VOLUME 6 ISSUE 3 OCTOBER 2021

IJEG

International Journal of Engineering and Geosciences

e-ISSN 2548-0960

The International Journal of Engineering and Geosciences (IJEG)

The International Journal of Engineering and Geosciences (IJEG) is a tri-annually published journal. The journal includes a wide scope of information on scientific and technical advances in the geomatics sciences. The International Journal of Engineering and Geosciences aims to publish pure and applied research in geomatics engineering and technologies. IJEG is a double peer-reviewed (blind) OPEN ACCESS JOURNAL that publishes professional level research articles and subject reviews exclusively in English. It allows authors to submit articles online and track his or her progress via its web interface. All manuscripts will undergo a refereeing process; acceptance for publication is based on at least two positive reviews. The journal publishes research and review papers, professional communication, and technical notes. IJEG does not charge for any article submissions or for processing.

CORRESPONDENCE ADDRESS
Journal Contact: engineeringandgeoscience@gmail.com

CONTENTS

Volume 6 - Issue 3

ARTICLES

International Journal of Engineering and Geosciences

https://dergipark.org.tr/en/pub/ijeg

e-ISSN 2548-0960

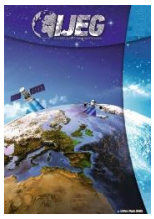

A new color distance measure formulated from the cooperation of the Euclidean and the vector angular differences for lidar point cloud segmentation

Ali Saglam[*1], **Nurdan Akhan Baykan** [2]

[1]*Konya Technical University, Engineering and Natural Sciences Faculty, Department of Computer Engineering, Konya, Turkey*

Keywords
Point Cloud Segmentation
Weighting
Color Distance
Measurement Vector
Angular Difference

ABSTRACT

Two important features of the points in the LiDAR point clouds are the spatial and the color features. The spatial feature is mostly used in the point cloud processing field due to its 3D informative and distinctive characteristic. The local geometric difference derived from the spatial features of the points is usually benefited by graph-based point cloud segmentation methods, because the geometric features of the local point groups are highly distinctive. In this paper, we use both the geometric and color differences of the adjacent local point groups at the impact rates 0.3, 0.5, and 0.7 and cooperate the Euclidean and the vector color differences within several averaging techniques for the color difference. The difference forms have been tested within a graph-based segmentation method on four point cloud segmentation datasets, two indoor and two outdoor, using their spatial and color information. The geometric mean as an averaging techniques increases the segmentation success for the all datasets except one outdoor when the color differences are used in the segmentation at the impact rate 0.3, while the harmonic mean increases the success for the all datasets the successes except the other outdoor at the same impact rate. According to the test results, the cooperating of the Euclidean and vector angular color difference measurements can considerable increase the segmentation success on the point clouds with color information in a high quality.

1. INTRODUCTION

Point clouds are 3D spatial and usually colored data obtained with light detection and ranging systems (LiDAR) (Strom et al., 2010). Because the points in a LiDAR point cloud inherently come as high amount and unorganized, to extract meaningful information from the data is a challenging problem (Li et al., 2017). The point cloud segmentation, which groups the points to reduce the data to be processed and extract new features, is an intermediate stage through the process of extracting meaningful information (Barnea and Filin, 2013).

Graph-based segmentation methods are widely preferred to segment the data for the segmentation process in both the image and point cloud processing fields. An efficient graph-based method (EGS) proposed for 2D image segmentation in (Felzenszwalb and Huttenlocher, 2004) is a widespread segmentation method due to the fastness and segmentation success. In this method, the nearby vertices (elements) are assumed to be connected by weighted edges. The weight values are weighted considering the differences in the color values between pixels for the 2D image segmentation process. Because the structures of 3D point clouds are unorganized unlike 2D images, it is difficult to process 3D point clouds. To deal with this problem, the points are usually grouped into regular 3D volumes (voxels) by the octree organization (Su et al., 2016; Xu et al., 2017). In this way, the edges are assumed between the adjacent voxels.

On the other hand, it is an advantage for the point cloud processing field that LiDAR data has 3D spatial features. The 3D feature provides geometrical features which are more distinctive according to the color feature. Therefore, most graph-based point cloud segmentation methods use the local surface orientation difference for weighting the connections instead of color difference (Vo et al., 2015; Xu et al., 2018a). The other reason for the preference of geometrical differences is that the color feature is usually misleading because the color

* **Corresponding Author**

*(asaglam@ktun.edu.tr) ORCID ID 0000 – 0003 – 2980 – 9666
(nbaykan@ktun.edu.tr) ORCID ID 0000 – 0002 – 4289 – 8889

Cite this article

Saglam A & Baykan N A (2021). A new color distance measure formulated from the cooperation of the Euclidean and the vector angular differences for lidar point cloud segmentation. International Journal of Engineering and Geosciences, 6(3), 117-124

Research Article / DOI: 10.26833/ijeg.709212 **Received: 25/03/2020; Accepted: 19/09/2020**

information of the points is sensitive to the brightness varying according to the light and the reflectiveness varying according to the materials of objects (Xu et al., 2018a). Another problem is that some spatially adjacent objects have similar colors. Nevertheless, some methods allow users to use color information with an adjustable influence rate, while some use color information at a certain rate (Papon et al., 2013; Strom et al., 2010; Zhu et al., 2017).

The quality of the color information of point clouds varies and quite affects the success of the segmentation stage if the color information is used at the rate that is higher than 0. In this work, we enforce to increases the segmentation success by using the color information more efficiently. In this reason, we focus on the local color differences methods between two adjacent elements in the RGB (red, green, and blue) color space. In the literature, the Euclidean distance is widely used for the color difference between the two elements (Aijazi et al., 2013; Bassier et al., 2017; Dutta et al., 2014; Papon et al., 2013; Strom et al., 2010). On the other hand, Chen et al. 2019 use the spectral angle as color difference in their study. In this work, we use the vector angular difference and cooperate with the Euclidean distance in some forms. The tested cooperation forms consist of the arithmetic, geometric and harmonic means of the two measurements.

Through our experiments, two indoor coarse and two outdoor fine point cloud segmentation datasets that include the RGB (red, green, and blue) color information of the points and reference segments. The color measures have been tested on the method EGS at the intervals 0.3, 0.5, and 0.7. The graphical results for two datasets are shown in the experimental results. As a quantitative segmentation evaluation, the Accuracy success measurement (Polak et al., 2009) has been used by looking at the compatibility between the result and reference segments after pairing them mutually one-to-one. According to the Accuracy values, the cooperated color difference measurements increases the segmentation success at the influence rate 0.3 for nearly all of the tested datasets.

The main contribution of this study is to present a new approach on the color distance measure for color informed point cloud segmentation. The result show that the cooperating of the Euclidean and vector angular differences by averaging as geometric and harmonic can significantly increases the segmentation success when the color information is a high quality in point clouds.

2. METHOD

2.1. Voxelization

Voxels are equal-sized 3D cubic volumes and of regular/organized data structures (Lohmann, 1998). For the voxel organization, the octree data structure has been used in this study like many studies in the literature. The octree organization is performed through dividing the volumes into eight equal-sized sub-volumes by starting from the sup-volume that covers all points in the point cloud and specified according to the desired voxel size until the sub-volumes reach the intended voxel size. The voxel size refers to the length of an edge of the voxels. Through the voxelization process, the points are appointed into the voxels according to spatial coordinates.

2.2. EGS Segmentation Method

Felzenszwalb and Huttenlocher, 2004 proposed a new segmentation method, named as "Efficient Graph-Based Method" (EGS), in 2004. The method runs successfully on 2D images in an effectively short time. The method regards the data elements (pixels for 2D images) as vertices and the connection between the adjacent vertices as edges. The edges are weighted with the Euclidean distance between the color vectors of the two vertices that are ends of the edges. In Fig. (1), the stages of the segmentation is presented.

According to the method, at first, each element is seen as a segment and has a unique segment label. The edges are sorted in ascending order according to their weight values. Beginning from the smallest edges, the edges are considered to remove from the graph with respect to the criterion in Eq. (1). If the weight value $w(u,v)$ of the edge between the vertices u and v meets the criteria, the edge is removed from the graph. Otherwise, the segments at the ends of the edge are involved in the same segments, and the elements in the two segments are labeled with the same segment label. If the segment labels are already the same, the edge is not evaluated by the criterion and directly removed. In Eq. (1), $Int(u)$ and $Int(v)$ are the longest edge in the segments S_u and S_v, respectively. $|S_u|$ and $|S_v|$ refer to the number of elements in the segments S_u and S_v, respectively. The parameter k determines the degree of segmentation (under-segmentation or over-segmentation).

$$\boldsymbol{w(u,v) > min\left(Int(u) + \frac{k}{|S_u|}, Int(v) + \frac{k}{|S_v|}\right)} \quad (1)$$

2.3 Geometric Difference

The most used feature of the point groups in the voxels is the surface normals (Rabbani et al., 2006). The normal vectors give the inclination of the local 3D surfaces and the PCA (Principal Component Analyses) method is the most used technique to obtain it (Lari and Habib, 2014). The angle between the normals of two adjacent voxels is one of the basic geometric differences. The normalized form $\widetilde{\boldsymbol{d_{uv}}}$ of the vector $\boldsymbol{d_{uv}}$ between the spatial centers $\boldsymbol{X_u}$ and $\boldsymbol{X_v}$ of two-point groups is a way to estimate the orientation through two adjacent local surfaces (Stein et al., 2014; Verdoja et al., 2017; Xu et al., 2018a). The angles α_u and α_v between the vector $\widetilde{\boldsymbol{d_{uv}}}$ and the normals $\widetilde{\boldsymbol{n_u}}$ and $\widetilde{\boldsymbol{n_v}}$ used widely to measure a geometric difference from the two local surfaces. As the geometric difference D_{uv}^{G} in this work, we have used the formula in Eq. (2).

$$\boldsymbol{D_{uv}^{G} = \frac{\alpha_u + \alpha_v}{2}} \quad (2)$$

The angles $\boldsymbol{\beta_u}$ and $\boldsymbol{\beta_v}$ in Fig. 2 (a) and Fig. 2 (b) are the acute angles between the normals and the vector $\widetilde{\boldsymbol{d_{uv}}}$, namely, the angles can be in the range 0-90°. The angles $\boldsymbol{\alpha_u}$ and $\boldsymbol{\alpha_v}$ are obtained by subtracting the angles $\boldsymbol{\beta_u}$ and $\boldsymbol{\beta_v}$ from 90°.

2.4 Color Difference

LiDAR systems can integrate the spatial and color information about the scanned surfaces. In this way, the points in a point cloud save the values of both the coordinate and color vectors. The color information exists generally as RGB values. Each RGB color vector denotes a vector in the RGB color space.

In the graph-based segmentation methods, the Euclidean distance between two color vectors is the most used measurement technique to measure the similarity/dissimilarity. To weight the edges between the vertices (voxels) with the Euclidean distance in point clouds, the mean RGB color values (u^R, u^G and u^B) of the points in the voxel u are used. The Euclidean distance E_{uv}^{RGB} for color differences between the adjacent voxels u and v can be calculated with Eq. (3) and seen in Fig. 3.

$$\boldsymbol{E_{uv}^{RGB}} = \sqrt{(\boldsymbol{u^R - v^R})^2 + (\boldsymbol{u^G - v^G})^2 + (\boldsymbol{u^B - v^B})^2} \qquad (3)$$

The vector angular difference is another distance measurement technique between two vectors as seen in Fig. 3. The angular difference $\hat{A}_{uv}^{RGB}$ between two color vectors $\boldsymbol{u^{RGB}}$ and $\boldsymbol{v^{RGB}}$ can be in the range 0-.90°. The greater the angular difference, the greater the color tone difference. If the angular difference is small but the vector length difference is high between two RGB color vectors, their color tone is similar but color lightness/darkness is different. This case allows the varying brightness over the surfaces to be ignored in the color-supported segmentation process.

In this work, the values of the scaled Euclidean and vector angular differences, and their different cooperated forms in Table 1 are tested, with the different influence rates, to weight values of edges. To evaluate both the color differences within the equal range, the calculated Euclidean distance $\boldsymbol{E^{RGB}}$ are scaled to the range 0-90 like the vector angular difference $\widehat{\boldsymbol{A}}^{\boldsymbol{RGB}}$ and the geometric difference $\boldsymbol{D^G}$. In the normalization operation for the scaled Euclidean distance $\widehat{\boldsymbol{E}}^{\boldsymbol{RGB}}$, the lower and upper limits were considered as 0 and the maximum distance among the calculated Euclidean distance values.

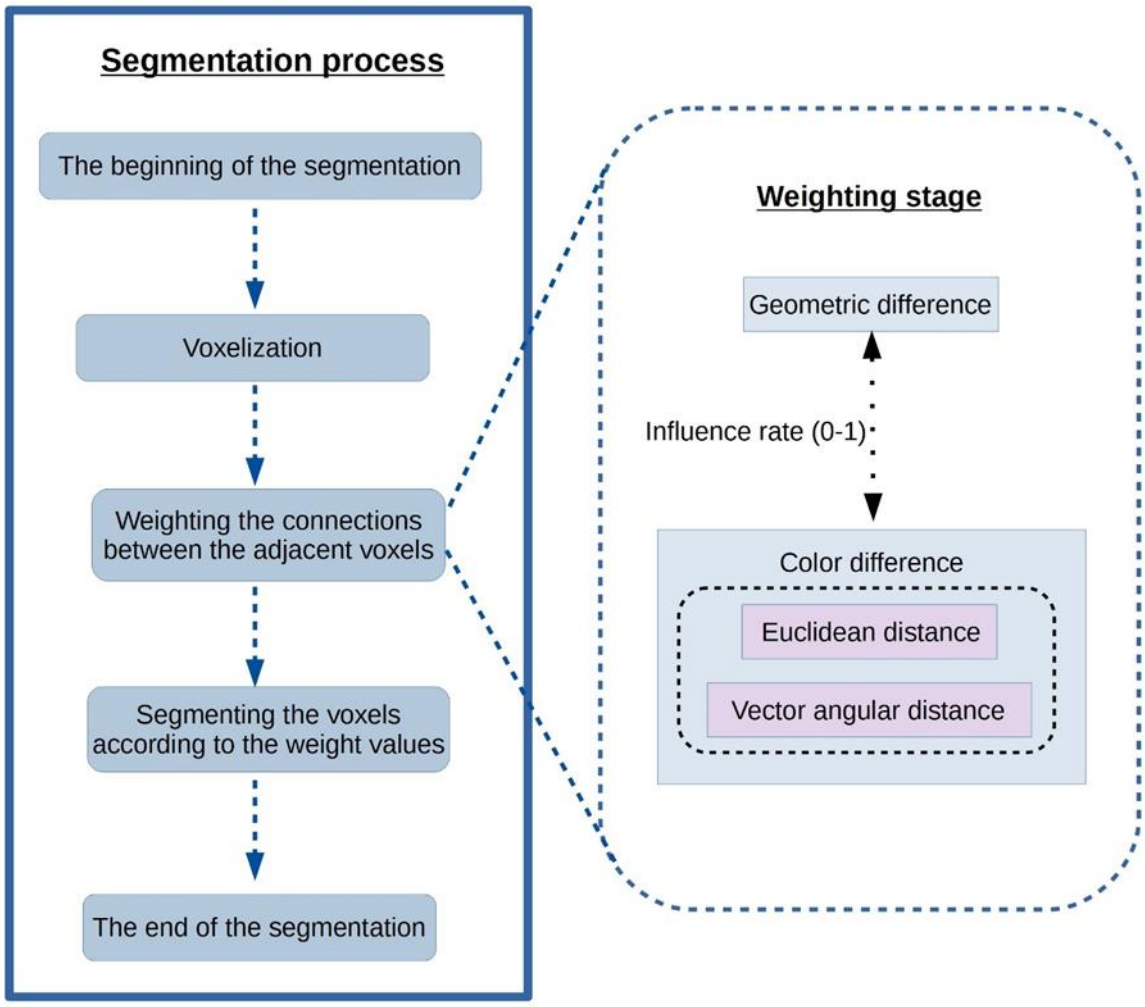

Figure 1. The weighting stage in the segmentation

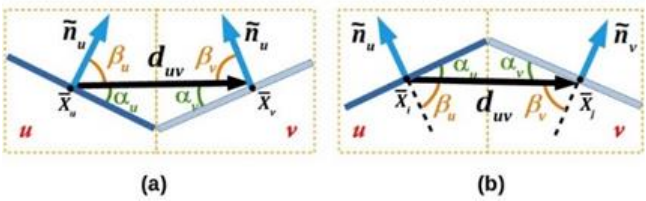

Figure 2. Some geometric differences between two local surfaces

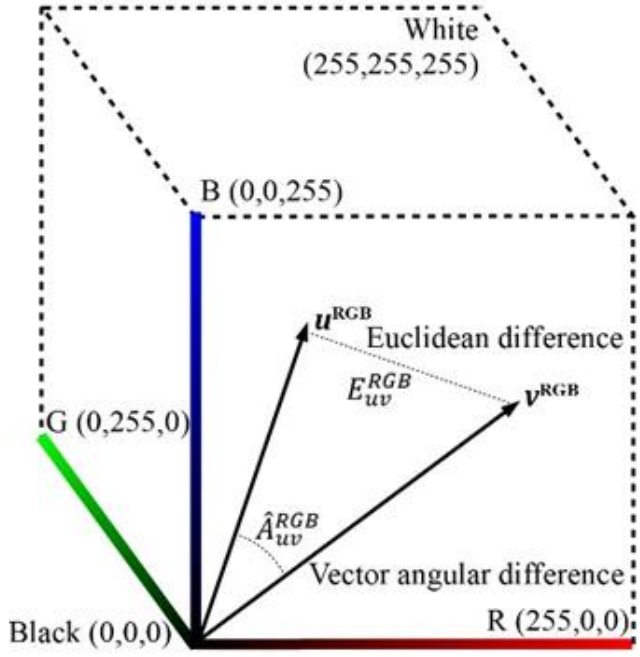

Figure 3. The Euclidean and vector angular differences between two color vectors

Table 1. Cooperation forms of color differences

Name	Color Difference Form
Euclidean color difference	$\hat{E}^{RGB}$
Vector angular color difference	$\hat{A}^{RGB}$
Arithmetic mean	$\frac{\hat{E}^{RGB} + \hat{A}^{RGB}}{2}$
Geometric mean	$\sqrt{\hat{E}^{RGB} \times \hat{A}^{RGB}}$
Harmonic mean	$2 \times \frac{\hat{E}^{RGB} \times \hat{A}^{RGB}}{\hat{E}^{RGB} + \hat{A}^{RGB}}$

3. EXPERIMENTAL RESULTS

3.1 Datasets

To test the color difference forms, the forms have been tested on four sample point cloud datasets (two indoors which are named as “Indoor 1” and “Indoor 2”, and two outdoors which are named as “Outdoor 1” and “Outdoor 2”). The indoor datasets are coarse segmentation datasets prepared for segmantic segmentation by (Armeni et al., 2016), while the outdoor datasets are cropped from outdoor building scans, which have been prepared from the two large-scale point cloud classification benchmark datasets (Hackel et al., 2017) with reference segments by (Xu et al., 2018a) and used by permission of (Xu et al., 2018b). The test data are shown with their original RGB colors in Fig. 4.

3.2 Results

In our experiments, the color difference forms in Table 1 have been used at the influence rates 0.3, 0.5, and 0.7 with the geometric difference in Eq. (2) for the weight values of edges of the EGS method with the segmentation parameter k in the range 0-300 with 10 intervals. The voxel size was specified as 0.1 like the study (Xu et al., 2018a).

As a quantitative evaluation, Accuracy measurement is used (Saglam and Baykan, 2019). According to the Accuracy measurement for segmentation success, the result segments and the reference segments have been paired firstly one-to-one, mutually. The pairing process is carried out according to the study (Awrangjeb and Fraser, 2014). After the pairing process, some segments among the result and reference segments may not be paired with any mutual segments. The ratio of the number of common points in the segment pairs to the number of points in the reference data indicates the Accuracy value.

In Table 2, the Accuracy results of the segmentation results with the best k parameter according to the color difference forms at the influence rates 0.3, 0.5, and 0.7 are taken part. In Fig. 5, the colored presentations of some segmentation results with reference data are demonstrated.

4. CONCLUSION

The process of point cloud segmentation is an important intermediate stage to extract meaningful information from the raw point clouds. The spatial geometric features are the most used property for graph-based point cloud segmentation methods. In this paper, we have added the color influence to local dissimilarity to weight connections in the graph structure at several influence rate**.** In the weighting method, the Euclidean and vector angular color differences are cooperated in some forms as arithmetic mean, geometric mean and harmonic means. The test was carried out on two indoor and two outdoor datasets using an efficient graph-based segmentation method. The method that cooperates the two color difference measures, especially the geometric mean and the harmonic mean, has substantially increased the segmentation success on the indoor datasets. On the other hand, the successes on the outdoor datasets is increased slightly because of the lack of color information on the outdoor datasets. The geometric mean as an averaging techniques increases the segmentation success for the all datasets except one outdoor when the color differences are used in the segmentation at the impact rate 03, while the harmonic mean increases the success for the all datasets the successes except the other outdoor at the same impact rate. The results show that the method is very useful when the segmentation are processed on the point clouds with sufficient color information.

ACKNOWLEDMENT

This study was carried out in the scope of the Doctoral Thesis of Ali SAGLAM.

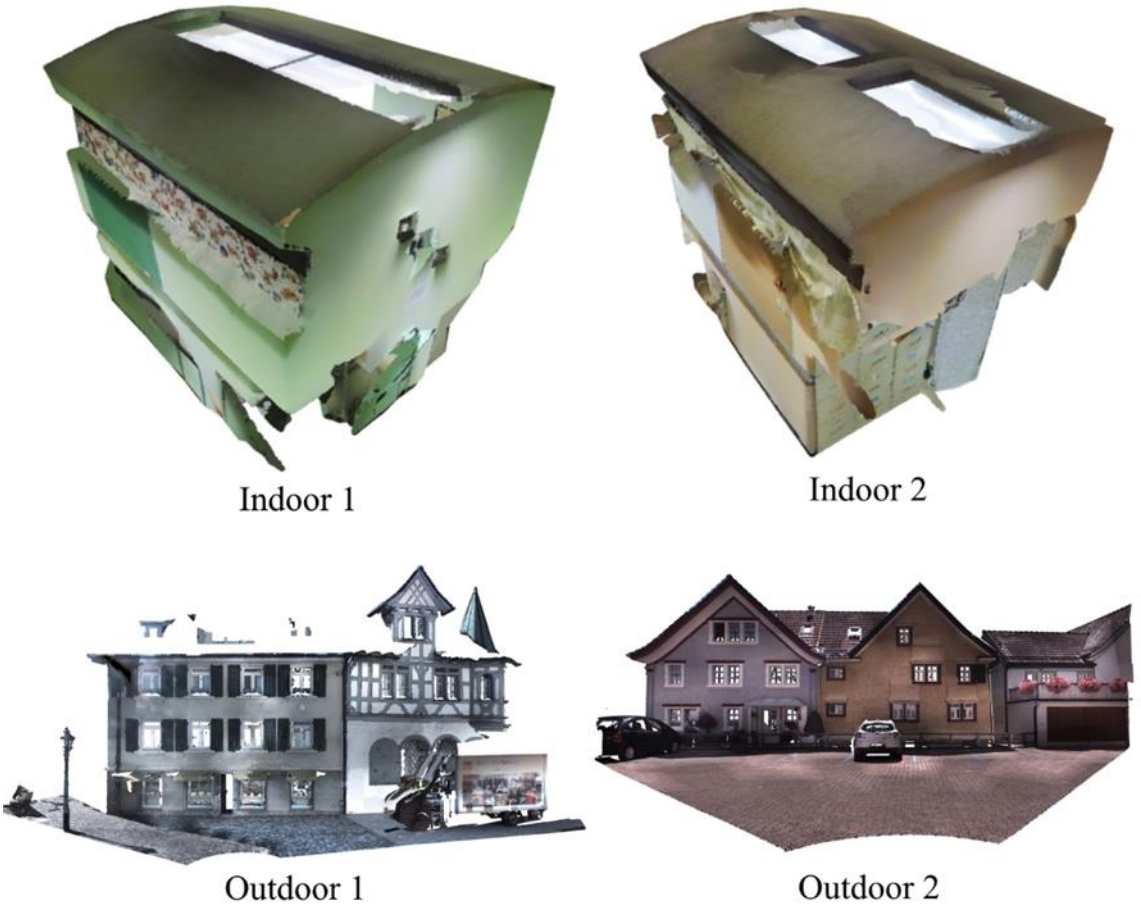

Figure 4. The original versions of the datasets used for segmentation

Table 2. Accuracy results of the colour difference forms

Color difference form	Color influence rate	Dataset			
		Indoor 1	Indoor 2	Outdoor 1	Outdoor 2
No color	0	0.6997	0.7187	0.6879	0.8036
Scaled Euclidean difference	0.3	0.7057	0.7528	0.6076	0.7820
Scaled Euclidean difference	0.5	0.7093	0.7158	0.5718	0.7209
Scaled Euclidean difference	0.7	0.6641	0.7058	0.4792	0.7058
Vector angular difference	0.3	0.6807	0.7232	0.6593	0.7847
Vector angular difference	0.5	0.7154	0.7876	0.6928	0.7507
Vector angular difference	0.7	0.7080	0.7588	0.6384	0.6968
Arithmetic mean	0.3	0.6931	0.6873	0.6225	0.7810
Arithmetic mean	0.5	0.7282	0.7643	0.5564	0.7342
Arithmetic mean	0.7	0.6579	0.7484	0.4912	0.6868
Geometric mean	0.3	0.7094	0.7937	0.6849	0.8176
Geometric mean	0.5	0.7351	0.7566	0.6294	0.7960
Geometric mean	0.7	0.7077	0.7153	0.5703	0.7168
Harmonic mean	0.3	0.7048	0.7436	0.7132	0.7782
Harmonic mean	0.5	0.7884	0.7386	0.6770	0.7787
Harmonic mean	0.7	0.7670	0.7763	0.5501	0.6761

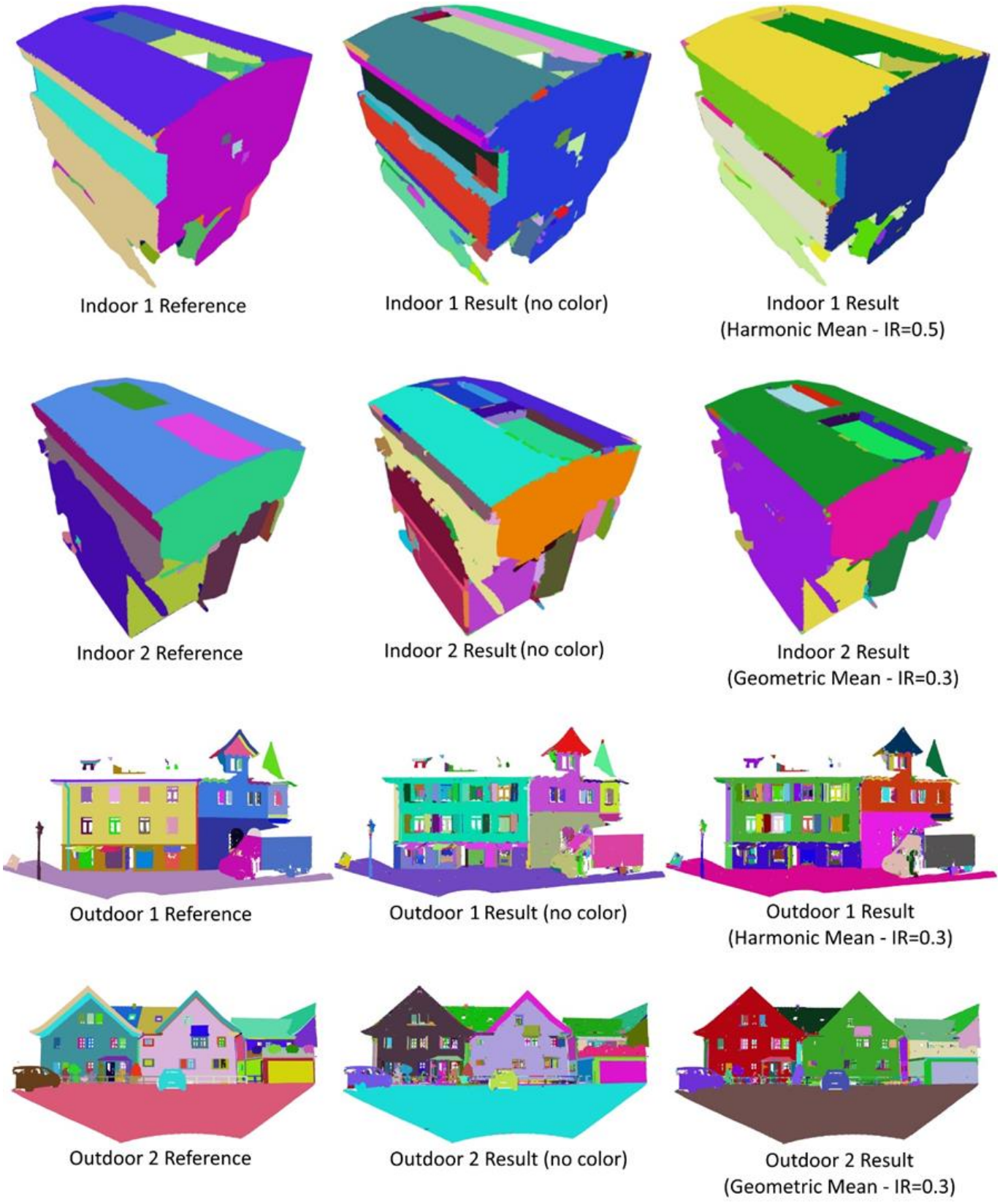

Figure 5. The colored reference data and segmentation results (with no color and some cooperated forms)

REFERENCES

Aijazi A K, Checchin P & Trassoudaine L (2013). Segmentation Based Classification of 3D Urban Point Clouds: A Super-Voxel Based Approach with Evaluation. Remote Sensing, 5(4), 1624–1650. https://doi.org/10.3390/rs5041624

Armeni I, Sener O, Zamir A R, Jiang H, Brilakis I, Fischer M & Savarese S (2016). 3D semantic parsing of large-scale indoor spaces. Proceedings of the IEEE Computer Society Conference on Computer Vision and Pattern Recognition. https://doi.org/10.1109/CVPR.2016.170

Awrangjeb M & Fraser C S (2014). An automatic and threshold-free performance evaluation system for building extraction techniques from airborne LIDAR data. IEEE Journal of Selected Topics in Applied Earth Observations and Remote Sensing 7(10), 4184–4198. https://doi.org/10.1109/JSTARS.2014.2318694

Barnea S & Filin S (2013). Segmentation of terrestrial laser scanning data using geometry and image information. ISPRS Journal of Photogrammetry and Remote Sensing, 76, 33–48. https://doi.org/10.1016/j.isprsjprs.2012.05.001

Bassier M, Bonduel M, Van Genechten B & Vergauwen M (2017). Segmentation of large unstructured point clouds using octree-based region growing and conditional random fields. International Archives of the Photogrammetry, Remote Sensing and Spatial Information Sciences - ISPRS Archives XLII-2/W8, 25–30. https://doi.org/10.5194/isprs-archives-XLII-2-W8-25-2017

Chen B, Shi S., Sun J, Gong W, Yang J, Du L, Guo K, Wang, B, Chen, B (2019). Hyperspectral lidar point cloud segmentation based on geometric and spectral information. Optics Express, 27(17). https://doi.org/10.1364/oe.27.024043

Dutta A, Engels J & Hahn M (2014). A distance-weighted graph-cut method for the segmentation of laser point clouds. International Archives of the Photogrammetry, Remote Sensing and Spatial Information Sciences - ISPRS Archives 40(3), 81–88. https://doi.org/10.5194/isprsarchives-XL-3-81-2014

Felzenszwalb P F & Huttenlocher D P (2004). Efficient graph-based image segmentation. International Journal of Computer Vision, 59(2), 167–181. https://doi.org/10.1023/B:VISI.0000022288.19776.77

Hackel T, Savinov N, Ladicky L, Wegner J D, Schindler K & Pollefeys M (2017). Semantic3D.net: A new Large-scale Point Cloud Classification Benchmark. ISPRS Annals of the Photogrammetry, Remote Sensing and Spatial Information Sciences. https://doi.org/10.5194/isprs-annals-IV-1-W1-91-2017

Lari Z & Habib A (2014). An adaptive approach for the segmentation and extraction of planar and linear/cylindrical features from laser scanning data. ISPRS Journal of Photogrammetry and Remote Sensing, 93, 192–212. https://doi.org/10.1016/j.isprsjprs.2013.12.001

Li L, Yang F, Zhu H, Li D, Li Y & Tang L (2017). An improved RANSAC for 3D point cloud plane segmentation based on normal distribution transformation cells. Remote Sensing 9(5). https://doi.org/10.3390/rs9050433

Lohmann G (1998). Volumetric image analysis. Wiley.

Papon J, Abramov A, Schoeler M & Worgotter F (2013). Voxel cloud connectivity segmentation - Supervoxels for point clouds. Proceedings of the IEEE Computer Society Conference on Computer Vision and Pattern Recognition, 2027–2034. https://doi.org/10.1109/CVPR.2013.264

Polak M, Zhang H & Pi M (2009). An evaluation metric for image segmentation of multiple objects. Image and Vision Computing, 27(8), 1223-1227. https://doi.org/10.1016/j.imavis.2008.09.008

Rabbani T, van den Heuvel F A & Vosselman G (2006). Segmentation of point clouds using smoothness constraint. International Archives of Photogrammetry, Remote Sensing and Spatial Information Sciences - Commission V Symposium "Image Engineering and Vision Metrology" 36, 248–253. https://doi.org/10.1111/1750-3841.12802

Saglam A & Baykan N A (2019). Evaluating the attributes of remote sensing image pixels for fast k-means clustering. Turkish Journal of Electrical Engineering & Computer Sciences, 27, 4188–4202. https://doi.org/10.3906/elk-1901-190

Stein S C, Schoeler M, Papon J & Worgotter F (2014). Object partitioning using local convexity. Proceedings of the IEEE Computer Society Conference on Computer Vision and Pattern Recognition, 304–311. https://doi.org/10.1109/CVPR.2014.46

Strom J, Richardson A & Olson E (2010). Graph-based segmentation for colored 3D laser point clouds. IEEE/RSJ 2010 International Conference on Intelligent Robots and Systems, 2131–2136. https://doi.org/10.1109/IROS.2010.5650459

Su Y T, Bethel J & Hu S (2016). Octree-based segmentation for terrestrial LiDAR point cloud data in industrial applications. ISPRS Journal of Photogrammetry and Remote Sensing 113, 59–74. https://doi.org/10.1016/j.isprsjprs.2016.01.001

Verdoja F, Thomas D & Sugimoto A (2017). Fast 3D point cloud segmentation using supervoxels with geometry and color for 3D scene understanding. Proceedings - IEEE International Conference on Multimedia and Expo, Hong Kong, China, 1285–1290. https://doi.org/10.1109/ICME.2017.8019382

Vo A V, Truong-Hong L, Laefer D F & Bertolotto M (2015). Octree-based region growing for point cloud segmentation. ISPRS Journal of Photogrammetry and Remote Sensing 104, 88–100. https://doi.org/10.1016/j.isprsjprs.2015.01.011

Xu Y, Hoegner L, Tuttas S & Stilla U (2017). Voxel- and graph-based point cloud segmentation of 3D scenes using perceptual grouping laws. ISPRS Annals of Photogrammetry, Remote Sensing and Spatial Information Sciences IV-1/W1, 43–50. https://doi.org/10.5194/isprs-annals-IV-1-W1-43-2017

Xu Y, Yao W, Tuttas S, Hoegner L & Stilla U (2018a). Unsupervised Segmentation of Point Clouds From

Buildings Using Hierarchical Clustering Based on Gestalt Principles. IEEE Journal of Selected Topics in Applied Earth Observations and Remote Sensing 11, 4270–4286. https://doi.org/10.1109/JSTARS.2018.2817227

Xu Y, Yao W, Tuttas S, Hoegner L & Stilla U (2018b). Building-Segmentation-Reference-Dataset [WWW Document]. URL https://github.com/Yusheng-Xu/Building-Segmentation-Reference-Dataset

Zhu Q, Li Y, Hu H & Wu B (2017). Robust point cloud classification based on multi-level semantic relationships for urban scenes. ISPRS Journal of Photogrammetry and Remote Sensing, 129, 86–102. https://doi.org/10.1016/j.isprsjprs.2017.04.022

International Journal of Engineering and Geosciences

https://dergipark.org.tr/en/pub/ijeg

e-ISSN 2548-0960

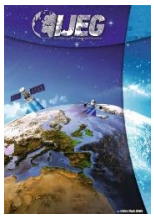

Comparison of point cloud filtering methods with data acquired by photogrammetric method and RGB-D sensors

Mehmet Akif Günen [*1], **Erkan Beşdok**[1]

[1]*Erciyes University, Engineering Faculty, Department of Geomatics Engineering, Kayseri, Turkey*

Keywords
Point Cloud
Photogrammetry
RGB-D Sensor
Terrestrial Laser Scanners
Backtracking Search
Optimization Based Filter

ABSTRACT

Point clouds (PCs) are inevitable sources to generate digital solid model-based applications such as reverse engineering, differential 3D modelling, 3D sensing and modelling of environments, scene reconstruction, augmented reality. Photogrammetric methods, Terrestrial Laser Scanners and RGB-D sensors are relatively common among the technologies used to capture PCs. Because of their structural characteristics, measuring systems produce large amounts of noise that cannot be precisely predicted in type and amplitude. Due to the noisy measurements, the spatial orientations of the differential surface particles and the spatial locations of the corner points have a certain degree of deformation. In order to increase visual, spatial and physical quality of the solid model, which is frequently used in reverse engineering, PCs must be filtered to discard noise and outlier. In this paper PC produced from different methods was filtering with Shepard Inverse Distance Weighting method, Gaussian Filtering method, Single Value Decomposition Based Plane Fitting method and Optimization Based Plane Fitting method. Backtracking Search Optimization Algorithm (BSA) was used to fitting plane. Experimental results were compared visually and statistical according to the number of neighborhoods. The results showed that Backtracking Search Optimization based filtering supplied better noise smoothing results than its competitors.

1. INTRODUCTION

3D Point Cloud (PC) plays an important role in creating and rendering solid models of physical objects. PC processing is an active research field because it is used in different research applications such as 3D reconstruction (Ahmadabadian et al. 2019), environmental mapping (Gunen et al. 2017), signal processing (Aghababaee et al. 2019), object recognition (Garcia-Garcia et al. 2018) and pose estimation (Vock et al. 2019), drainage network determination (Gunen et al. 2019). 3D reconstruction applications are increasing with falling costs of computing platforms and improvements in 3D capture systems. Various technologies have been developed based on relatively different principles for acquiring highly accurate PCs from the physical structures of objects. Despite advances in PC capture technologies used to express the numerical equivalents of physical models, PCs suffer from noise due to instantaneous changes in atmospheric physical parameters and noise sources contained in the 3D capture method and equipment used. Therefore, in order to produce high-accuracy digital models of physical models, various noise types that contaminate the PCs should be filtered (Hou et al. 2012; Narváez and Narváez 2006)

RGB-D sensors, Photogrammetric Methods, and Terrestrial Laser Scanner (TLS) are the mostly used PC obtaining methods and can be examined in two parts: active and passive methods. While commonly used TLS and RGB-D sensor are active methods, Optical Photogrammetric methods are passive methods (Oliveira et al. 2014). These three methods, which are frequently used in obtaining a PC, have different technical structures. The 3D spatial coordinates are measured in the local coordinate system depending on the direction and distance of the object to be measured according to TLS. Also, TLS is capable of capturing millions of points per second and effectively generating a 3D PC of large areas in a short period. Although it

* **Corresponding Author**

*(akif@erciyes.edu.tr) ORCID ID 0000-0001-5164-375X
(ebesdok@erciyes.edu.tr) ORCID ID 0000-0001-9309-375X

Cite this article

Gunen M A & Besdok E (2021). Comparison of point cloud filtering methods with data acquired by photogrammetric method and RGB-D sensors. International Journal of Engineering and Geosciences, 6(3), 125-135

Research Article / DOI: 10.26833/ijeg.731129

Received: 02/05/2020; Accepted: 19/06/2020

produces high accuracy and precision PC, TLSs have high investment cost. Photogrammetric methods define parallax between correspondence-points in the images of the scene and allow it to obtain spatial coordinates of points related to the extrinsic and intrinsic orientation parameters. Photogrammetric methods have been rapidly increasing in popularity due to progress in imaging technology and software (Ulvi 2018). RGB-D sensors are compact systems consisting of an infrared camera and an RGB camera. Therefore, RGB-D sensors provide the possibility to obtain texture, like some TLS and photogrammetric methods, as well as depth map. RGB-D sensors are widely used in the production of indoor maps, especially with their programmable structures and cost (Amenta, 1999; Hoppe et al. 1992; Tölgyessy and Hubinský 2011).

PCs contain indispensable noise and outliers due to inadequate sensor limits, imperfect nature of the instruments, scene artifacts, presence of inadequate ambient conditions, and systematic errors. Depending on the system PC produced, the sampled discrete information should be processed to remove the noise (Wolff et al. 2016). The raw PC should be filtered to ensure further analysis and processing. In addition, PC filtering is employed to preserve existing details expressed by the PC, such as edge features and to get the smooth surfaces that are required to produce realistic digital models of physical objects (Cai et al., 2019). It is very difficult to recognize and interpret a PC in terms of human perception. So that, they can be converted to solid model surfaces, which is the differential surfaces of mesh model and the edge elements of these surfaces, using mesh models.

In recent years, many 3D filtering methods have been developed for denoising PCs. In general, noise suppression from literature has been done using two different approaches, data processing in the form of a PC and processing of data in the form of differential surface elements (Fleishman et al. 2003). Both approaches benefit from the topological relationships of the vertexes with their neighborhoods. In general, both approaches are based on moving vertex points according to certain criteria. Most of these are applied to the mesh and the lesser part is applied directly to the PCs. Point cloud filtering methods can be generally divided into neighborhood based, statistical based and projection based. Neighborhood based methods that use similarity information between point and its neighbors are the most used methods since they are effective and easy (Han et al., 2017).

The Gaussian Filtering (GF) computes Euclidean distances between the point of interest and its specific neighborhoods. Then, by using Gaussian weights produced with the help of distances, the current point is filtered (Adams et al. 2009; Wirjadi and Breuel 2005). In Median Filtering, the neighborhoods of the point of interest are determined depending on the distance. Then, the median point of the point is projected to a local plane and filtering is performed. The Moving Least Squares method is based on the recognition of the relevant parameter solutions to localized polynomial surfaces obtained by local measurement values. The general method used in the development of the average filtering is based on identifying the normalized mean vectors of the local normal vectors of the points adjacent to the point of interest. Then moving the corresponding point towards the local surface defined by the adjacent points (Gunen, 2017). The Shepard Inverse Distance Weighting (IDW) filtering is one of the basic methods used for filtering PCs is to project each point in the PC by defining the selected limited number of neighboring points. Fluctuated surfaces can be defined by the tensor products of the base functions (Babak and Deutsch 2009; Lu and Wong 2008). Plane-based filtering methods, such as Single Value Decomposition (SVD) Based Plane Fitting, produce fast results. However, they are not robust to noisy data. Evolutionary Computing methods supply better results in general than classical local plane fitting tools, such as the least square method, in the solution of a best plane fitting problem (Gunen, 2017; Kurban, 2014).

Evolutionary computation methods are stochastic search methods that are used effectively in solving different types of problems (Civicioglu et al. 2020). The fact that they produce more successful results than classical methods in solving complex problems such as PC cloud filtering motivated the design of a new Evolutionary computation-based 3D spatial filtering.

The PC datasets used in this paper were produced by using TLS, RGB-D sensor, and Photogrammetric method. The PC produced by TLS was determined as reference data, due to its inherent properties. Shepard Inverse Distance Weighting Method (IDW), Gaussian Filtering Method (GF), Single Value Decomposition Based Filtering Method (SVD) and Optimization Based Plane Fitting by using Backtracking Search Optimization Algorithm (BSA) Method with different number of neighborhoods were used to filtering PCs produced by using RGB-D sensor and Photogrammetric method.

The rest of this paper has been organized as follows; Section 2 presents Data Collection, Material and Methods are presented in Section 3, Experimental Results and Discussion are given in Section 4.

2. DATA COLLECTION

In this section, general 3D data capture principles of the TLS, RGB-D, and Photogrammetric techniques have been analyzed comparatively.

2.1. Terrestrial Laser Scanner

In recent years, with the changing and developing technology, laser technology has reached a very advanced level. Capable of capturing thousands of points per second, TLSs can produce data at the desired quality and time, from small objects to large areas without being noticed day or night. In addition to the brand and model of TLS devices using Light Detection and Ranging (LIDAR) technology, the resolution and quality parameters used in scanning affect the PC's spatial coordinate (Sevgen 2019; Yu et al. 2004). TLSs are expensive due to their high equipment requirements, the need for specialized software knowledge, and the need for skilled employees (Yu et al. 2004). Since the PC of the object is created in more than one session, it is necessary

to transform in the global or mutual local coordinate system. The random sample consensus (RANSAC)-based Iterative closest point (ICP) method is generally used for registration or geo-referencing of the PCs from different sessions (Gunen et al. 2017, Altuntas, 2015). It selects random points on different PCs to allow correspondence points to be searched and finalizes the registration process according to the determined criteria (Altuntas, 2015). In addition to being fast and reliable, RANSAC-based is preferred because of sampling large data.

Faro Focus3D X130 TLS was used to obtain the PC. The Faro Focus3D X130 TLS is used to obtain PCs because it offers versatile measurement, wide range of solutions, and colored PC. Its light weight, integrated structure, advanced distance measurement capability, and intuitive operation system are used in work requiring precision. In addition to its ability to scan 976,000 dots per second and to scan up to 130 meters of area, its integrated camera captures the current scanning scene with 70 MP 8-bit RGB images. Each model used in the application was scanned in six different sessions with various directions and heights (URL, 2019).

2.2. Photogrammetric Methods

The Photogrammetric method acquires 3D PC from the sequential 2D images obtained as overlapping intervals. Multiple images obtained from different angles are used to produce 3D information (Javernick et al. 2014; Tercan, 2017). There are several methods to produce a PC from Satellite, Aerial, and Close-Range images with multiple views. Structure from Motion (SfM) is the method that provides high success and accuracy. SfM is a remote sensing method that produces 3D spatial coordinates of objects using color information of randomly ordered multiple view images. The optimal measurement design is the beginning of the PC production phase. In other words, in order to obtain the best results of the operations in the works as soon as possible, it is necessary to understand the system and technique of the images captured (Gunen et al. 2020; Li et al. 2012; Ulvi 2018). Much of the software uses key points of multiple images to determination the relative orientation of the camera. They usually use the Scale-Invariant Feature Transform and Speeded up Robust Features local feature detector (Juan and Gwon 2009) to determine key points. By using key points, correspondence points are matched by methods such as the RANSAC algorithm. The key point determination is very sensitive to noise; therefore, the results depend on spatial and radiometric resolution images. Also, these points are necessary for the creation of epipolar geometry. After the epipolar geometry is created, the relative orientation of the sequential cameras relative to each other is carried out and their dense point cloud as up to scale is determined. Paying attention to the accuracy of the light in the correct direction and the overlap rate in the pair of stereo images affects the data quality when capturing images of the object (Xiang and Cheong 2003). In cases where the image overlap rates are too low and there are extreme differences between the image scales, SfM may not produce a sufficient result (Doğan and Yakar 2018; Javernick et al. 2014). For better image matching on scene images, the fixed lens should be captured at as high a spatial resolution as possible. Sony Alpha ILCE-A6000, which has a Semi-Pro mirrorless camera and fixed lens, was used to capture images. It is a compact system that can shoot at a resolution of 6000x4000 and has a 24.3 megapixel 23.5x15.6 mm sized CMOS sensor. In addition, the advanced image processor and a superior AF system produces less aliasing images in moving scenes. 109 images were used to produce Model 1, as seen in Figure 1.b. 118 images were used to produce Model 2, as seen in Figure 1.e.

2.3. RGB-D sensor

The use of RGB-D sensor in 3D reconstruction applications in computer graphics and computer vision started rapidly in the last several decades. RGB-D sensor, which is developed for human computer interaction, is being used by different disciplines, together with the Software Development Kit (SDK) developed. Great attention has been paid to research due to its cost saving, easy accessibility, efficiency in 3D reconstruction, and use in Simultaneous localization and mapping (SLAM) application (Stückler et al. 2015). RGB-D sensor, which is the time-of-flight-based depth cameras, consist of infrared (IR) depth sensor, IR emitter and RGB camera. These lightweight sensors provide color and depth per pixel in enough resolution. Red, green, and blue CMOS sensors are used in RGB imagery. The depth map is produced by the IR camera, where the distance between the object and the view is recorded as a pixel value by pseudo scale distance. It is very important for the sensor to produce a depth map because the distance is recorded as pixel value and depth information basic of PC. Since the sequential and still image is captured in SLAM applications, various methods have been developed for producing a PC or model simultaneously. Two methods, mainly image-based and shaped-based, are used to generate PCs using an RGB-D sensor (Nyarko et al. 2018). The PC produced from each of the depth maps from the sequential frames has a local coordinate system. In the shaped-based method, PC registration is performed by using RANSAC based ICP between sequential PCs because of the efficiency and reliability of the method. In the image-based methods, pose estimation is performed with the help of epipolar geometry, which forms the basis of photogrammetry. To do this, the key points are first determined from the sequential images and then the corresponding points are determined by RANSAC based methods. With the help of correspondence points, the pose estimation process is completed. In both methods, because of the simultaneous operation, the rapid movement of the sensor or the sudden displacement of the object prevents the calculation of the homography between the PCs and causes the mismatch (Stückler et al. 2015). PCs obtained with RGB-D sensors generate noise depending on the texture of the object surface, lighting condition, viewing angle, sensor restriction and distance to object. Therefore, filters such as Kalman are adapted to the sensors or the PC generated from the depth map is filtered to remove potential noise (Jia et al. 2019). In this paper, a Kinect 2 RGB-D sensor is used. This sensor can capture 30 frame images per second at a 1920x1080

spatial resolution. The effective SLAM-operated sensor between 0.5/4.5 meters can produce a depth map at 514x424 spatial resolution.

3. MATERIAL and METHODS

The noise level of PCs significantly affects the accuracy of reconstructed models. In order to increase the model accuracy, a controlled filtering process should be used. Filtering can cause the destruction of noisy data from the PC, as well as extracting or suppressing noisy data representing the PC. In this paper, it is emphasized to increase the quality of the model obtained from different methods and to remove noisy data from the PC. IDW, GF, SVD Based Plane Fitting, and Optimization Based Plane Fitting by using BSA methods were used to remove noise.

In practice, the test models (Model 1 and Model 2) in Figure 1, obtained by using TLS are considered to be errorless data (reference data) assuming that there is not much noise because they are obtained from close range. PCs of models obtained from the photogrammetric method and the RGB-D sensor were filtered and then results were compared with the reference data. While obtaining models with different methods, the same lighting conditions were provided. Since each model is produced in the local coordinate system, it is represented in the same coordinate system using the RANSAC-based ICP method. In Model 1, the photogrammetric method produced 124,211 points, TLS produced 259,726 points, and RGB-D sensor produced 100,038 points. In Model 2, the photogrammetric method produced 354,254 points, TLS produced 444,404 points, and RGB-D sensor produced 184,768 points. Although the models produced with three different methods for both models were recorded under equal conditions of lighting in the laboratory environment, they produced different colors due to system characteristics.

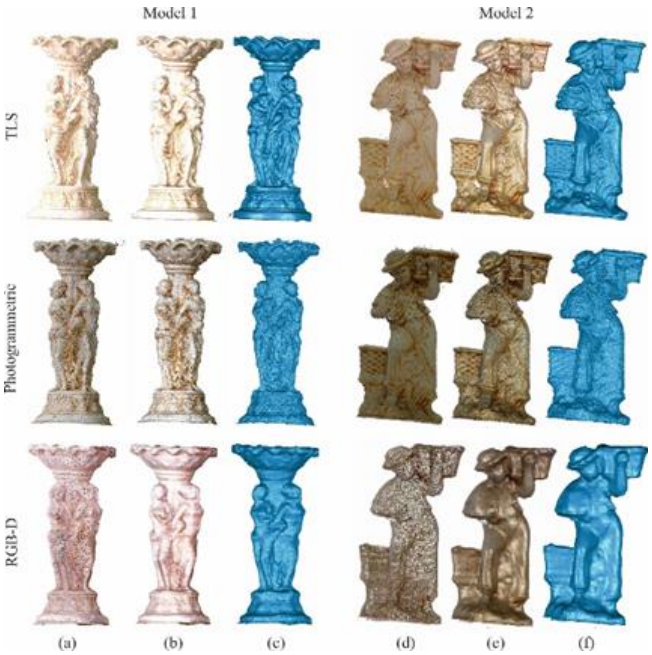

Figure 1. Model 1 (a) Point Cloud, (b) Mesh Model, and (c) Solid Model, Model 2 (d) Point Cloud, (e) Mesh Model and (f) Solid Model

3.1. Gaussian Filtering Method

With the development of computational capabilities of computers, the Gaussian Filters, which require high computational power, are applied to PCs. The Gaussian filter is a low pass filtering, which uses Gaussian functions to produce the result. Although Gaussian filters cause loss of detail in data, they are fast and simple. There are also Gaussian derivative filters, such as the bilateral filters, which are developed to limit the loss of data caused by the Gaussian filter. *k* is the closest neighboring point set of the $f_{(x,y,z)}$ vertex (Adams et al., 2009; Tercan 2018; Wirjadi and Breuel 2005). The Euclidean distance between these vertex points and nearest neighbor points are calculated using Equation (1).

$$d = dist\left(f_{(x,y,z)}, k\right) \tag{1}$$

The distance values calculated using Equation (1) are converted to Gaussian weight values using Equation (2);

$$G_\sigma(p) = \frac{1}{2\pi\sigma^2} e^{-\frac{d^2}{2\sigma^2}} \tag{2}$$

As the σ value changes in Equation (2), the solid model is changed. While determining the value requires expertise and experience, visual value can be estimated by applying statistical tests. In this paper, the optimum σ value was selected as 0.4 mm, experimentally. When the weight values obtained by using Equation (2) are used to fuse the positions of *k* vertexes, the corresponding vertex is filtered. This was expressed by;

$$W_{f_{(x,y,z)}} = G_\sigma(p)k \tag{3}$$

To achieve more optimum results in 3D Gaussian filtering, the expression shown in Equation (3) may have better results by changing the confidence interval (Adams et al., 2009; Tercan, 2018; Wirjadi and Breuel, 2005). When the Gaussian filtering results are examined in Figure 4 and Figure 5, it is seen that the photogrammetric method has more detail and noise compared to RGB-D data. This is a result of the fact that the RGB-D data has less accuracy and density than the photogrammetric data. Similarly, the filtered photogrammetric data is closer to the reference data than the filtered RGB-D data.

3.2 The Shepard Inverse Distance Weighting Method

The Shepard Inverse Distance Weighting (IDW) method is based on giving more weight to close neighborhoods than the distant vertex neighborhoods. When a point selected within the PC is filtered, utilization of points closer to that point increases the quality of filtering. Because of the law of the instrument, an instrument is more affected by what is close to them. The IDW method, which is a deterministic method, is used in the suppression of peak and pit noise. In contrast, this

filter tends to disrupt the natural form of the model to be obtained by causing an increase in the number of iterations, resulting in shrinkage in the data. The weighting strategy used in the IDW filtering method is defined using Equation (4);

$$w_i = \frac{d^{p}{}_i}{\sum_{j=1}^{n} d_i^{\,p}} \tag{4}$$

Here, d is the Euclidean distance between the vertex to be filtered and its neighbor w is the weight value. The p shown in Equation (4) is known as the power parameter and is usually taken as 2. The Euclidean distance between the point to be filtered and the neighboring points of this point are calculated using the Equation (5);

$$d_i = \sqrt{(\mathrm{x}-\mathrm{x}_i)^2 + (\mathrm{y}-\mathrm{y}_i)^2 + (\mathrm{z}-\mathrm{z}_i)^2} \tag{5}$$

According to the calculated distance, the points are weighted (Babak and Deutsch, 2009; Lu and Wong, 2008);

$$f(x,y,z) = \sum_{i=1}^{n} w_i f_i \tag{6}$$

3.3. Singular Value Decomposition Based Plane Fitting Method

The SVD method yields matrix factorization that is used in many areas such as dimensionality reduction, plane fitting, and feature extraction. Using the SVD method, an $X_{(\mathrm{n,n})}$ can be defined using Equation (7);

$$X = USV^T \tag{7}$$

$U_{(\mathrm{n,n})}$ consists of three principal components, $V_{(\mathrm{n,n})}$ consists of three eigenvectors, which corresponded to eigenvalues, respectively. $S_{(\mathrm{n,n})}$ diagonal matrix is the square matrix representing the singular values, $\sigma_1 > \sigma_2 > \ldots\ldots > \sigma_n$. General form of matrix X ;

$$\sum_{i=1}^{n} u_i \sigma_i v_i^T = [u_1, u_2, \ldots, u_n] \times \begin{pmatrix} \sigma_1 & \cdots & 0 \\ M & O & M \\ 0 & L & \sigma_n \end{pmatrix} \times [v_1, v_2, \ldots, v_n] \tag{8}$$

PC contains 3D spatial information and the third principal component has the lowest variance. That is, the third eigenvector is approximately the normal direction of the local plane obtained from the nearest neighborhood of the filtered point (Golub and Reinsch, 1971; Kurban 2014). The steps of the Single Value Decomposition Based Plane Fitting solution are below;

1) Set the vector, p consists of neighboring points of the point to be filtered (r),
2) $c = mean(p,\ 1)$ is the average of the vector,
3) Normalize the c vector; $M = [p_1 - c; p_2 - c; \ldots; p_n - c]$, $USV = SVD(M)$
4) Here, $USV = SVD(M)$ and $n = V(:, end)$ gives the local plane normal direction.
5) r_0 is the projected point on the local plane obtained by $(r - r_0) \cdot n = 0$

3.4. Optimization Based Plane Fitting Method

The problem of plane fitting is one of the problems in literature. In the case of a plane fitting problem, a vector, p , is selected from the nearest neighbor of each point to be filtered and fits the local plane to these points. Then, the point to be filtered in the PC is projected on the local plane. The parameters representing the plane can also be calculated with the least-squares method, SVD method, Levenberg-Marquardt method, or evolutionary computation tools (Bellekens, et al. 2014; Civicioglu, 2013; Civicioglu et al. 2020; Gunen et al. 2020). The objective function used to obtain the coefficients of the local plane to be represented by the p vector is given in Equation (9).

$$\underset{a,b,d}{\operatorname{argmin}} \sum |ax + by + cz - d| \mid c = 1 \tag{9}$$

In order to obtain the projected point, $r_{(\mathrm{x}_0,\mathrm{y}_0,\mathrm{z}_0)}$, in the local plane parametric equation can be used.

$$\frac{x-u}{a} = \frac{y-v}{b} = \frac{z-w}{c} = t \tag{10}$$

Here, $r_{(u,v,w)}$ is the point to be filtered. The parametric equation can be converted to Equation (11).

$$\begin{aligned} x &= u + a \times t \\ y &= v + b \times y \\ z &= w + c \times t \end{aligned} \tag{11}$$

From here Equation (12) is obtained.

$$a \times (u + a \times t_0) + b \times (v + b \times t_0) + c \times (w + c \times t_0) + d = 0 \tag{12}$$

If t_0 is isolated, then Equation (13) is obtained.

$$t_0 = -\frac{au + bv + cw + d}{a^2 + b^2 + c^2} \tag{13}$$

By developing Equation (13).

$$\begin{aligned} x_0 &= u + a \times t_0 \\ y_0 &= v + b \times y_0 \\ z_0 &= w + c \times t_0 \end{aligned} \tag{14}$$

The distance between points $r_{(u,v,w)}$ and $r_{(\mathrm{x}_0,\mathrm{y}_0,\mathrm{z}_0)}$ is calculated using Equation (15).

$$d = (\mathrm{u}-\mathrm{x}_0)^2 + (\mathrm{v}-\mathrm{y}_0)^2 + (\mathrm{w}-\mathrm{z}_0)^2 \tag{15}$$

Then the coordinates of $r_{(x_0,y_0,z_0)}$ are obtained with Equation (16).

$$x_0 = u - a\frac{au+bv+cw+d}{a^2+b^2+c^2}$$
$$y_0 = v - b\frac{au+bv+cw+d}{a^2+b^2+c^2} \quad (16)$$
$$z_0 = w - c\frac{au+bv+cw+d}{a^2+b^2+c^2}$$

The steps of the Optimization Based Plane Fitting solution are below;

ax+by+cz+d=0 | c=1 represents the local plane.

1. Set the vector, p, which consists of neighboring points of point to be filtered ($r_{(u,v,w)}$),
2. Repeat the following steps until it reaches the specified error criterion for each point or during iteration,
2.1. Determining the plane parameters (a,b,c,d),
2.2. Calculate the projection, $r_{(x_0,y_0,z_0)}$, of the point, $r_{(u,v,w)}$, in the local plane,
2.3. Memorize the new location of the point,
3. End the process.

Evolutionary computational methods can provide more consistent solutions for plane fitting problems than classical methods. Also, they are used to solve non-linear, non-derivative complex problems. Also, evolutionary computational algorithms do not easily trap local solutions (Tercan et al. 2020). In this paper, the Backtracking Search Optimization Algorithm (BSA) was used to solve the parameters of the local plane.

BSA (Civicioglu, 2013) is an evolutionary search algorithm developed by Civicioglu to solve real-value optimization problems. Compared to various evolutionary algorithms, BSA produces simpler results for problems such as surface fitting. The initial value in the problem solution is not dependent on the single control parameter it has. The mixrate, controls the crossover process, is the only control parameter. When creating new populations, it uses crossover and mutation operators as in the classical differential search algorithm. The search strategy and boundary control that it uses when creating a new population has enabled a very powerful exploration and exploitation skill (Civicioglu, 2013). In this experiment, dimension of pattern matrix is determined as 50. Stopping conditions are given below;

1.Stop when the maximum number of iterations is 500.
2.Stop if a better solution could not be obtained in the last 20 function evaluations.
3.Stop if the absolute value of the solution obtained for the algorithm is less than 10-16.

The BSA pseudo code is given in Figure 2.

Input: $ObjFun$, N, D, $maxcycle$, $mixrate$, $low_{1:D}$, $up_{1:D}$
Output: $globalminimum$, $globalminimizer$
// $rnd \sim U(0,1), rndn \sim N(0,1), w = rndint(\cdot), rndint(\cdot) \sim U(1,\cdot) \mid w \in \{1,2,3,\ldots,\cdot\}$
1 *function* $bsa(ObjFun, N, D, maxcycle, low, up)$
// INITIALIZATION
2 $globalminimum = inf$
3 **for** i **from** 1 **to** N **do**
4 **for** j **from** 1 **to** D **do**
5 $P_{i,j} = rnd \cdot (up_j - low_j) + low_j$ // Initialization of population, P.
6 $oldP_{i,j} = rnd \cdot (up_j - low_j) + low_j$ // Initialization of oldP.
7 **end**
8 $fitnessP_i = ObjFun(P_i)$ // Initial-fitness values of P
9 **end**
10 **for** $iteration$ **from** 1 **to** $maxcycle$ **do**
// SELECTION-I
11 **if** $(a < b | a, b \sim U(0,1))$ **then** $oldP := P$ **end**
12 $oldP := permuting(oldP)$ // 'permuting' arbitrary changes in positions of two individuals in oldP.
13 **Generation of Trial-Population**
// MUTATION
14 $mutant = P + 3 \cdot rndn \cdot (oldP - P)$
// CROSSOVER
15 $map_{1:N,1:D} = 1$ // Initial-map is an N-by-D matrix of ones.
16 **if** $(c < d | c, d \sim U(0,1))$ **then**
17 **for** i **from** 1 **to** N **do**
18 $map_{i,u(1:\lceil mixrate \cdot rnd \cdot D \rceil)} = 0 \mid u = permuting(\langle 1,2,3,\ldots,D \rangle)$
19 **end**
20 **else**
21 **for** i **from** 1 **to** N **do**, $map_{i,randi(D)} = 0$, **end**
22 **end**
// Generation of Trial Population, T
23 $T := mutant$
24 **for** i **from** 1 **to** N **do**
25 **for** j **from** 1 **to** D **do**
26 **if** $map_{i,j} = 1$ **then** $T_{i,j} := P_{i,j}$
27 **end**
28 **end**
// Boundary Control Mechanism
29 **for** i **from** 1 **to** N **do**
30 **for** j **from** 1 **to** D **do**
31 **if** $(T_{i,j} < low_j) or (T_{i,j} > up_j)$ **then**
32 $T_{i,j} = rnd \cdot (up_j - low_j) + low_j$
33 **end**
34 **end**
35 **end**
36 **end**
// SELECTION-II
37 $fitnessT = ObjFnc(T)$
38 **for** i **from** 1 **to** N **do**
39 **if** $fitnessT_i < fitnessP_i$ **then**
40 $fitnessP_i := fitnessT_i$
$P_i := T_i$
41 **end**
42 **end**
43 $fitnessP_{best} = min(fitnessP) \mid best \in \{1,2,3,\ldots,N\}$
44 **if** $fitnessP_{best} < globalminimum$ **then**
45 $globalminimum := fitnessP_{best}$
$globalminimizer := P_{best}$
// Export globalminimum and globalminimizer
46 **end**
47 **end**

Figure 1. The Pseudo Code of the Backtracking Search Optimization Algorithm (Civicioglu, 2013)

4. Experimental Results and Discussion

Geodetic measurement systems, by their nature, produce noisy data of various types and amplitudes, which are unpredictable. The most important method of achieving reliable measurements in an environment where the avoidance of noise is limited by physical reasons is to produce statistical measures based on multiple observations or to filter the measurements available. Post-process filtering is more suitable because repeated measurement is not always possible. The photogrammetric method and the data generated by the RGB-D sensor were filtered to consider the noise level of the instrument. The data to be filtered is compared with the TLS data and the amount of the average error by changing the number of neighbors depends on the filtering method. Figure 3.a and Figure 3.b are the results of Model 1 photogrammetric method and RGB-D sensor, respectively. When the two figures are examined together, the average error of filtering obtained with the RGB-D sensor is greater. While the Gaussian filter was the most unsuccessful in the photogrammetric method, the SVD method was the worst method in the RGB-D sensor. Because the planes created in SVD method are highly affected by noise. Figure 3.c and Figure 3.d belong to model 2. The results of model 2 photogrammetric and RGB-D sensors are given, respectively. As in model 1, the filtering results of RGB-D sensor produced a higher average error in Model 2. The Gaussian filter was the worst in the photogrammetric method, while the IDW

method produced very close results. The Gaussian method was the worst method in the RGB-D method and the SVD followed it. In both test models, according to the changing number of neighborhoods, the least error was given by the Optimization Based Plane Fitting method. Therefore, it has produced an average error of unpredictable magnitude due to the varying noise level in each model. Gaussian filtering yielded the highest average error.

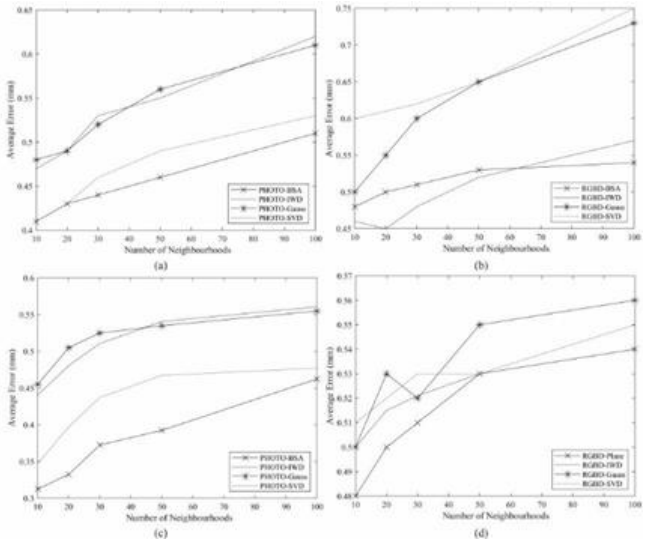

Figure 3. (a) Average Error of the Model 1 Photogrammetric Method, (b) Model 1RGB-D Sensor, (c) Average Error of Model 2 Photogrammetric Method, (d) Model 2 RGB-D Sensor

PCs from different methods were registered using RANSAC-based ICP. Because of the registration, the Euclidean distance calculated between the filtered data and the reference data and distance value were clustered. The cluster labels allow visual evaluation of the differences between the filtered and reference data. Distance values, which are cluster labels, were changed to the pseudo colors red, turquoise, purple, white, and yellow. Thus, it was visually obtained which vertexes move in the filtered point cloud. The red color shows the least moving vertexes. Yellow color refers to the most moving vertex. In this paper, the nearest neighbor number was experimentally determined for visual representation as (10, 20, and 30). Using larger numbers of the neighboring vertex causes loss of detail in the data and using fewer vertexes prevents the generation of enough information to compare the filtered results. Different numbers of neighborhoods (10, 20, 30, 50, and 100) were used for better expression of the graph data in Figure 3. Figure 4 shows the results of filtering according to the number of model 1 neighborhoods and the solid models of these results. Figure 5 shows the results of filtering according to the number of model 2 neighborhoods and the solid models of these results.

Error values were calculated by comparing the PCs captured with RGB-D and photogrammetric methods with reference data. The calculated error values are assigned to the point cloud of the system where they are generated as pseudo color and then the mesh surface is formed. When the results of the filtering are examined with the error amounts and the colorless solid models, it can be said that the results of the filtering provide approximate values. As the number of neighborhoods increased, the closure and detail of the data gaps decreased. As the sigma value was changed in the Gaussian filtering technique, the surface softness was changed but the most appropriate value was experimentally determined to be 0.4mm. The effect of this change on the result can be examined by a further study. Increasing the power parameter in the IDW filters may impair the result quality of the data. The SVD and Optimization Based Plane Fitting filter methods work differently from others because the surface parameter is fitted by calculating the projection of the point to the surface. Moreover, in some places on the surface, there are discontinuous transitions. The Optimization Based Plane Fitting filter with better quality than the SVD based method has been found to obtain solutions. Free-form surfaces can be used instead of the plane to increase the surface continuity effect in projection-based filtering.

5. CONCLUSION

PCs suffer from unpredictable and uncontrollable noise types with variable amplitude, due to the general error characteristics of the data capture environment conditions and the hardware used to capture related data. The noise, which disturbs the quality of PCs must be suppressed by using several filtering methods, such as the spatial filtering techniques mentioned in this paper. The most important method of achieving reliable measurements in an environment where the avoidance of noise is limited by physical reasons is to produce measures based on multiple observations or to filter the measurements available. In this paper, test model PCs were obtained using Terrestrial Laser Scanner, the Photogrammetric Method, and RGB-D sensors. The obtained point clouds were filtered according to the number of neighborhoods at three different levels using the Shepard Inverse Distance Weighting method, Gaussian Filtering method, Single Value Decomposition Based Filtering, and Optimization Based Plane Fitting. The Backtracking Search Optimization Algorithm, which works to find the best values for the parameters of the system or model in different conditions, has been used to determine the local plane parameters. Thus, the successes of the measurement systems as well as the success of filtering methods were examined. Although the proposed method provides effective results, it does not make sense to compare it in terms of CPU time consumption. Because evolutionary computation-based methods generally work slower than classical methods. Based on the statistical and visual results obtained, the Optimization Based Plane Fitting Method using Backtracking Search Optimization Algorithm gave the best result.

In future studies, comparisons will be made with detailed analysis using evolutionary calculation-based methods that use different strategies to filter PC.

ACKNOWLEDMENT

This paper forms part of Mehmet Akif Günen's master's thesis and supported by the projects: Erciyes University BAP FYL-2013-4330 and Tubitak 115Y235.

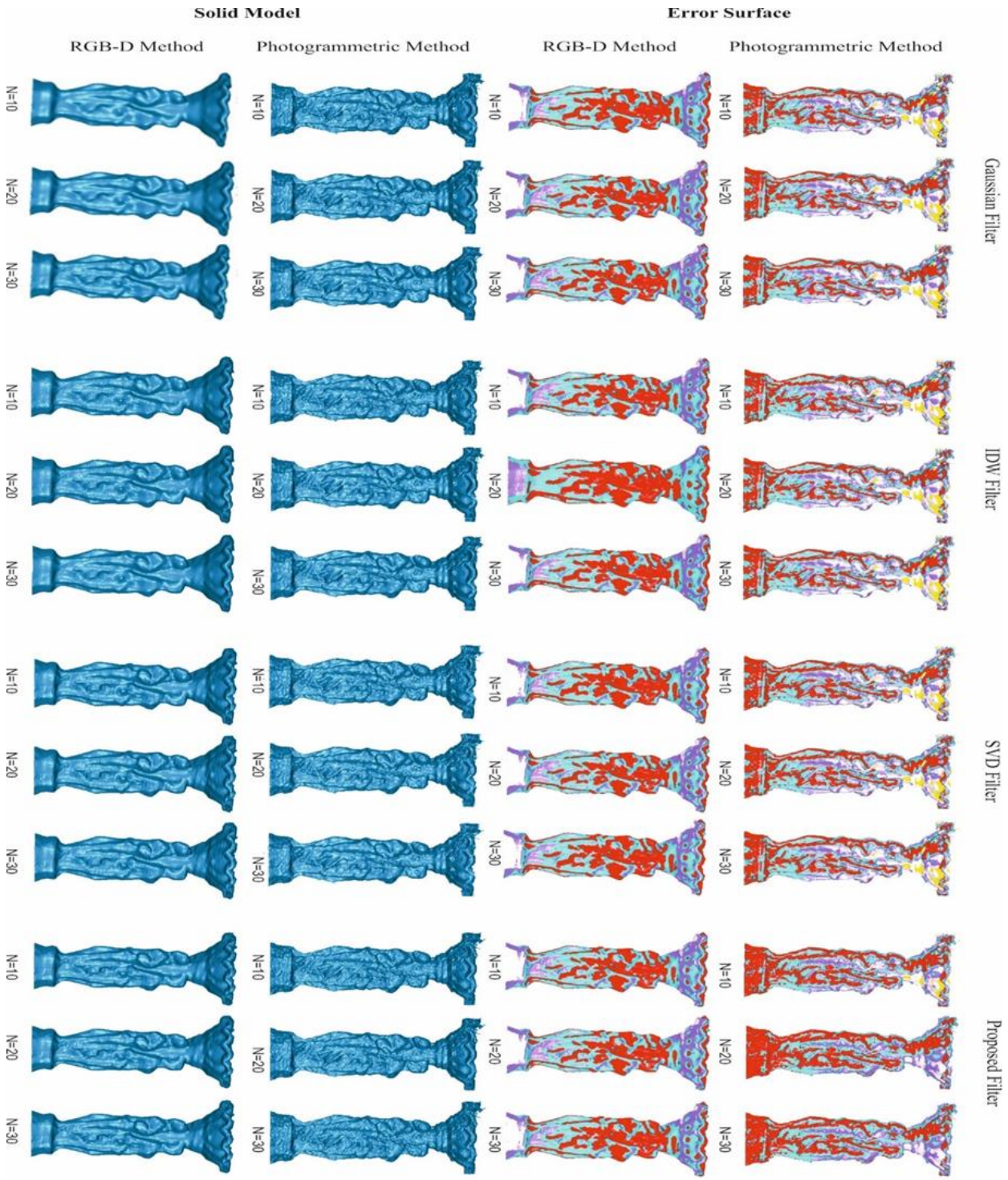

Figure 4. The solid model and error surfaces generated by applying specified filtering methods with different neighborhood number (N) in Model 1 produced by the Photogrammetric and RGB-D methods

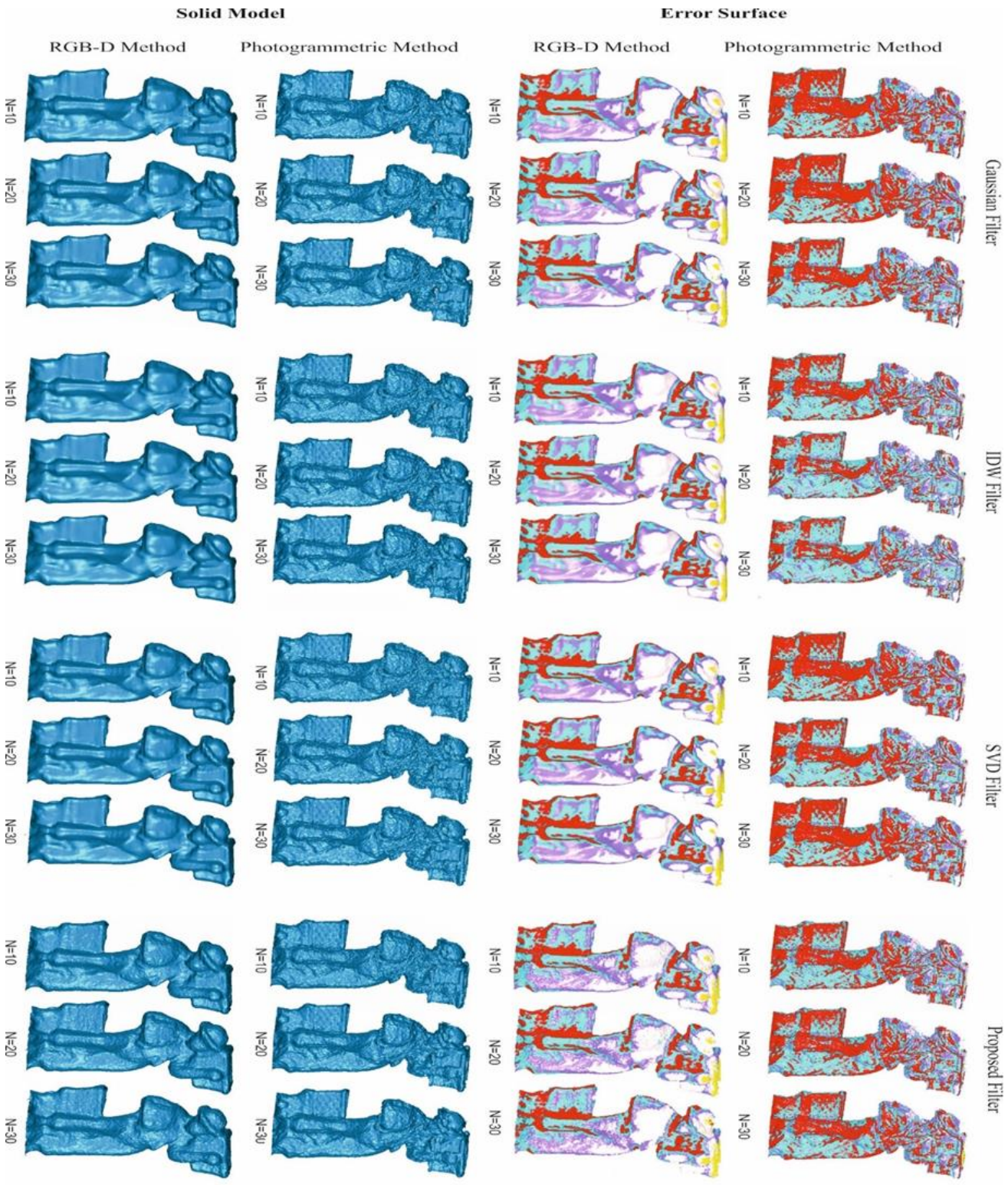

Figure 5. The solid model and error surfaces generated by applying specified filtering methods with different neighborhood number (N) in Model 2 produced by the Photogrammetric and RGB-D methods.

REFERENCES

Adams A, Gelfand N, Dolson J & Levoy M (2009). Gaussian kd-trees for fast high-dimensional filtering. ACM SIGGRAPH 2009. https://doi.org/10.1145/1576246.1531327

Aghababaee H, Ferraioli G, Schirinzi G & Pascazio V (2019). Regularization of SAR Tomography for 3-D Height Reconstruction in Urban Areas. IEEE Journal of Selected Topics in Applied Earth Observations and Remote Sensing, 12(2), 648-659.

Ahmadabadian A H, Karami A & Yazdan R (2019). An automatic 3D reconstruction system for texture-less objects. Robotics and Autonomous Systems, 117, 29-39.

Altuntas C (2015). Integration of point clouds originated from laser scanner and photogrammetric images for visualization of complex details of historical buildings. The International Archives of Photogrammetry, Remote Sensing and Spatial Information Sciences, 40(5), 431.

Amenta N (1999). The crust algorithm for 3 D surface reconstruction. Symposium on Computational geometry, 423-424.

Babak O & Deutsch C V (2009). Statistical approach to inverse distance interpolation. Stochastic Environmental Research and Risk Assessment, 23(5), 543-553.

Bellekens B, Spruyt V, Berkvens R & Weyn M (2014). A survey of rigid 3D point cloud registration algorithms. International Journal on Advances in Intelligent Systems, 8, 118-127.

Cai S, Zhang W, Liang X, Wan P, Qi J, Yu S & Shao J (2019). Filtering airborne LiDAR data through complementary cloth simulation and progressive TIN densification filters. Remote Sensing, 11(9), 1037.

Civicioglu P (2013). Backtracking search optimization algorithm for numerical optimization problems. Applied Mathematics and Computation, 219(15), 8121-8144.

Civicioglu P, Besdok E, Gunen M A & Atasever U H (2020). Weighted differential evolution algorithm for numerical function optimization: a comparative study with cuckoo search, artificial bee colony, adaptive differential evolution, and backtracking search optimization algorithms. Neural Computing and Applications, 32, 3923–3937.

Doğan Y & Yakar M (2018). GIS and three-dimensional modeling for cultural heritages. International Journal of Engineering and Geosciences, 3(2), 50-55.

Fleishman S, Drori I & Cohen-Or D (2003). Bilateral mesh denoising. ACM Transactions on Graphics (TOG), 950-953.

Garcia-Garcia A, Orts-Escolano S, Garcia-Rodriguez J & Cazorla M (2018). Interactive 3D object recognition pipeline on mobile GPGPU computing platforms using low-cost RGB-D sensors. Journal of Real-Time Image Processing, 14(3), 585-604.

Golub G H & Reinsch C (1971). Singular value decomposition and least squares solutions. In Linear Algebra (pp. 134-151): Springer, Berlin, Heidelberg

Gunen M A (2017). Comparison of point cloud filtering algorithms. Master's Thesis, Erciyes University, Kayseri.

Gunen M A, Atasever Ü H, Taşkanat T & Besdok E (2019). Usage of unmanned aerial vehicles (UAVs) in determining drainage networks. Nature Sciences, 14(1), 1-10.

Gunen M A, Besdok E, Civicioglu P & Atasever U H (2020). Camera calibration by using weighted differential evolution algorithm: a comparative study with ABC, PSO, COBIDE, DE, CS, GWO, TLBO, MVMO, FOA, LSHADE, ZHANG and BOUGUET. Neural Computing and Applications.

Gunen M A, Çoruh L & Besdok E (2017). Oyun Dünyasında Model Ve Doku Üretiminde Fotogrametri Kullanımı. Geomatik, 2(2), 86-93.

Gunen M A, Kesikoglu A, Karkinli A E & Besdok E (2017). RGB-D sensörler ile iç mekan haritalamasi [Turkish-only]. International Artificial Intelligence and Data Processing Symposium (IDAP).

Han X-F, Jin J S, Wang M-J, Jiang W, Gao L & Xiao L (2017). A review of algorithms for filtering the 3D point cloud. Signal Processing: Image Communication, 57, 103-112.

Hoppe H, DeRose T, Duchamp T, McDonald J & Stuetzle W (1992). Surface reconstruction from unorganized points. Proceedings of the 19th annual conference on Computer graphics and interactive techniques (pp. 71-78).

Hou W, Chan T & Ding M (2012). Denoising point cloud. Inverse Problems in Science and Engineering, 20(3), 287-298.

Javernick L, Brasington J & Caruso B (2014). Modeling the topography of shallow braided rivers using Structure-from-Motion photogrammetry. Geomorphology, 213, 166-182.

Jia C, Yang T, Wang C, Fan B & He F (2019). A new fast filtering algorithm for a 3D point cloud based on RGB-D information. PloS one, 14(8).

Juan L & Gwon O (2009). A comparison of sift, pca-sift and surf. International Journal of Signal Processing, Image Processing and Pattern Recognition, 8(3), 169-176.

Kurban T (2014). 3 Boyutlu Nesnelerin Modellenmesi İçin Nokta Bulutlarının Sezgisel Optimizasyon Yöntemleri İle İşlenmesi. PhD Thesis, Erciyes Universitesi, Kayseri.

Li Y, Snavely N, Huttenlocher D & Fua P (2012). Worldwide pose estimation using 3d point clouds. European conference on computer vision.

Lu G Y & Wong D W (2008). An adaptive inverse-distance weighting spatial interpolation technique. Computers & Geosciences, 34(9), 1044-1055.

Narváez E A L & Narváez N E L (2006). Point cloud denoising using robust principal component analysis. GRAPP, 51-58.

Nyarko E K, Vidović I, Radočaj K & Cupec R (2018). A nearest neighbor approach for fruit recognition in RGB-D images based on detection of convex surfaces. Expert Systems with Applications, 114, 454-466.

Oliveira A, Oliveira J F, Pereira J M, De Araújo B R & Boavida J (2014). 3D modelling of laser scanned and photogrammetric data for digital documentation: the Mosteiro da Batalha case study. Journal of real-time image processing, 9(4), 673-688.

Sevgen S C (2019). Airborne lidar data classification in complex urban area using random forest: a case study of Bergama, Turkey. International Journal of Engineering and Geosciences, 4(1), 45-51.

Stückler J, Waldvogel B, Schulz H & Behnke S (2015). Dense real-time mapping of object-class semantics from RGB-D video. Journal of real-time image processing, 10(4), 599-609.

Tercan E (2017). İnsansız hava aracı kullanılarak antik kent ve tarihi kervan yolunun fotogrametrik belgelenmesi: Sarıhacılar örneği. Mühendislik Bilimleri ve Tasarım Dergisi, 5(3), 633-642.

Tercan E (2018). Karayolu ölçmelerinde insansız hava araçlarının kullanılması: Okurcalar şehir merkezi örneği. Ömer Halisdemir Üniversitesi Mühendislik Bilimleri Dergisi, 7(2), 649-660.

Tercan E, Besdok E & Tapkın S (2020). Heuristic Modelling of traffic accident characteristics. Transportation Letters, 1-9.

Tölgyessy M & Hubinský P (2011). The kinect sensor in robotics education. Proceedings of 2nd International Conference on Robotics in Education, 143-146.

Ulvi A (2018). Analysis of the utility of the unmanned aerial vehicle (UAV) in volume calculation by using photogrammetric techniques. International Journal of Engineering and Geosciences, 3(2), 43-49.

URL https://faro.app.box.com/s/ou88y63qotb5cnid5610nc570z74cpsu/file/441669813395, Accessed on: 2 October 2019.

Vock R, Dieckmann A, Ochmann S & Klein R (2019). Fast template matching and pose estimation in 3D point clouds. Computers & Graphics, 79, 36-45.

Wirjadi O & Breuel T (2005). Approximate separable 3D anisotropic Gauss filter. IEEE International Conference on Image Processing, Genova, Italy.

Wolff K, Kim C, Zimmer H, Schroers C, Botsch M, Sorkine-Hornung O & Sorkine-Hornung A (2016). Point cloud noise and outlier removal for image-based 3D reconstruction. Fourth International Conference on 3D Vision (3DV), 118-127.

Xiang T & Cheong L-F (2003). Understanding the behavior of SFM algorithms: A geometric approach. International journal of computer vision, 51(2), 111-137.

Yu J, McMillan L & Gortler S (2004). Surface camera (scam) light field rendering. International Journal of Image and Graphics, 4(04), 605-625.

International Journal of Engineering and Geosciences

https://dergipark.org.tr/en/pub/ijeg

e-ISSN 2548-0960

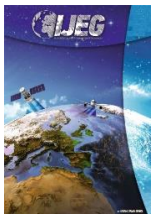

Fully optimized multilayer radar absorber design using multi-objective abc algorithm

Enes Yigit[1], **Huseyin Duysak** *[1]

[1]*Karamanoglu Mehmetbey University, Engineering Faculty, Department* of *Electrical-Electronics Engineering, Karaman, Turkey*

Keywords
Multi-objective optimization
Pareto front
Radar absorbing material (RAM)
Triple objective ABC

ABSTRACT

Main purpose of the design of multi-layer radar absorber (MRA) by means of metaheuristic optimization algorithms is to minimize both the total thickness (TT) of MRA and the maximum reflection coefficients for transverse electric (RTE) & transverse magnetic (RTM) polarizations at any oblique angle of incidence. For this purpose, sequence and thicknesses of layers of the MRA have been optimized by either single-objective approach based on combining all objectives or double-objective approach in which TT is evaluated separately from the reflection coefficients. In this study, triple-objective artificial bee colony (TO-ABC) algorithm integrated with Pareto front technique is proposed for fully optimized MRA design. Thus, both RTE, RTM and TT are simultaneously minimized by optimizing thickness, sequence and number of the layers. To demonstrate the superiority of TO-ABC, 3 types of MRAs operating at the frequency ranges of 2–18 GHz for each angle of incidence from 0^0 to 60^0 are optimized and compared with the literature. Furthermore, 4 different real MRAs are also optimized using real materials given in the literature. Thanks to the developed graphical user interface and TO-ABC algorithm, despite the limited number of materials, all possible solutions providing the specified parameters are easily achieved and successful MRA structures are designed.

1. INTRODUCTION

Electromagnetic (EM) stealth technology is an important issue which has increased its popularity in the last quarter century and has many commercial and military applications. The main purpose of this technology is to reduce the EM energy scattered from the target as much as possible and to make the target invisible to the radar receiver. Within this scope, multi-layer radar absorbers (MRA) have become very popular in recent years due to their superior absorption capabilities (Yigit and Duysak, 2019a). To produce the MRA having low thickness and low reflection properties, the sequence and thickness of the materials used in the layers should be optimally determined. For this purpose, natural-inspired optimization algorithms such as artificial bee colony (ABC)(Toktas et al., 2018), central force algorithm (CFO) (Asi and Dib, 2010), particle swarm optimization (PSO)(Goudos and Sahalos, 2006a) , genetic algorithm (GA) (Kern and Werner, 2003) and differential evolution (DE) (Goudos, 2009) and also surrogate-based optimization(Toktas et al., 2019) have been successfully applied to various MRA designs operating at different frequency ranges between 0.2–18 GHz (Asi and Dib, 2010; Goudos, 2009; Goudos and Sahalos, 2006a, 2006b; Jiang et al., 2009; Kern and Werner, 2003; Michielssen et al., 1993; Ranjan et al., 2018; Roy et al., 2016, 2015; Toktas et al., 2019, 2018; Weile et al., 1996; Yigit and Duysak, 2019a). Most of these studies were performed either for normal incidence or for a limited angle of incidence. Broad-band and wide-angle MRAs should be designed for practical implementations of the stealth technologies. However, the design of broad-band and wide-angle MRA with as thin as possible is a challenging problem. In all of the studies given in references (Asi and Dib, 2010; Goudos, 2009; Goudos and Sahalos, 2006a, 2006b; Jiang et al., 2009; Kern and Werner, 2003; Michielssen et al., 1993; Ranjan et al., 2018; Roy et al., 2016, 2015; Toktas et al., 2019, 2018; Weile et al., 1996), where predefined 16 virtual materials were preferred, MRA designs were performed by means of either single objective (Asi and Dib, 2010; Goudos, 2009; Goudos and Sahalos, 2006a; Kern and Werner, 2003; Michielssen et al., 1993; Ranjan

* **Corresponding Author**

(enesyigit@kmu.edu.tr) ORCID ID 0000 – 0002 – 0960 – 5335
*(huseyinduysak@kmu.edu.tr) ORCID ID 0000 – 0002 – 2748 – 0660

Cite this article

Yiğit E & Duysak H (2021). Fully optimized multilayer radar absorber design using multi-objective abc algorithm. International Journal of Engineering and Geosciences, 6(3), 136-145

Research Article / DOI: 10.26833/ijeg.743661

Received: 27/05/2020; Accepted: 22/12/2020

et al., 2018; Roy et al., 2016, 2015; Toktas et al., 2018) or multi-objective (MO) approaches (Goudos and Sahalos, 2006b; Jiang et al., 2009; Toktas et al., 2018; Weile et al., 1996). In the MO approach, both thickness and reflection coefficients are optimized simultaneously, while in single objective optimization all objectives are combined in a single objective function by means of weight coefficients (Goudos, 2009). In addition, a new double-stage method has recently been introduced that optimizes the total thicknesses (TT) of layers separately from number & sequence of the layers (NSL) (Yigit and Duysak, 2019a) . Thanks to the double-stage approach, negative effects of sudden changes in layer sequence has been prevented (Yigit and Duysak, 2019a). However, similar to other single or MO approaches (Asi and Dib, 2010; Goudos, 2009; Goudos and Sahalos, 2006a, 2006b; Jiang et al., 2009; Kern and Werner, 2003; Michielssen et al., 1993; Ranjan et al., 2018; Roy et al., 2016, 2015; Toktas et al., 2019, 2018; Weile et al., 1996), in (Yigit and Duysak, 2019a) the reflection coefficients for Transverse Electric (TE) and Transverse Magnetic (TM) polarizations were combined in a single objective function. Satisfactory results can be achieved by combining different objective functions at the beginning of the algorithm, but in some special cases, it is inevitable that MO optimization is required for compromises between objectives. For example, in some cases, it may be desirable to minimize the maximum reflection coefficient by sacrificing TT. In this case, MO optimization approaches are inevitable.

In this study, three different objectives (TT, reflection coefficients for TE and TM polarizations) for fully optimized MRA design are synchronously minimized by means of Pareto-integrated triple objective ABC (TO-ABC) algorithm. In MRA design problem, it is not a reasonable approach to set a minimum or maximum objective for the number of layers (NL). As it can be seen from (Yigit and Duysak, 2019a), much thinner structures can be designed by using more layers. Therefore, in this study, NSL is simultaneously optimized with thicknesses. A graphical user interface (GUI) is designed on the MATLAB platform to easily obtain possible solutions on the Pareto front. The effectiveness of the method is demonstrated by using both 16 predefined virtual materials (Michielssen et al., 1993) and up-to-date 21 real materials(Yigit and Duysak, 2019a). The designed structures are compared with the similar multi-layer radar absorbers in the literature(Ranjan et al., 2018). 3 different designs (for TE/TM modes) effective at the frequency band of 2-8 GHz, 12-18 GHz and 2-18 GHz at the angles of incident between 0^0 and 60^0 are optimized. In addition, 4 different MRA structures are also designed, which consist entirely of real materials, operating across the entire band from 2 to 18 GHz for all angles of incident between 0^0 and 60^0.

The physical model of the MRA design and the basic theory of the ABC algorithm are briefly presented in the next section. In Section III, the detailed information of TO-ABC is presented. The implementation of the TO-ABC algorithm and optimized MRA designs are given in Section IV. The concluding remarks and possible further studies are mentioned in the conclusion section.

2. PHYSICAL MODEL of MRA STRUCTURE and ABC ALGORITHM

2.1. Physical Model of MRA Structure

A basic MRA structure consists of different materials coated on a perfect electric conductor. Each layer is defined by different electrical properties and different thickness. The main purpose of the MRA design is to determine the NSL and TT, to minimize the back scattered energy for TE & TM polarizations for desired angle of incidences and frequencies. While the EM wave travels through each layer, it is exposed to the transmission, the absorption and the reflection effects in the each layer. Therefore, the total surface reflection of the MRA depends on the alignment of the entire structure. Since the detailed formulation of MRA design problem was given in many studies (Asi and Dib, 2010; Goudos, 2009; Goudos and Sahalos, 2006a, 2006b; Jiang et al., 2009; Kern and Werner, 2003; Michielssen et al., 1993; Ranjan et al., 2018; Roy et al., 2016, 2015; Toktas et al., 2019, 2018; Weile et al., 1996; Yigit and Duysak, 2019a), in this study only the basic equations are given and critical points are indicated. In the polarization-insensitive MRA design, the back-scattered energy must be minimized in both TE and TM polarizations along with the TT of the MRA. Therefore, three objective functions ($\boldsymbol{OF_1}, \boldsymbol{OF_2}, \boldsymbol{OF_3}$) are defined as follow,

$$\begin{aligned} \text{minimize } \mathrm{OF}_1 &= maximum\,\{20log10(RTE)\} \\ \text{minimize } \mathrm{OF}_2 &= maximum\,\{20log10(RTM)\} \\ \text{minimize } \mathrm{OF}_3 &= TT \end{aligned} \tag{1}$$

where $\boldsymbol{RTM}$ and $\boldsymbol{RTE}$ are the reflection coefficient matrices, which includes the TM and TE polarizations corresponding to each of the defined angle of incidence and the frequency values. For an MRA structure with $\boldsymbol{M}$ (M^{th} layer is perfect electric conductor) layer, the RTE and RTM are defined as follows (Yigit and Duysak, 2019a),

$$\boldsymbol{R_i}^{\boldsymbol{TE}} = \frac{\boldsymbol{r_i}^{\boldsymbol{TE}} + \boldsymbol{R_{i+1}}^{\boldsymbol{TE}} \boldsymbol{e}^{-2j\boldsymbol{k_{i+1}}\boldsymbol{d_{i+1}}}}{\mathbf{1} + \boldsymbol{r_i}^{\boldsymbol{TE}} \boldsymbol{R_{i+1}}^{\boldsymbol{TE}} \boldsymbol{e}^{-2j\boldsymbol{k_{i+1}}\boldsymbol{d_{i+1}}}} \tag{2}$$

$$\boldsymbol{R_i}^{\boldsymbol{TM}} = \frac{\boldsymbol{r_i}^{\boldsymbol{TM}} + \boldsymbol{R_{i+1}}^{\boldsymbol{TM}} \boldsymbol{e}^{-2j\boldsymbol{k_{i+1}}\boldsymbol{d_{i+1}}}}{\mathbf{1} + \boldsymbol{r_i}^{\boldsymbol{TM}} \boldsymbol{R_{i+1}}^{\boldsymbol{TM}} \boldsymbol{e}^{-2j\boldsymbol{k_{i+1}}\boldsymbol{d_{i+1}}}} \tag{3}$$

where $\boldsymbol{d_i}$ corresponding to the thickness of each layer. The $\boldsymbol{r_i}^{\boldsymbol{TE}}$ and $\boldsymbol{r_i}^{\boldsymbol{TM}}$ are given as follows,

$$\mathbf{r_i}^{\mathbf{TE}} = \begin{cases} \dfrac{\boldsymbol{\mu_{i+1}}\mathbf{k_i} - \boldsymbol{\mu_i}\mathbf{k_{i+1}}}{\boldsymbol{\mu_{i+1}}\mathbf{k_i} + \boldsymbol{\mu_i}\mathbf{k_{i+1}}} & \mathbf{i < M} \\ -\mathbf{1}, & \mathbf{i = M} \end{cases} \;\&\; \mathbf{r_i}^{\mathbf{TM}} = \begin{cases} \dfrac{\boldsymbol{\varepsilon_{i+1}}\mathbf{k_i} - \boldsymbol{\varepsilon_i}\mathbf{k_{i+1}}}{\boldsymbol{\varepsilon_{i+1}}\mathbf{k_i} + \boldsymbol{\varepsilon_i}\mathbf{k_{i+1}}} & \mathbf{i < M} \\ \mathbf{1} & \mathbf{i = M} \end{cases} \tag{4}$$

According to the angle of incidence $\boldsymbol{\theta}^{\circ}$, the wave number $\boldsymbol{k_i}$, of the $\boldsymbol{i^{th}}$ layer is defined as,

$$k_i = 2\pi f\sqrt{\mu_i\varepsilon_i - \mu_0\varepsilon_0\, sin^2(\theta)} \tag{5}$$

In (4), while $\boldsymbol{\mu_i}$ and $\boldsymbol{\varepsilon_i}$ are the frequency($\boldsymbol{f}$) depended complex permeability and permittivity of the materials, $\boldsymbol{\mu_0}$ and$\boldsymbol{\varepsilon_0}$ are permeability and permittivity of free space,

respectively (Yigit and Duysak, 2019a). According to the (2) and (3), the TT of the structure is defined as follow,

$$TT = \sum_{i=1}^{M-1} d_i \quad (6)$$

2.2. Single-Objective ABC Algorithm for MRA Design

Natural inspired metaheuristic optimization techniques can produce satisfactory results which are close to the optimum result for nonlinear problems. ABC is an efficient algorithm inspired by the nectar search activities of honey bee swarms (Karaboga and Basturk, 2007). In the algorithm, the number of food sources (NS) specify the potential solutions of the problem, while the amount of nectar in the sources corresponds to fitness value of the solution. The details of the algorithm developed by modeling the behavior of employed, onlooker and scout bees are given in (Yigit and Duysak, 2019a). The changes made in these three phases in the MO-ABC algorithm are explained in detail in the next section.

3. MO-ABC ALGORITHM

3.1. Multi -Objective Optimization

In the single-objective optimization, optimum results can be obtained by comparing only the single value of the objective function. However, if there is more than one objective function, the problem is defined as a MO optimization problem and all objective functions are simultaneously optimized. The mathematical expression of MO optimization problem can be defined as follows.

$$minF(\chi) = [f_1(\chi), f_2(\chi), \dots\dots, f_{\Pi}(\chi)] \quad (7)$$

$$\chi = [x_1, x_2, \dots\dots, x_u] \in S \quad (8)$$

where $\boldsymbol{\Pi}$, $\boldsymbol{\chi}$ and $\boldsymbol{S}$ are the number of the objective functions, $\boldsymbol{u}$ dimensional decision variable vector and the search space, respectively. The solution of the multi-objective optimization problem is generally represented by a Pareto optimal set (Deb et al., 2002; Huo et al., 2015). For the minimization problems, if at least one objective value of the solution $\boldsymbol{\chi}$ is less than the other solution $\boldsymbol{\chi'}$, and all objective values of $\boldsymbol{\chi'}$ aren't less than $\boldsymbol{\chi}$, then $\boldsymbol{\chi}$ dominates $\boldsymbol{\chi'}$. However, if no solution dominates the solution $\boldsymbol{\chi'}$, ***then*** $\boldsymbol{\chi'}$ is called as the nondominated or Pareto-efficient solution. All Pareto solutions constitute elite solution (ES) set which are the possible solutions of the MO problem.

3.2. Multi-Objective ABC Algorithm

The MO-ABC algorithm includes four phase; initialization, employed bees, onlooker bees and scout bees. The flow chart of the algorithm is given in the Fig.1.

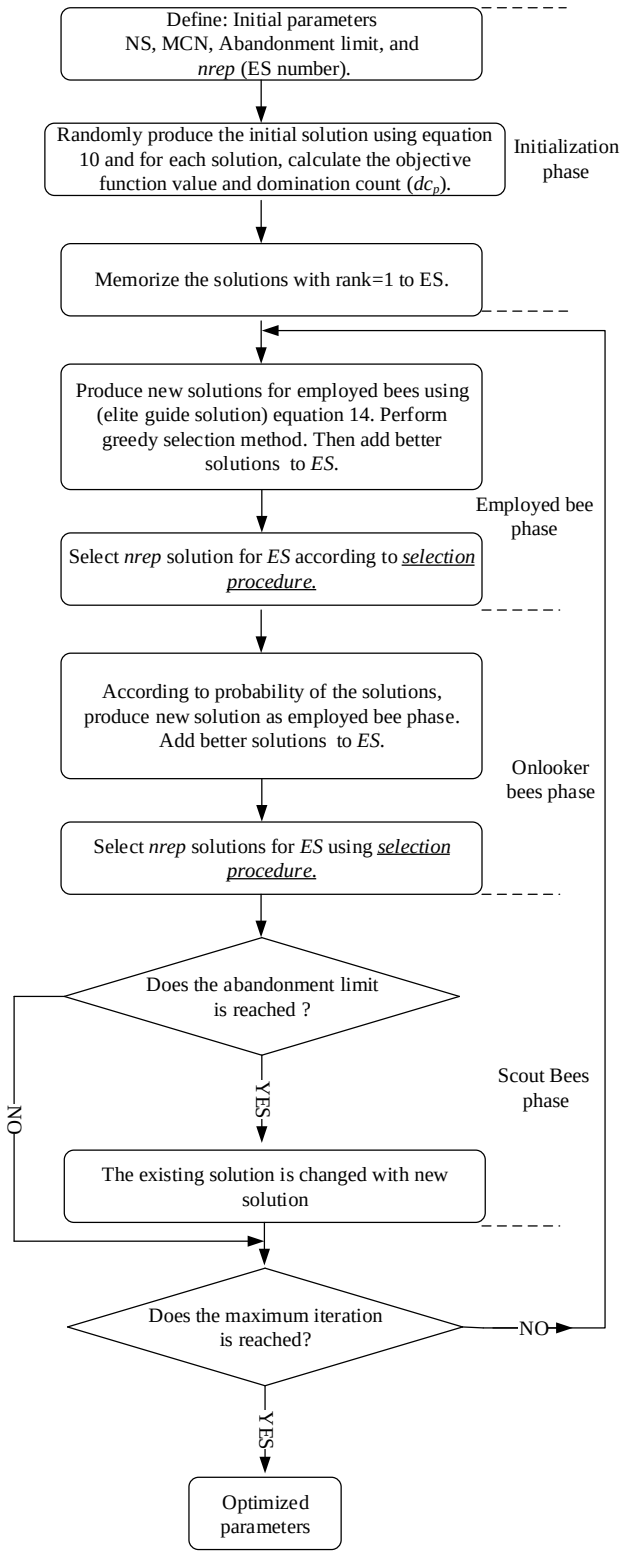

Figure 1. The flow chart of MOABC

1) Initialization

The population $\boldsymbol{P}$ of the bee swarm is defined as follows,

$$\boldsymbol{P} = \{\boldsymbol{\chi_1}, \boldsymbol{\chi_2}, \dots\dots, \boldsymbol{\chi_{NS}}\} \quad (9)$$

where $\boldsymbol{NS}$ is the number of food source. The initial food sources $\boldsymbol{\chi_p}$ are randomly generated by (10),

$$\chi_p = lb^d + rand(0,1)(ub^d - lb^d) \quad (10)$$

where $\boldsymbol{p} \in \{\mathbf{1}, \mathbf{2}, \ldots\ldots, \boldsymbol{NS}\}$ and $\boldsymbol{d} \in \{\mathbf{1}, \mathbf{2}, \ldots\ldots, \boldsymbol{u}\}$ are the solution vector index and dimension of $\boldsymbol{\chi_p}$, respectively. $\boldsymbol{lb}$ and $\boldsymbol{ub}$ are lower and upper bound of solution vectors.

- *Determination of elite solutions.*

In MO optimization, there are more than one objective function, so it is not simple to determine the non-dominated solutions. In this study, in order to sort and select the ES, fast nondominated sorting (Deb et al., 2002) requiring the less computations, is preferred.
For each solution, two parameters are calculated, these are;

1. Domination count, $\boldsymbol{dc_p}$: the number of solutions which dominate the solution $\boldsymbol{p}$,
2. $\boldsymbol{S_P}$: Set of the solutions dominated by solution $\boldsymbol{p}$.

In fast nondominated sorting method, the initial values of $\boldsymbol{dc_p}$ of all solutions in population are defined as zero. For each solution $\boldsymbol{p}$ in the population $\boldsymbol{P}$ is then compared with every other solution $\boldsymbol{q}$ in $\boldsymbol{P}$. If the solution $\boldsymbol{p}$ is better than $\boldsymbol{q}$, then $\boldsymbol{S_P}$=$\boldsymbol{S_P} \cup \{\boldsymbol{q}\}$, otherwise; $\boldsymbol{dc_p} = \boldsymbol{dc_p} + \mathbf{1}$. If $\boldsymbol{dc_p} = \mathbf{0}$, $\boldsymbol{dc_p}.\mathbf{rank} = \mathbf{1}$. Otherwise, $\boldsymbol{dc_p}$ corresponding to each member ($\boldsymbol{q}$) of $\boldsymbol{S_P}$ is reduced by one. When $\boldsymbol{dc_p}$ of $\boldsymbol{q}$ is zero, it is saved to the new $\boldsymbol{Q}$ list. This $\boldsymbol{Q}$ list constitutes the second nondominated front. This process continues until all front is determined (Deb et al., 2002). In this study, ES consists of the first nondominated front as illustrated in Fig. 2(a).

- *Crowding Distance*

The crowding-distance is obtained according to each objective function value of the Pareto points. For each objective function, the distance values of the largest and smallest points are assumed as an infinite. The initial values of the distances of all solutions are assigned as zero and then the distances of each solutions for each objective function are updated as follows (Deb et al., 2002).

$$dist_{m,j} = dis_{m,j} + \frac{f_{m,j+1} - f_{m,j-1}}{\max(f_m) - \min(f_m)} \tag{11}$$

where $\mathbf{dist_{m,j}}$ denotes distance of j^{th} solution of m^{th} objective function as illustrated in Fig. 2b.

The exact crowding-distance vector ($\mathbf{Cd_j}$) is obtained by summing the individual distance values corresponding to each objective as follows,

$$Cd_j = \sum_{m=1}^{\Pi} dist_{m,j} \tag{12}$$

- Selection procedure

The number of ES can be more than the desired number of archive, **nrep**. Therefore, population selection strategy must be applied to select solutions to constitute **ES**. Since the ranks of the all solutions in ES are equal to 1, the solutions with the higher distance should be selected.

For this purpose, the crowding distance values ($\mathbf{Cd}$) of all solutions are sorted in descending form and the first **nrep** solutions are selected.

2) Employed Bee Phase

In the employed bee phase, bees search new food sources to improve the existing solution. In the original ABC algorithm(Karaboga and Basturk, 2007), a new food source $\boldsymbol{\chi}'$ is generated by using (13) for each employed bee sources ($\mathbf{n} = \mathbf{1} \ldots \mathbf{NS}$),

$$\chi'_{nr} = \chi_{nr} + \phi(\chi_{nr} - \chi_{kr}) \tag{13}$$

where $\boldsymbol{\chi_{kr}}$ is neighbour solution of $\boldsymbol{\chi_{nr}}$ corresponding to the randomly generated $\mathbf{r} \in [\mathbf{1}, \mathbf{u}]$.

Original ABC algorithm don't use the ES or best solution. However, to effectively improve the solutions in MO-ABC, the new solutions must be updated based on the ES (Huo et al., 2015). In the second phase of the MO-ABC algorithm, a new food source is produced by the following equation (Huo et al., 2015),

$$\boldsymbol{\chi'}_{nr} = \boldsymbol{\chi}_{nr} + \phi(\boldsymbol{\chi}_{nr} - \boldsymbol{\chi}_{kr}) + \psi(\boldsymbol{y}_{nr} - \boldsymbol{\chi}_{kr}) \quad \boldsymbol{y}_{nr} \in \boldsymbol{ES} \tag{14}$$

where ϕ and ψ are random numbers in the ranges of [-1, 1] and [0, 2], respectively. $\mathbf{y_{nr}}$ denotes the randomly selected solution from **ES**.

The choice between the existing and new solutions is determined by means of the greed selection. If the existing solution is worse than the new solution, the abandonment counter is reset and $\mathbf{ES} = \mathbf{ES} \cup \{\boldsymbol{\chi}'_{\mathbf{n}}\}$; otherwise, the counter is increased. After all employed bees search new food source, **ES** is updated by performing the selection procedure.

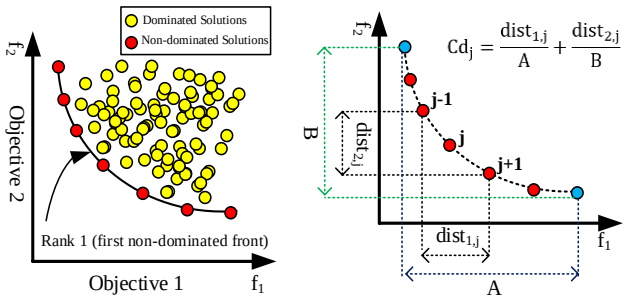

Figure 2. Illustration of the Pareto front points; a) Dominated and non-dominated solutions, b) Determination of Crowded distances

3) Onlooker Bee Phase

In the onlooker bee phase, in order to calculate the selection probability value, the fitness value of each solution must be calculated. For a single objective function, the fitness value is calculated as follows (Karaboga and Basturk, 2007)

$$fit(\chi_n) = \frac{1}{1 + f(\chi_n)} \tag{15}$$

However, in the MO optimization, since the number of objective functions is more than one, (15) is not applicable. Thus, the fitness function based on

normalization should be used. The normalization calculation is as follows (Huo et al., 2015),

$$f'_m(\chi_n) = \begin{cases} \dfrac{\max(f_m) - f_m(\chi_n)}{\max(f_m) - \min(f_m)}, & if\ \max(f_m) \neq \min(f_m) \\ 1, & if\ \max(f_m) = \min(f_m) \end{cases} \quad (16)$$

The $\boldsymbol{fit(\chi_n)}$ is calculated as following equation (Huo et al., 2015)

$$fit(\chi_n) = \frac{1}{\Pi}\sum_{m=1}^{\Pi} f'_m(\chi_n) \quad (17)$$

The selection probability is calculated as follows,

$$prob_n = \frac{0.9 fit(\chi_n)}{\max_{n=1}^{NS} fit(\chi_n)} + 0.1 \quad (18)$$

Then, each of the onlooker bees searches the new food source depending on the selection probability. If randomly generated number in the range of $[\mathbf{0}, \mathbf{1}]$ is greater than $\boldsymbol{prob_n}$, the new solution will be produced using (14) and the steps in the employed bee phase are applied.

4) Scout Bee Phase

In this phase, if a solution is not improved when the abandonment limit is reached, the existing solution is changed. For this purpose, the existing employed bee is transformed to the scout bee and a new food source is generated by (10). Thus, the algorithm continues to run until the maximum cycle number (MCN) or it reaches a predefined stop criteria.

4. IMPLEMENTATION OF TO-ABC ALGORITHM

The TO-ABC method for MRA design consists of 3 main parts as seen in Fig. 3. The objective functions of the algorithm are defined as given in (1).

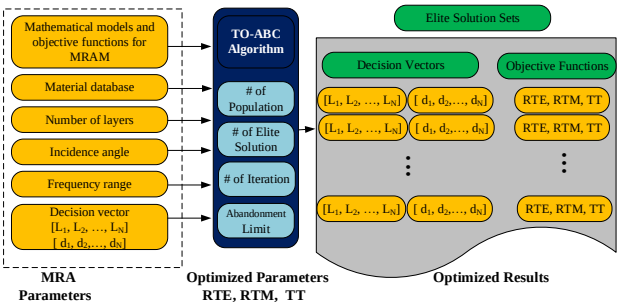

Figure 3. Implementation of TO-ABC to design of MRA

The parameters of the MRA structure and TO-ABC algorithm are defined as given in Fig. 3. Since the minimum layer thicknesses are defined as 0, at the end of the optimization the layers with zero thicknesses are removed from the sequence. Thus, the ES are listed as shown in the Fig. 3 and optimized results are obtained.

4.1. Graphical User Interface for MRA Design

Dozens of studies have been done for the MRA design in the last quarter century. Each of these studies aimed to develop a part of the design problem. In this study, a fully optimized MRA design method is presented for the first time. However, since there are many parameters to consider in MRA design, an easily accessible interface is needed for real applications. Therefore, in this study, a GUI is developed for a fully optimized MRA design. As seen in Fig. 4 the GUI has 5 different parametric inputs such as Frequency, Angle of Incidence, MRA, Optimization and Material List. After these inputs have been defined, the program is run by clicking the "*Start MRA Design*" button. Once the optimization is completed, the optimal results determined on the Pareto front are illustrated in the GUI, while the corresponding RTE, RTM and TT values are listed in the "Elite Solution" section. In GUI, the operator selects the desired result according to the trade-off between RTE, RTM and TT. The NSL and thicknesses of layers corresponding to the selection of the operator are given in the "Layer sequence & Thickness" section and the reflection coefficients for TE and TM polarizations are plotted depending on the angle of incidence. Thus, with the developed GUI, MRA designers can easily access the results they need.

4.2. Fair Comparison Criterias and Comparison Data

Several studies have been conducted for MRA design so far and the superiority of the proposed methods in each study have been compared with previous ones. In order to make a fair comparison, the designed MRAs should be compared based on the same parameters. These parameters can be summarized as follows.

1. When comparing the two designs, it is not fair to consider only the maximum reflection coefficients and to ignore thicknesses. Because it is obvious in MRA design that maximum reflection coefficient decreases with increasing thickness.
2. It is also not true to compare broad-band wide-angle designs for a single type of polarization. For example, while the maximum reflection coefficient for TE polarization is minimized, TM increases. Therefore, the reflection coefficients for TE and TM polarizations need to be optimized simultaneously.
3. When making comparisons, optimizing both designs for the same angle of incidence is another important consideration. For example, it is a not fair comparison to compare an MRA structure which is optimized between 0^0 and 40^0 with another design which is optimized between 0^0 and 60^0. Because, it is an expected result that the MRA optimized for 60^0 has worse RTE, RTM and TT values than the MRA optimized for 40^0.
4. Finally, when presenting the performances of the designs, it is not a consistent method to give the average values of the reflection coefficients relative to the all frequency band and angle of incidence. Because, if the design has a very low reflection coefficient at any angle or frequency, it significantly reduces the average value and affects the general information about other values.

Therefore, these issues should be taken into consideration in order to make a rational assessment. For example, the designs optimized between $0\text{-}40^0$ in (Toktas et al., 2019) were compared to those given in

references(Ranjan et al., 2018; Roy et al., 2015). However, since the designs given in (Roy et al., 2015) were optimized only for normal incidence, their performances at 40^0 are inherently worse than the (Toktas et al., 2019). It is also unfair to compare the designs in (Toktas et al., 2019) with the designs in (Ranjan et al., 2018) , as the MRAs in (Ranjan et al., 2018) were optimized to operate between 0^0 and 60^0.

Based on these 4 criteria, in this study, the designs optimized with 16 virtual materials are compared to those in (Ranjan et al., 2018). Since the formulation (2)&(3) was verified with computer simulation technology (CST) in the previous study(Yigit and Duysak, 2019a), the CST results are not given in this study.

4.3. Designed Fully Optimized MRAs with 16 Virtual Materials

To show the success and practice usage of the TO-ABC, virtual materials listed in (Michielssen et al., 1993) are selected as the material list in the GUI. Three types of MRAs effective in the frequency ranges of 2-8 (Des1), 12-18 (Des2) and 2-18 GHz (Des3) are optimized. The angles of incidence are changed between 0^0 and 60^0. These are compared with those in(Ranjan et al., 2018). All design parameters except the frequency band are selected as shown in Fig. 4. While plotting the reflection coefficients, to obtain high-resolution graphics, the resolutions of frequency and angle are determined as 0.1 GHz and 1^0, respectively. As seen in Table 1, at the end of the TO-ABC algorithm, different MRA structures having different NL and sequences are optimized. As shown in Fig. 4, although the number of ES are identified as 50, a total of 19 possible solutions are found and 7 of them are given in Table 1. It should be noted that the RTE and RTM values given in all Tables are the maximum values between all angles of incidence ($\boldsymbol{\theta} \in [\mathbf{0}°, \mathbf{60}°]$) and frequencies. The 3D plots of RTE and RTM according to angle of incidence and the frequency are illustrated in Fig. 4. When these solutions are compared with the results given in the (Ranjan et al., 2018), it is seen that the highlighted solution 12 in Table 1 is similar to the design in the (Ranjan et al., 2018).

However, although there is a difference of 0.02 dB in RTE, RTM and TT values are lower than those found in [13]. When the other values in Table 1 are examined, it is seen that there are much thinner designs with much lower RTM values than the solution 12. However, it should be noted that RTE values of the other solutions are higher than solution 12.When the solution 13 of Des2 is compared with the respective MRA(Ranjan et al., 2018) in Table 2, it can be seen that both TT, RTE and RTM of the MRA are lower than the(Ranjan et al., 2018). This result clearly demonstrates the success of the proposed method. Furthermore, due to the nature of the MO approach, lower reflection coefficients can be obtained by sacrificing thickness or much finer MRAs can be chosen from Table 2 by compromising from reflection coefficient. Considering Table 3, where the results of Des3 are listed, it can be seen that all the ES consist of 4 layers and most of them have same sequence except from third layer. Furthermore, when the solution 16 in Table 3 is compared with (Ranjan et al., 2018), it is seen that although they have the same sequence, both the RTE, RTM and TT values of the solution 16 are much better than the (Ranjan et al., 2018). This result is a clear indication of the necessity of the triple objective approach in MRA design.

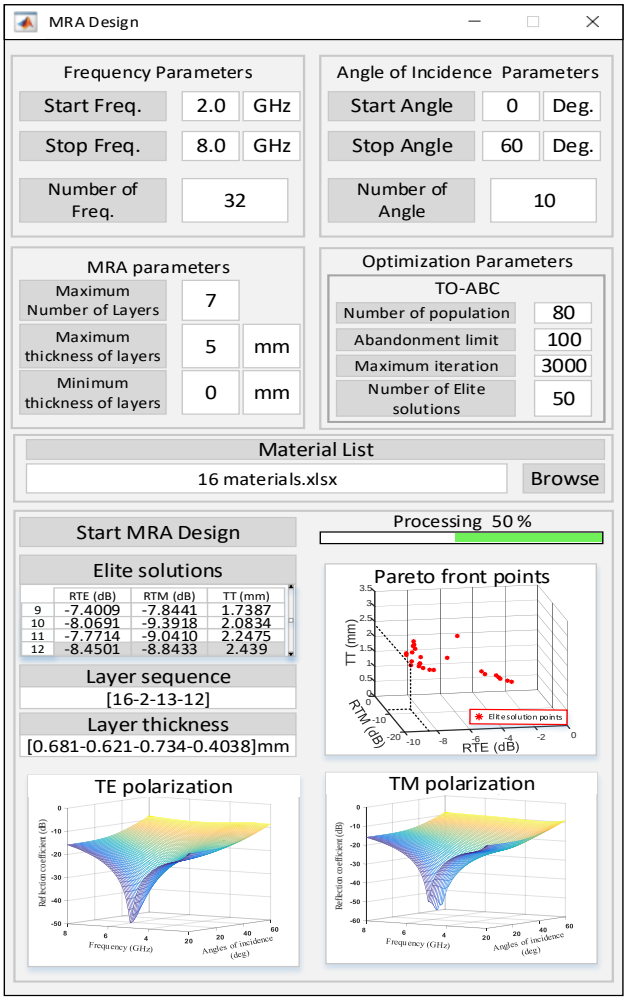

Figure 4. The GUI for fully optimized MRA design

Table 1. The results corresponding to some of the pareto points obtained by TO-ABC algorithm for Des1 (2-8 ghz)

	Layer sequence	d1	d2	d3	d4	RTE	RTM	TT
6	[16-1-9]	0.569	0.332	0.838		-7.401	-7.844	1.739
7	[16-2-10-11]	0.572	0.302	0.415	0.560	-7.554	-9.541	1.849
8	[16-2-10-9]	0.650	0.300	0.373	0.581	-7.768	-9.045	1.903
9	[16-11-2-15]	0.486	0.345	0.877	0.300	-8.056	-7.834	2.008
10	[16-2-9-11]	0.656	0.447	0.417	0.563	-8.069	-9.392	2.083
11	[14-2-13]	0.629	1.006	0.612		-7.771	-9.041	2.248
12	[16-2-13-12]	0.681	0.621	0.734	0.404	-8.450	-8.843	2.440
			Data from (Ranjan et al., 2018)					
	Layer sequence	d1	d2	d3	d4	RTE	RTM	TT
	[16-2-13-12]	0.701	0.657	0.707	0.383	-8.476	-8.570	2.449

Table 2. The results corresponding to some of the pareto points obtained by TO-ABC algorithm for Des2 (8-12 GHz)

	Layer sequence	d1	d2	d3	d4	RTE	RTM	TT
8	[16-2]	0.364	0.286			-6.668	-12.685	0.650
9	[16-8]	0.376	0.370			-7.050	-12.879	0.746
10	[16-2-5-6]	0.376	0.276	0.040	0.124	-7.742	-9.050	0.817
11	[16-8-6]	0.376	0.308	0.250		-7.776	-10.878	0.935
12	[16-8-16]	0.259	0.651	0.136		-8.021	-11.531	1.046
13	[16-8-12-6]	0.376	0.560	0.014	0.162	-8.543	-10.484	1.113
14	[16-8-6]	0.373	0.634	0.250		-9.302	-9.622	1.256
	Data from (Ranjan et al., 2018)							
	Layer sequence	d1	d2	d3	d4	RTE	RTM	TT
	[16-7-3-8]	0.358	0.414	0.130	0.293	-8.510	-9.940	1.195

Table 3. The results corresponding to some of the pareto points obtained by TO-ABC algorithm for Des3 (2-18 GHz)

	Layer sequence	d1	d2	d3	d4	RTE	RTM	TT
12	[16-7-3-14]	0.340	1.227	0.379	0.501	-6.714	-7.277	2.447
13	[16-7-3-14]	0.340	1.036	0.731	0.385	-6.768	-7.854	2.492
14	[16-7-3-14]	0.340	1.183	0.631	0.425	-6.899	-7.782	2.579
15	[16-7-4-14]	0.340	1.300	0.568	0.445	-6.972	-8.448	2.653
16	[16-7-5-14]	0.349	1.245	1.000	0.319	-7.444	-8.466	2.912
17	[16-6-3-14]	0.340	1.232	1.063	0.367	-7.333	-8.183	3.002
18	[16-7-3-15]	0.340	1.264	1.094	0.367	-7.150	-8.658	3.065
	Data from (Ranjan et al., 2018)							
	Layer sequence	d1	d2	d3	d4	RTE	RTM	TT
	[16-7-5-14]	0.348	1.246	1.002	0.326	-7.400	-8.300	2.920

4.4. Designed MRAS with Real Materials

After the importance of TO-ABC approach in the fully optimized MRA design has been proved by the use of predefined virtual materials, real MRA structures have been designed with much more limited real materials. For this purpose, a new material pool of 21 fabricated materials presented in the literature(Yigit and Duysak, 2019a) are used. The compositions of the materials and measured operating frequencies are given in Table 4. The frequency dependent complex permeabilities $\boldsymbol{\mu_i}$ and permittivities $\boldsymbol{\varepsilon_i}$ of these 21 up-to-date materials can be downloaded from (Yigit and Duysak, 2019a, 2019b). 4 types of MRA structures labeled as Des4 (2-8 GHz), Des5 (8.2-12.4GHz), Des6 (12-18GHz) and Des7 (2-18 GHz) are optimized at wide-angle (0^0-60^0). The layer properties and labels of the selected designs are listed in Table 5. In GUI software, the control parameters of the optimization process such as maximum number of layers, abandonment limit, maximum iteration number, population number and maximum number of elite solution are selected as 10, 100, 3000, 100 and 100, respectively. The maximum and minimum layer thicknesses are defined as 4 mm and 0 mm, respectively. Thus, at the end of the optimization, the layers having a thickness of 0 mm is removed from the structure. In these designs, since the used real materials are limited, TT is ignored when choosing between the ES and the solutions with minimum reflection coefficient are presented. Des4, Des5, Des6 and Des7 are selected by considering both RTE and RTM values. While some designs have lower RTM values, these designs have higher RTE values than other designs.

Although the reflection coefficients of the designed MRAs can be simply obtained by using (2, 3), for an easier assessment, RTE and RTM corresponding to the each 10^0 angle of incidences are presented in Table 5. As seen in Table 6, 7, 8 and 9, 7 design are given in each table. As shown in Table 6, the RTE and RTM of solution 33 of Des5 are -6.29 and -11.79 dB for whole angles of incidence and the frequencies. In the initial parameters of the TO-ABC algorithm, this value can be selected larger, so that thicker, but better MRA structures can be designed. Since the all materials given in Table 4 can be used in Des5, much more successful MRA structures are designed than the Des4. As shown in Table 7, the TT of solution 20 is 4.058 mm, although it has an absorption capability of 87% for all frequencies and all angles of incident between 0^0-60^0. When the solution 24 given in Table 7 is observed, it is realized that the TT increases but the maximum reflection coefficients considerably decreases. In Des6, 8 materials given in the Table 4 are used. The ES obtained after TO-ABC are given in Table 8. Although all solutions have the same layer sequence, they have different thickness and reflection coefficient values. Among these solutions, the solution 15 with the lowest RTE value is selected and the RTE and RTM values are seen in Table 5.

Table 4. Up-to-date materials listed in literature (Yigit and Duysak, 2019a, 2019b)

Material number	Fabricated Materials	Measured Frequency range (GHz)
17	Dispersed Alinco ($Fe_{49.7}Co_{24}Ni_{14}Al_8Cu_3Nb_1Ti_{0.3}$) powder in paraffin wax. Fraction of powder is 50%	2-18
18	Dispersed Alinco powder in paraffin wax. Fraction of powder is 60%	2-18
19	$Ba_{0.85}Sm_{0.15}Co_2Fe_{16}O_{27}$ hexaferrite	2-18
20	Pure porous carbon, obtained through the pyrolysis of pure ZIF-67	2-18
21	The Ferrit/Co/porous carbon materials obtained through the pyrolysis of $Ba_{0.85}Sm_{0.15}Co_2Fe_{16}O_{27}$ @ZIF-67 template at 500^0C	2-18
22	… $Ba_{0.85}Sm_{0.15}Co_2Fe_{16}O_{27}$ @ZIF-67 template at 550^0C	2-18
23	…$Ba_{0.85}Sm_{0.15}Co_2Fe_{16}O_{27}$ @ZIF-67 template at 650^0C	2-18
24	Carbon coated nickel nanocapsule	2-18
25	U-type hexaferrite $Ba_4(Co_{1-3x}Cr_x)_2Fe_{36}O_{60}$) for different values of *x*	8.2 - 12.4
26	U-type hexaferrite $Ba_4(Co_{1-3x}Cr_x)_2Fe_{36}O_{60}$) for different values of *x*	8.2 - 12.4
27	U-type hexaferrite $Ba_4(Co_{1-3x}Cr_x)_2Fe_{36}O_{60}$) for different values of *x*	8.2 - 12.4
28	U-type hexaferrite $Ba_4(Co_{1-3x}Cr_x)_2Fe_{36}O_{60}$) for different values of *x*	8.2 - 12.4
Polyaniline (PA)/expanded graphite (EG) composites mixed at different weight percentages (*wt. %)* with novolac phenolic resin (NPR) (PA/EG_x – NPR)		
29	*x*=0.15, 10 wt.%	
30	*x*=0.15, 20 wt.%	
31	x=0.15, 30 wt.%	
32	x=0.25, 10 wt.%	
33	x=0.25, 20 wt.%	8.2 - 12.4
34	x=0.25, 30 wt.%	
35	x=0.00, 10 wt.%	
36	x=0.00, 20 wt.%	
37	x=0.00, 30 wt.%	

Table 5. The layer properties and reflection coefficients of Des4, Des5, Des6 and Des7

L.#	Des4 2-8 GHz 0^0-60^0 TE/TM pol.			Des5 8.2-12.4 GHz 0^0-60^0 TE/TM		
	Mat. #	Thick. (mm)		Mat #	Thick. (mm)	
1	19	3.975		17	0.095	
2	20	1.072		36	2.551	
3	24	1.954		37	0.894	
4	18	1.144		17	0.517	
Maximum Reflection Coefficient (dB)	Angle of incidence			Angle of incidence		
	0^0	-12.05 TE	-12.05 TM	0^0	-11.96 TE	-11.96 TM
	10^0	-12.02 TE	-12.23 TM	10^0	-12.01 TE	-12.16 TE
	20^0	-11.82 TE	-12.76 TM	20^0	-12.11 TE	-12.74 TE
	30^0	-11.22 TE	-13.72 TM	30^0	-12.19 TE	-13.62 TE
	40^0	-9.96 TE	-15.16 TM	40^0	-12.05 TE	-14.42 TE
	50^0	-8.26 TE	-16.30 TM	50^0	-11.24 TE	-14.11 TE
	60^0	-6.29 TE	-11.79 TM	60^0	-8.81 TE	-11.40 TE
TT		8.14 (mm)			4.05 (mm)	
NL		4			4	

L.#	Des6 12-18 GHz 0^0-60^0 TE/TM pol.			Des7 2-18 GHz 0^0-60^0 TE/TM pol		
	Mat. #	Thick. (mm)		Mat #	Thick. (mm)	
1	19	1.851		19	2.980	
2	20	0.803		21	1.384	
3	17	0.298		22	0.881	
4	22	0.291		18	0.811	
Maximum Reflection Coefficient (dB)	Angle of incidence			Angle of incidence		
	0^0	-9.99 TE	-9.99 TM	0^0	-8.33TE	-8.33 TM
	10^0	-9.97 TE	-10.16 TM	10^0	-8.26TE	-8.48 TM
	20^0	-9.89 TE	-10.70 TM	20^0	-8.05TE	-8.97 TM
	30^0	-9.70 TE	-11.71 TM	30^0	-7.68TE	-9.89 TM
	40^0	-9.27 TE	-13.35 TM	40^0	-7.11TE	-11.47 TM
	50^0	-8.44 TE	-15.59 TM	50^0	-6.28TE	-11.16 TM
	60^0	-7.04 TE	-15.42 TM	60^0	-5.02TE	-9.45 TM
TT		3.24 (mm)			6.056 (mm)	
NL		4			4	

Table 6. The results selected from 50 pareto points obtained by TO-ABC algorithm for Des4 (2-8 GHz)

	Layer sequence	d1	d2	d3	d4	RTE	RTM	TT
28	[19-21-20-18]	3.535	0.780	0.299	1.232	-5.051	-10.600	5.845
29	[19-21-20-18]	3.118	1.481	0.458	1.082	-4.928	-10.794	6.138
30	[19-21-20-18]	4.000	0.770	0.012	1.422	-5.171	-11.162	6.204
31	[19-20-18]	4.000	1.082	1.461		-5.238	-11.749	6.543
32	[19-20-18]	4.000	1.159	1.422		-5.268	-11.827	6.581
33	[19-20-24-18]	3.975	1.072	1.954	1.144	-6.290	-11.790	8.140
34	[19-24-17]	4.000	3.802	1.508		-6.048	-12.813	9.310

Table 7. The results selected from 38 pareto points obtained by TO-ABC algorithm for Des5 (8.2-12.4 GHz)

	Layer sequence	d1	d2	d3	d4	RTE	RTM	TT
18	[25-29-30-25]	0.684	0.828	0.074	0.757	-6.466	-12.809	2.343
19	[18-35-26-18]	0.095	2.542	0.478	0.396	-6.884	-14.660	3.512
20	[17-36-37-17]	0.095	2.551	0.894	0.517	-8.812	-11.405	4.058
21	[36-36-17-24]	3.358	0.862	0.655	0.380	-8.040	-14.950	5.254
22	[32-34-20-23]	3.336	0.443	1.195	0.538	-7.398	-15.295	5.513
23	[29-23-34]	4.000	0.622	1.731		-7.802	-16.404	6.353
24	[30-29-26-27]	1.442	3.026	2.032	2.628	-9.413	-12.639	9.129

Table 8. The results selected from 40 pareto points obtained by TO-ABC algorithm for Des6 (12-18 GHz)

	Layer sequence	d1	d2	d3	d4	RTE	RTM	TT
9	[19-20-17-22]	1.061	1.006	0.297	0.185	-5.379	-12.993	2.549
10	[19-20-17-22]	1.279	0.837	0.243	0.289	-5.547	-13.839	2.648
11	[19-20-17-22]	1.362	0.791	0.250	0.312	-5.743	-14.561	2.715
12	[19-20-17-22]	1.486	0.761	0.298	0.283	-5.793	-14.516	2.827
13	[19-20-17-22]	1.461	0.801	0.298	0.291	-5.846	-14.192	2.851
14	[19-20-17-22]	1.560	0.814	0.298	0.291	-6.199	-12.922	2.963
15	[19-20-17-22]	1.851	0.803	0.298	0.291	-7.036	-9.994	3.243

Table 9. The results selected from 19 pareto points obtained by TO-ABC algorithm for Des7 (2-18 GHz)

	Layer sequence	d1	d2	d3	d4	RTE	RTM	TT
11	[19-24-21-18]	2.894	0.093	1.925	0.837	-4.960	-8.763	5.749
12	[19-21-22-18]	2.781	1.387	0.742	0.866	-4.811	-9.647	5.775
13	[19-24-21-18]	2.894	0.232	1.866	0.849	-4.897	-8.960	5.842
14	[19-24-21-18]	2.894	0.353	1.783	0.897	-4.872	-9.152	5.928
15	[19-21-22-18]	2.980	1.384	0.881	0.811	-5.026	-8.330	6.056
16	[19-21-22-18]	2.885	1.598	0.898	0.771	-5.000	-9.247	6.153
17	[19-24-20-18]	2.796	1.334	1.526	1.098	-4.911	-9.158	6.754

As listed in the Table 5, both RTE and RTM of Des7 are below -7 dB for the all angles of incidence between 0^0-40^0. Although the all designs in this section are optimized using limited number materials, the obtained satisfactory results clearly demonstrate the superiority of the TO-ABC method.

As shown in Table 5, reflection coefficients of the Des6 is below -9.27 dB for entire frequency band and angles of incident between 0^0- 40^0. Since the Des7 is optimized to operate at broad-band (2-18 GHz), as shown in Table 9, the maximum reflection coefficient is found about -5 dB for whole angles of incidence.

4. CONCLUSION

In the last 25 years, optimization based many studies have been carried out for MRA design. While the majority of these studies were performed with single-objective optimization, some of them were performed with double-objective approaches. However, in order to fully optimize an MRA structure, RTE, RTM and TT must be simultaneously optimized. Thanks to the proposed TO-ABC algorithm, RTE, RTM and TT are simultaneously optimized for the first time and the ES of the objective functions are successfully obtained. Three MRA structures designed with virtual materials are compared with the latest MRAs in the literature and the performance of the proposed method is demonstrated. In addition, thanks to the developed GUI, a practical and easy user interface for MRA design is also provided.

Furthermore, four different broad-band wide-angle MRAs operating in the frequency ranges of 2-18 GHz are designed using 21 real-materials presented in recent years. Thanks to developed TO-ABC algorithm, despite the limited number of materials, all possible solutions providing the specified parameters are achieved and successful MRA structures are designed. With the help of proposed GUI, MRA designs can be practically realized without the need for complex computer scripts. Since the results obtained in this study provide a new perspective

for MRA design, triple-objective approach can be developed for different optimization techniques in further studies.

REFERENCES

Asi M & Dib N I (2010). Design of multilayer microwave broadband absorbers using central force optimization. Progress in Electromagnetic Research, 26, 101–113.

Deb K, Pratap A, Agarwal S & Meyarivan T (2002). A fast and elitist multiobjective genetic algorithm: NSGA-II. IEEE Trans. Evol. Comput. 6, 182–197. https://doi.org/10.1109/4235.996017

Goudos S K (2009). Design of microwave broadband absorbers using a self-adaptive differential evolution algorithm. International Journal of RF and Microwave Computer-Aided Engineering, 19(3), 364–372.

Goudos S K & Sahalos J N (2006a). Design of Broadband Radar Absorbing Materials using Particle Swarm Optimization, Proceedings of EMC Europe, 1111–1116.

Goudos S K & Sahalos J N (2006b). Microwave absorber optimal design using multi-objective particle swarm optimization. Microwave and Optical Technology Letters, 48, 1553–1558.

Huo Y, Zhuang Y, Gu J & Ni S (2015). Elite-guided multi-objective artificial bee colony algorithm. Applied Soft Computing 32, 199–210. https://doi.org/https://doi.org/10.1016/j.asoc.2015.03.040

Jiang L, Cui J, Shi L & Li X (2009). Pareto optimal design of multilayer microwave absorbers for wide-angle incidence using genetic algorithms. IET microwaves, antennas & Propagation, 3(4), 572–579.

Karaboga D & Basturk B (2007). A powerful and efficient algorithm for numerical function optimization: artificial bee colony (ABC) algorithm. Journal of Global Optimization, 39(3), 459–471.

Kern D J & Werner D H (2003). A genetic algorithm approach to the design of ultra-thin electromagnetic bandgap absorbers. Microwave and Optical Technology Letters, 38, 61–64. https://doi.org/10.1002/mop.10971

Michielssen E, Sajer J-M, Ranjithan S & Mittra R (1993). Design of lightweight, broad-band microwave absorbers using genetic algorithms. IEEE Transactions on Microwave Theory and Technology, 41(6), 1024–1031.

Ranjan P, Choubey A & Mahto S K (2018). A novel approach for optimal design of multilayer wideband microwave absorber using wind driven optimization technique. AEU-International Journal of Electronics and Communications, 83, 81–87.

Roy S, Mahanti A, Roy S D & Mahanti G K (2016). Comparison of Evolutionary Algorithms for Optimal Design of Broadband Multilayer Microwave Absorber for Normal and Oblique Incidence. Applied Computational Electromagnics Society Journal, 31(1).

Roy S, Roy S D, Tewary J, Mahanti A & Mahanti G K (2015). Particle swarm optimization for optimal design of broadband multilayer microwave absorber for wide angle of incidence. Progress in Electromagnics Research, 62, 121–135.

Toktas A, Ustun D & Tekbas M (2019). Multi-Objective Design of Multi-Layer Radar Absorber Using Surrogate-Based Optimization. IEEE Transations on Microwave Theory and Technology, 67, 3318–3329. https://doi.org/10.1109/TMTT.2019.2922600

Toktas A, Ustun D, Yigit E, Sabanci K & Tekbas M (2018). Optimally Synthesizing Multilayer Radar Absorbing Material (RAM) Using Artificial Bee Colony Algorithm. Proceedings of International Seminar/Workshop on Direct and Inverse Problems of Electromagnetic and Acoustic Wave Theory, DIPED. IEEE, 237–241. https://doi.org/10.1109/DIPED.2018.8543261

Weile D S, Michielssen E & Goldberg D E (1996). Genetic algorithm design of Pareto optimal broadband microwave absorbers. IEEE Transactions on Electromagnetic Compatibility, 38(3), 518–525.

Yigit E & Duysak H (2019)a. Determination of Optimal Layer Sequence and Thickness for Broadband Multilayer Absorber Design Using Double-Stage Artificial Bee Colony Algorithm. IEEE Transactions on Microwave Theory and Techniques, 67(8), 3306–3317.

Yigit E & Duysak H (2019)b. electrical_properties.xlsx. IEEE Transactions on Microwave Theory and Technology https://ieeexplore.ieee.org/abstract/document/8744403/media#media

International Journal of Engineering and Geosciences

https://dergipark.org.tr/en/pub/ijeg

e-ISSN 2548-0960

A new approach for matching road lines using efficiency rates of similarity measures

Müslüm Hacar*[1], Turkay Gökgöz[1]

[1]*Yıldız Technical University, Engineering Faculty, Geomatics Engineering Department, Istanbul, Turkey*

Keywords
Object matching
Similarity measure
Efficiency ratio
Geometric integration
Map conflation

ABSTRACT

The lack of common semantic information among corresponding geo-objects in different datasets required new matching approaches based on geometric and topological measures. In this study, a semi-automated matching approach based on the matching capabilities of geometric and topological measures was proposed. In the first stage, after the initial matching performed by a scoring system, the efficiency of each measure on the matching accuracy is evaluated manually by an operator. In the second stage, (1) the score of each measure is updated in accordance with the accuracy distributions. This means that the score of a measure is increased if it is relatively more significant than others. Finally, (2) matching process is repeated with new scores. The proposed approach was tested by matching tree-, cellular-, and hybrid-patterned road lines in municipal, private navigation, and OpenStreetMap datasets. The experimental testing shows that it has satisfactory results both in accuracy and completeness. F-measure is over 86% in hybrid-patterned Bosphorus datasets.

1. INTRODUCTION

Geometric integration establishes the relationships between the objects in a spatial dataset and the corresponding objects in another dataset and ensures that the target dataset reaches the required competence. Producing better (geometrically and semantically more up-to-date and rich) maps by using two different maps representing the same entities is also an important issue of integration and is called map conflation (Lynch and Saalfeld, 1985; Saalfeld, 1988). The integration process can be used for different purposes. Cobb et al. (1998) remarked the requirements for map conflation as; updating with the objects transferred from one dataset to another, optimization of geometric and semantic accuracy, and transferring data to a dataset containing missing information. The conflation process enables the spatial data generated by different sources to be used together. Geometric, topological and semantic similarities between objects are important criteria for the conflation process. The greater the similarity, the lower the operator effort.

The conflation process is based on the principle of matching geometries (point, line, and polygon) that represent the same real entities (Yuan and Tao, 1999). Determining the correspondences between the objects according to their relations and similarities is called matching process (Hacar and Gökgöz, 2019b).

In this study, a semi-automated matching approach based on the efficiency rates of the measures was proposed. In this section, related studies in the literature are examined. Following section presents the study area and datasets, the geometric and topological measures used to determine the similarities between the objects, and the proposed approach. Section 3 presents the experiment with tree-, cellular-, and hybrid-patterned road networks, and the evaluation of the results conducted with the statistics of the study. Section 4 concludes the study by discussing the results and giving several further suggestions.

1.1. Related Works

Many methods have been developed to match line objects since it was first applied in 1980s by Rosen and Saalfeld (1985) and Saalfeld (1988). Main problem in line matching is that none of the corresponding line geometries from different sources are geometrically identical. In other words, the geometrical properties of corresponding line objects such as orientation, length, shape, location have not equal values. According to Hacar and Gökgöz (2019b), there are three important reasons that researchers prefer to work with line matching rather than point and polygon matchings: (1) difficulties in establishing relationships between complex representations such as patterns, intersections,

* **Corresponding Author**

*(muslumhacar@gmail.com)ORCID ID 0000-0002-8737-8262
(gokgoz@yildiz.edu.tr) ORCID ID 0000-0001-8716-6131

Cite this article

Hacar M & Gökgöz T (2021). A new approach for matching road lines using efficiency rates of similarity measures. International Journal of Engineering and Geosciences, 6(3), 146-156

Research Article / DOI: 10.26833/ijeg.791324 **Received: 07/09/2020; Accepted: 04/11/2020**

roundabouts, dead ends, (2) the need to keep navigation datasets up-to-date and (3) the rise of Volunteered Geographical Information (VGI) datasets.

The concepts of matching progress in spatial data integration have also been focused by researchers. Yuan and Tao (1999) classified the matching process by geometry, topology and semantic. Ruiz et al. (2011) also discussed the integration process by match type; geometric, topological and semantic. Volz (2006) classified the process by similarity measures; point-, linear-, and area-based and the hybrid. Xavier et al. (2016) classified the measures as geometric, topological, attribute, context, and semantic. Memduhoğlu and Başaraner (2018) compared thematic geographic ontologies created for cities and discussed about possible contributions of basic integration methods and technologies of spatial semantics for creating a multi-representation spatial database paradigm. Hacar and Gökgöz (2019a) designed a conceptual model for matching process under spatial data integration by classifying the types of geometry, measure, relationship, and spatial information.

There have been developed many matching methods. While some of them works fully automated, others allow the user intervention. Xiong and Sperling (2004) proposed a semi-automatic method for matching road networks. By using a cluster-based matching process, strong relationships between nodes, edges, and segments in the two road networks are determined. Their method allows identifying and correcting missing matches, but requires significant interaction (operator intervention) during the process. Li and Goodchild (2011) proposed an automated optimization model to match the road lines using geometric and semantic measures, as well as an affine transformation. They used asymmetric property of one-way Hausdorff distance as a measure of dissimilarity. In addition, the Hamming distance was also used as a criterion of dissimilarity to show the difference between road names. Lei and Lei (2019) also developed a flow-based optimization model that seeks to minimize the total discrepancy between two datasets. Moreover, Araújo et al. (2019) proposed a Spark-based approach using the names of the places (semantic) and context information (e.g., neighbouring streets) to compare the corresponding objects in real-world data sources of New York and Curitiba.

Some researchers focused on matching objects in datasets that have a significant scale difference. To work with this kind of source datasets, researchers often use topological measures (e.g., the degree of connectivity (or the valence), spider function, buffer-growing, etc.) to match the corresponding objects. Mustière and Devogele (2008) proposed an approach relying on the comparison of geometrical, attributive, and topological properties of objects for matching networks with different levels of details. Olteanu-Raimond et al. (2015) used belief theory to represent and fuse knowledge from different sources to model imperfection (imprecision, uncertainty, and incompleteness), and make a decision. Chehreghan and Abbaspour (2018) developed an optimization-based matching approach for multi-source spatial datasets by taking into account several geometric criteria. The approach benefits from a genetic algorithm and sensitivity analysis to identify corresponding objects. Moreover, Guo et al. (2019) designed a new matching method for the objects in multi-scale geodatabases using weights of some well-known geometric and topological measures. The method has three stages; (1) entire, (2) partial matchings, and (3) roundabout detection and matching. The authors used a splitting process to match the unmatched road segments.

Some studies in urban lands are also crucial tasks of integration cases. Recently, VGI, social media, and geocoding data are used to extract and combine new spatial data in urban areas (Hacar 2020; Kılıç and Gülgen 2020; Bilgi et al. 2019). VGI enables generation of maps by using crowd-sourced volunteer contributors. Each volunteer has equal role to contribute the geometric and semantic properties of the geographical objects. However, since there is no rule to be a volunteer in VGI, non-expert contributors may draw features irregularly or inconsistently with basics of cartography. Therefore, result map may have low quality. In this context, geo-object matching is used as a process providing a solution for analysing and increasing the quality and accuracy of VGI data. Koukoletsos et al. (2012) proposed a matching approach to assess the completeness of VGI data. They developed a multi-step approach matching OpenStreetMap (OSM) road data with the UK's official mapping agency Ordnance Survey (OS), taking into account the similarities in geometric (search distance, direction, line-based buffer zone) and attribute (road names). Pourabdollah et al. (2013) also conducted a conflation study with attribute-rich OS data to improve the quality of OSM road data. Besides, Hacar and Gökgöz (2019b) conducted a matching study with OSM and TomTom navigation data. In some cases, line-based (linear) approaches to matching road objects may be insufficient. In such cases, an area-based (spatial) matching approach, like proposed by Fan et al. (2016), can be used. This method finds the corresponding blocks in source datasets with a spatial overlapping ratio. It then matches the surrounding roads using the matched blocks. Also Fan et al. (2016) tested their method by matching OSM and public city data and achieved satisfactory results in Heidelberg (Germany), a network of regular networks, and Shanghai (China), with a relatively more complex network. The sources and patterns of road networks are two important factors to consider in the matching process. Yang et al. (2014) classify the pattern groups of the blocks that the roads surround and match the nodes in the groups hierarchically. Hacar (2019) and Hacar and Gökgöz (2019b) developed a score-based multi-stage method and tested it with cellular-, tree-, and hybrid- patterned road networks. According to the method, the candidate matches are scored in accordance with the geometric and topological similarity and then the objects with high scores are matched incrementally.

The matching methods differ from each other according to the hierarchical steps of the approaches, even if they have some common stages, metrics or rules. The design of the method can primarily affect the sufficiency of the case study. Also, the complexity of road networks can reduce the sufficiency. The previous approaches had low interest in complex road networks

such as in Istanbul. In this study, the scope of the proposed approach is determined to design a new matching model and its applicability in Istanbul road networks.

2. THE PROPOSED APPROACH

The proposed approach performs the matching process of road lines thanks to the efficiency rates. The rates are calculated using geometric and topological measures. The main idea for selecting the measures is to determine the similarities of corresponding matching pairs from different source datasets. As seen in Fig. 1, the matching process is managed in two stages in addition to a pre-process. Firstly, two road networks are aligned as a pre-process. In the first stage, road lines closer to each other than a predefined threshold distance value T are identified as candidate matchings. Hausdorff distance is used to determine the closeness between candidates. T should be large enough to identify possible correct matches and small enough not to cause too many missing matches (mismatching). The threshold can be determined by examining the source datasets and structure of road networks, and by conducting several experimental matching observations. After the selection of corresponding pairs, for each candidate matching, (1) similarity scores are calculated based on the measures of Hausdorff distance (S_H), orientation (S_O), sinuosity (S_S), mean perpendicular distances (S_P), mean length of triangular edges (S_T) and modified degree of connectivity (S_C) (Fig. 2). The maximum similarity score assigned to a candidate pair is 4 for all measures apart from sinuosity and mean perpendicular distance. Sinuosity and mean perpendicular distance represent similar characteristics of lines. The maximum score with respect to these indicators is 2 so that the maximum total score of these indicators shall be the same as the others, 4, for fairness (Hacar and Gökgöz, 2019b). Table 1 shows the computation criteria of scores for each measure. (2) Sum of the similarity scores are obtained for each candidate pair, and (3) the candidates, whose total similarity scores are maximum, are selected as matched pairs and other candidates are eliminated. The efficiency of each measure is determined by comparing the matched pairs with the result of the manual matching. After determining the number of correct and incorrect matches for each measure, it is ensured that the score of the measure, which performs better results in term of the number of correct and incorrect matches, is higher than that of the relatively insignificant (less number of correct and/or much more incorrect matches). For this purpose, the efficiency ratio is used, where the numbers of correct and incorrect matchings are placed together. Each measure has its own efficiency ratio.

Maximum-Minimum normalization method was adapted to calculate the efficiency ratio. Briefly, the ratio is multiplied by the similarity scores to increase the effect of the measure that performs the matching process with high accuracy and reduces, but not disables, the effect of the measure with low accuracy.

The normalization consists of two equation: *Profit* (P) and *Loss* (L) (Eq. 1 and Eq. 2). While P represents how far the value X_i from minimum value, L represents how close the value X_i to maximum value. The following formulas are used as original Maximum-Minimum normalization measures (Başaraner, 2011; Şen, 2013).

$$P = \frac{X_i - X_{min}}{X_{max} - X_{min}} \quad (1)$$

$$L = \frac{X_{max} - X_i}{X_{max} - X_{min}} \quad (2)$$

These criteria can be adapted to calculate the normalized values P_i and L_i for each similarity measure with regards to the correct and incorrect match numbers as follows.

$$P_i = \frac{N_{Correct_i} - N_{Correct_{min}}}{N_{Correct_{max}} - N_{Correct_{min}}} \quad (3)$$

$$L_i = \frac{N_{Incorrect_{max}} - N_{Incorrect_i}}{N_{Incorrect_{max}} - N_{Incorrect_{min}}} \quad (4)$$

where $N_{Correct_i}$ (i=1,2,..,n) represents the number of correct matches of the respective measure, $N_{Correct_{min}}$ represents the least number of correct matches, and $N_{Correct_{max}}$ represents the maximum number of correct matches between all the measures. In addition, $N_{Incorrect_i}$ (i=1,2,..,n) represents the number of incorrect matches of the respective measure, $N_{Incorrect_{min}}$ represents the least number of incorrect matches, and $N_{Incorrect_{max}}$ represents the maximum number of incorrect matches between all the measures.

The efficiency rates could be calculated as follows:

$$E_i = P_i \times L_i \quad (5)$$

However, the efficiency ratio (Eq. 5) is to be zero for the measure that performs the maximum number of incorrect or minimum number of correct matches. This results in the score used for the respective measure being multiplied by a factor of 0 (zero) and the corresponding measure being ineffective (disabled) in the second stage of the approach. Since there is no correlation between the numbers of the correct and incorrect matches, making any measure ineffective may reduce the success of the process. Also, our experience in matching cases motivates us to consider all of the measures, even if it is relatively less significant (generating many incorrect matches). Therefore, the exponential function should be used with previous formula (Eq. 5). Exponential function prevents the least important measure from taking a value 0 (Eq. 6). In other words, the least important measure also affects the results in the second stage.

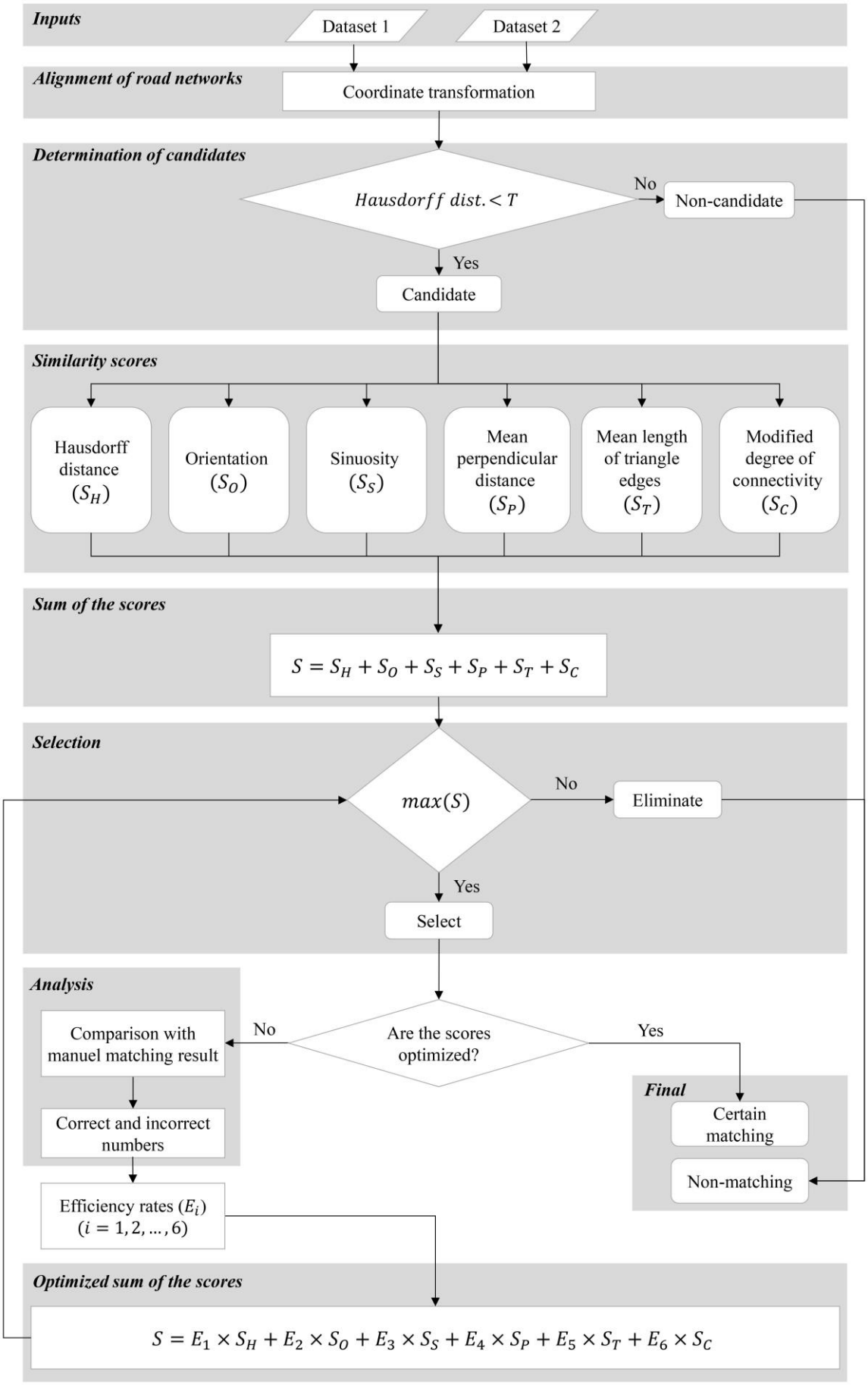

Figure 1. The workflow of the proposed approach

Table 1. The computation criteria of similarity scores (Hacar, (2019); Hacar and Gökgöz, 2019b)

Measure	Criteria
Hausdorff distance	For each candidate pair, the first three closest matches are scored as $S_{H_1} = 4$, $S_{H_2} = 2$, and $S_{H_3} = 1$, respectively. The fourth and others are scored as $S_{H_{i\,(i>3\,\in Z^+)}} = 0$.
Orientation	Candidate pairs in the same class are scored as $S_O = 4$. If they are in adjacent classes (seen in Fig. 2)), the score is assigned as $S_O = 2$. Otherwise, the score is assigned as $S_O = 0$.
Sinuosity	The rules for sinuosity scores (S_S) are as follows: if S_n = Low and if S_m = Low, then $S_S = 2$ if S_n = Low and if S_m = Mid, then $S_S = 1$ if S_n = Low and if S_m = High, then $S_S = 0$ if S_n = Mid and if S_m = Low, then $S_S = 1$ if S_n = Mid and if S_m = Mid, then $S_S = 2$ if S_n = Mid and if S_m = High, then $S_S = 1$ if S_n = High and if S_m = Low, then $S_S = 0$ if S_n = High and if S_m = Mid, then $S_S = 1$ if S_n = High and if S_m = High, then $S_S = 2$
Mean perpendicular distance	If the difference between the mean perpendicular distances of Line n and Line m is less than or equal to $\sigma_p/2$ (σ_p is the standard deviation of all mean perpendicular distances), then it is scored as $S_P = 2$. If the difference between the mean perpendicular distances of Line n and Line m is greater than $\sigma_p/2$ and less than or equal to σ_p, then it is scored as $S_P = 1$. Otherwise, it is scored as $S_P = 0$.
Mean length of triangle edges	If the difference between the mean length of triangle edges of Line n and Line m is less than or equal to $\sigma_E/2$ (σ_E is the standard deviation of all mean lengths of triangle edges), then this matching is scored as $S_T = 4$. If the difference between the mean length of triangle edges of Line n and Line m is greater than $\sigma_E/2$ and less than or equal to σ_E, then it is scored as $S_T = 2$. Otherwise, it is scored as $S_T = 0$.
Modified degree of connectivity	If the candidates have the same degree, then it is scored as $S_C = 4$. If there is a just one degree of difference between the candidates, then it is scored as $S_C = 2$. Otherwise, it is scored as $S_C = 0$.

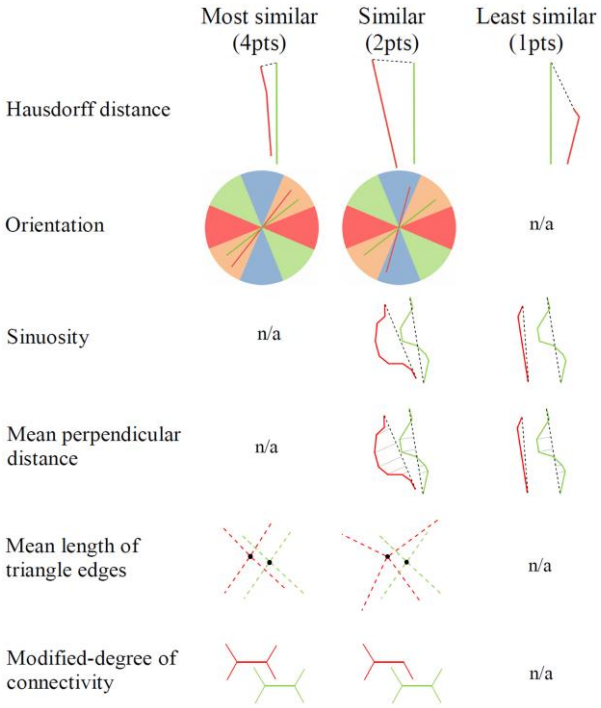

Figure 2. The similarity scores of possible matches (Hacar and Gökgöz, 2019b).

$$E_i = 2^{P_i \times L_i} \quad (6)$$

In the second stage, the matching process is repeated with similarity scores updated (optimized) with E_i efficiency rates. This means that the score of a measure is increased whether it is relatively more significant than others. Finally, the candidates with the highest total similarity scores are determined as certain matches.

3. EXPERIMENTAL TESTING

3.1. Study Area and Datasets

The proposed method was tested with tree-, cellular-, and hybrid-patterned road networks in Istanbul. We used different sources as; Istanbul Metropolitan Municipality (IMM), two private navigation companies Başarsoft and TomTom, and OSM, one of the popular VGI projects, to show how efficient the proposed approach with different samples (Fig. 3) (Table 2). Also, an additional matching process was conducted with a large amount of data covering Bosphorus of Istanbul to prove its efficiency in a realistic way (Fig. 4). In Bosphorus, major elevation differences exist from coastal land to exterior bound. This kind of local surface changes makes road networks complex and leads the road shapes to be similar with hybrid-patterns.

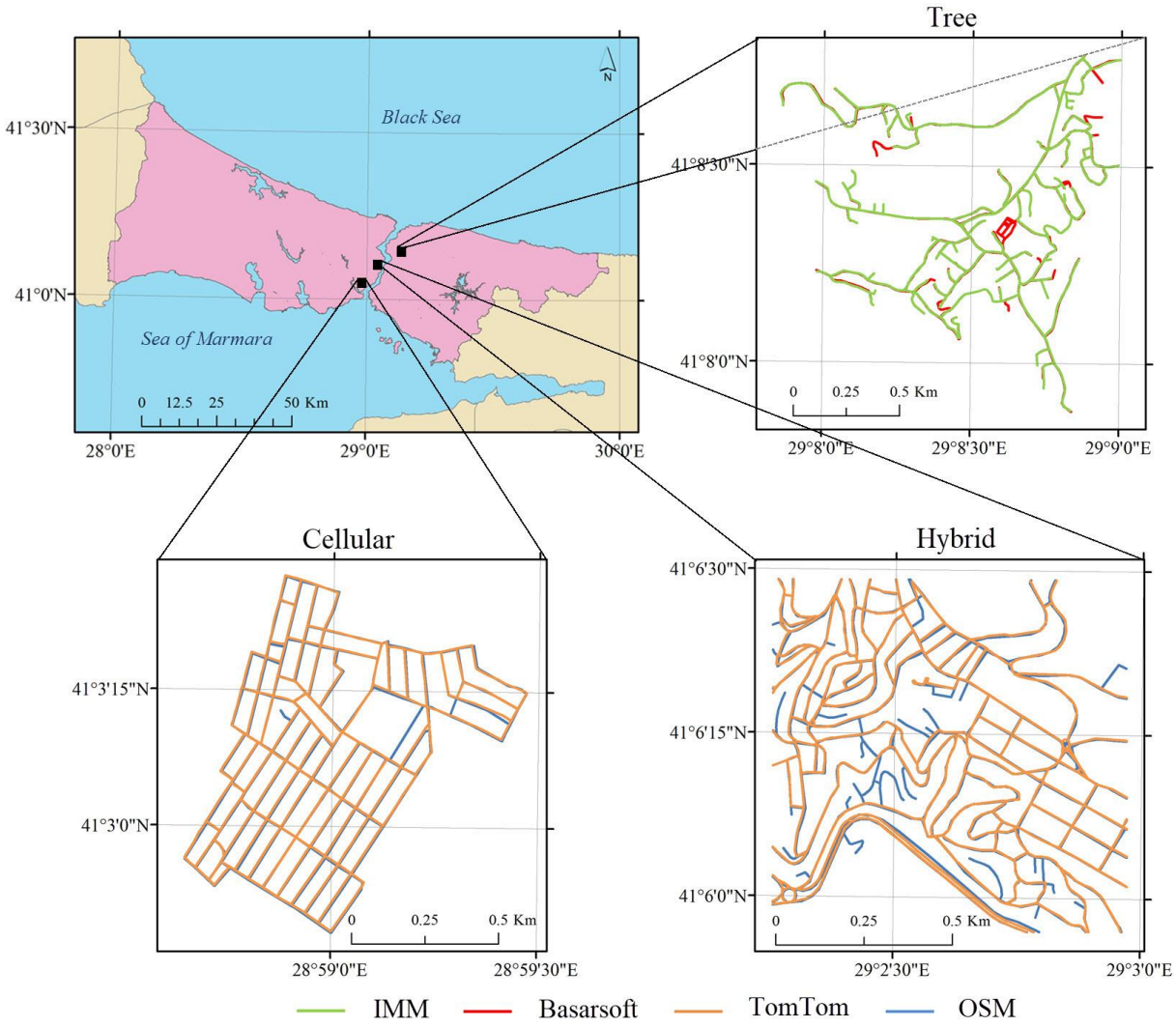

Figure 3. Tree-, cellular-, and hybrid-patterned road networks: IMM (green), Başarsoft (red), OSM (blue), and TomTom (orange)

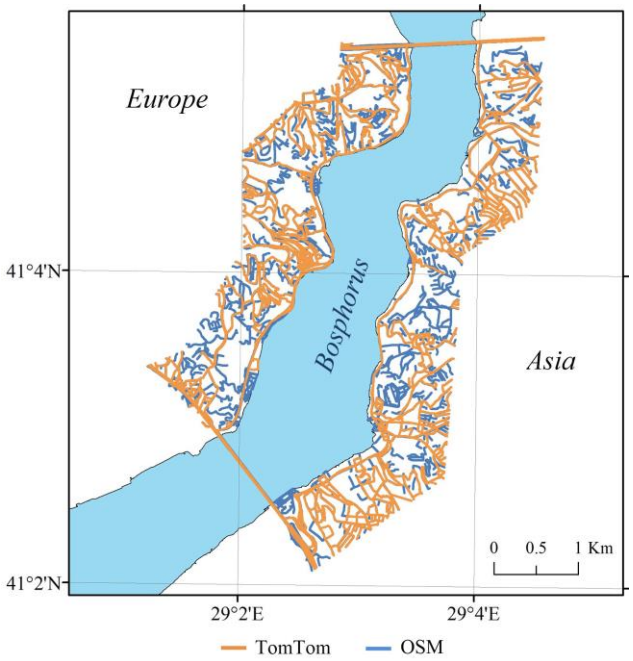

Figure 4. The road networks in Bosphorus, Istanbul: OSM (blue) and TomTom (orange)

Table 2. The number or objects and total road length in each dataset

Pattern	Source	The number of objects	Total length (km)
Tree	IMM	134	14.54
	Başarsoft	118	13.64
Cellular	OSM	153	16.22
	TomTom	146	15.87
Hybrid	OSM	288	21.95
	TomTom	221	19.69
Bosphorus	OSM	3030	221.60
	TomTom	1381	141.04

3.2. Pre-processing

The source datasets have different coordinate systems. This difference affects the calculation of similarity negatively. For example, the objects in the Başarsoft, TomTom, and OSM datasets have geographical coordinates in WGS84 datum. However, the measures used in the study are calculated in metric. Therefore, the geographical coordinates of the objects were transformed into the ITRF96 datum (Gauss-Krüger projection, Central meridian: 30° and GRS80 ellipsoid)

where the IMM dataset was defined. Furthermore, two road networks were aligned using linear rubber-sheet transformation. Moreover, we set T distance threshold as 85m for tree- and cellular-patterned road networks and 50m for hybrid-patterned road network by using our previous matching experiences with source datasets and the study area.

3.3. Results and Evaluation

The results of the matching process were compared with the results of manual matching, and then, the numbers of correct and incorrect matches in Table 3 were determined. The evaluation was performed both integrated and separately with each geometric and topological measure. In the first stage of the approach, some results occurs categorically in accordance with the type of measures and road patterns. While Hausdorff distance measure performed the maximum number of correct and the least number of incorrect matches in both tree and cellular patterns, its result in hybrid pattern is different. Mean perpendicular distance performs the maximum number of correct matches. However, it also gave the most number of incorrect matches in hybrid patterns. Therefore, we examine the results of the measures by using their correctness and incorrectness percentages (Table 3). Hausdorff distance measure performed the maximum correctness and the minimum incorrectness in all patterns. Sinuosity and mean perpendicular distance measure gave the least correctness and the maximum incorrectness in cellular pattern. Orientation was the second best similarity measure in terms of both correct and incorrect matching in all patterns. From this point of view, it can be observed from Table 3 that mean perpendicular distance was the worst in all patterns. Similarly, mean length of triangle edges and modified degree of connectivity performed the least correctness and the most incorrectness in hybrid pattern. However, these measures gave similar results with orientation and sinuosity in tree.

The similarity scores used in the first stage were optimized by the E_i in Table 4 and new similarity scores to be used in the second stage were calculated as in Table 5.

Table 3. The numbers and percentages of correct and incorrect matching

			H[1]	O[2]	S[3]	P[4]	T[5]	C[6]	1. stage
Tree	Correct	Number	90	88	84	83	86	86	88
		%	78	54	49	40	43	47	75
	Incorrect	Number	26	75	86	125	114	97	30
		%	22	46	51	60	57	53	25
Cellular	Correct	Number	146	146	109	144	142	145	147
		%	95	39	33	33	37	39	94
	Incorrect	Number	7	233	224	299	246	231	9
		%	5	61	67	67	63	61	6
Hybrid	Correct	Number	191	191	182	195	181	189	190
		%	83	56	47	40	40	40	82
	Incorrect	Number	38	148	206	296	275	279	42
		%	17	44	53	60	60	60	18

[1]Hausdorff distance; [2]Orientation; [3]Sinuosity; [4]Mean perpendicular distance; [5]Mean length of triangle edges; [6]Modified degree of connectivity

Table 4. Efficiency rates (E_i) of similarity measures

E_i	H[1]	O[2]	S[3]	P[4]	T[5]	C[6]
Tree	2.00000	1.28409	1.03978	1.00000	1.03356	1.08765
Cellular	2.00000	1.16961	1.00000	1.00000	1.11875	1.17006
Hybrid	1.64067	1.32845	1.01742	1.00000	1.00000	1.02644

[1]Hausdorff distance; [2]Orientation; [3]Sinuosity; [4]Mean perpendicular distance; [5]Mean length of triangle edges; [6]Modified degree of connectivity

Table 5. The similarity scores used in the first and second stages of the approach

Stage	Pattern	S_H			S_O		S_S		S_P		S_T		S_C	
1.	All	4	2	1	4	2	2	1	2	1	4	2	4	2
2.	Tree	8	4	2	5.14	2.57	2.08	1.04	2	1	4.13	2.07	4.35	2.18
	Cellular	8	4	2	4.68	2.34	2	1	2	1	4.48	2.24	4.68	2.34
	Hybrid	6.56	3.28	1.64	5.31	2.66	2.03	1.02	2	1	4	2	4.11	2.05

In the second stage, the relationships between the candidates were determined with new similarity scores in Table 5 and the process was performed for the last time. Accordingly, while the proposed approach, with

the updated (optimized) scores, performed almost the same number of matches as the number of manual matching in tree and cellular patterns, some missing matching occurred in hybrid pattern (Table 6). The missing matching is related to two parameter: (1) matching capability of the approach and (2) distance threshold. While the approach was common for all the source patterns, the distance threshold *T* was different in hybrid pattern. Therefore, possible reason for the missing matches of hybrid was *T*.

With the updated similarity scores, the number of correct matches increased by 4 and the number of incorrect matches decreased by 7 in tree-patterned roads. Although the number of incorrect matches decreased by 2 in cellular-patterned roads, the number of correct matches also decreased by 1. While there is no change in the number of correct matches in hybrid roads after second stage, the number of incorrect matches decreased by 8.

The operation of controlling the manual matching could have been too hard with over a thousand corresponding matching pairs in Bosphorus datasets. Therefore, after generating the final matching with whole datasets, the correct and incorrect matches was determined by comparing randomly selected sample data with manual matching (Fig. 5). In Table 6 and 7, the results are based on the sample of Bosphorus datasets.

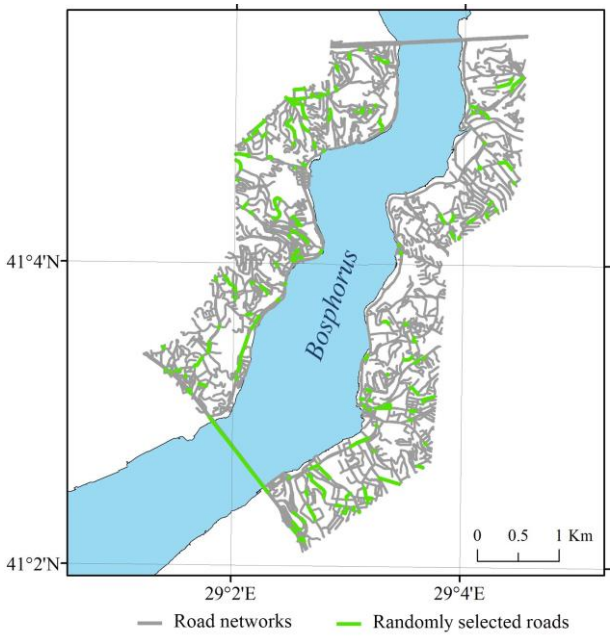

Figure 5. Randomly selected roads (green) and the whole road networks (grey) in Bosphorus datasets.

Since Bosphorus datasets consist of several types of patterns, it is better to examine matching instances in accordance with the pattern type separately. Fig. 6 shows correctly matched road lines with cellular pattern. They were matched correctly both in the first stage and the second stage. Both this visual instance and Table 6 show that the second stage of the proposed method almost have the same result with the first one in cellular patterned-road networks. Besides, while the northwest roads with hybrid pattern in Fig. 7 was matched correctly, the south was a missing match. The possible reason is that the corresponding roads have quite different geometric properties such as sinuosity and centroid. Moreover, the road 1 in Fig. 8 was matched incorrectly with the road 2' both in the first and second stage since the geometric and topological properties of the road 1 are more similar with the road 2' than with the road 1'. As a matter of course, there were expected instances showing us that the second stage optimized the matching process by eliminating the incorrect matches in the first stage. The road 1 Fig. 9b was matched with three roads in other datasets in the first stage. However, the matches with the roads 2' and 3' were incorrect. In the second stage, the efficiency rates ensured the elimination of the incorrect matches.

Table 6. Final results of the matching process by means of matching numbers

		Cor.[1]	Incor.[2]	Miss.[3]	Sum
Tree	Man.[4]	116	-	-	116
	1.Stage	88	30	-	118
	2.Stage	92	23	1	115
Cellular	Man.[4]	150	-	-	150
	1.Stage	147	9	-	156
	2.Stage	146	7	-	153
Hybrid	Man.[4]	262	-	-	262
	1.Stage	190	42	30	232
	2.Stage	190	34	38	224
Bosphorus sample (Hybrid)	Man.[4]	151	-	-	151
	1.Stage	114	25	12	139
	2.Stage	114	18	19	132

[1]Correct; [2]incorrect; [3]missing; [4]manual matching

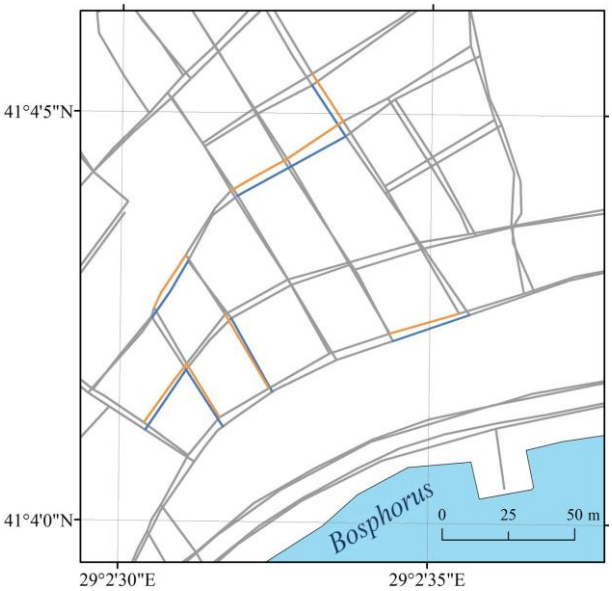

Figure 6. Correct matches in the cellular pattern

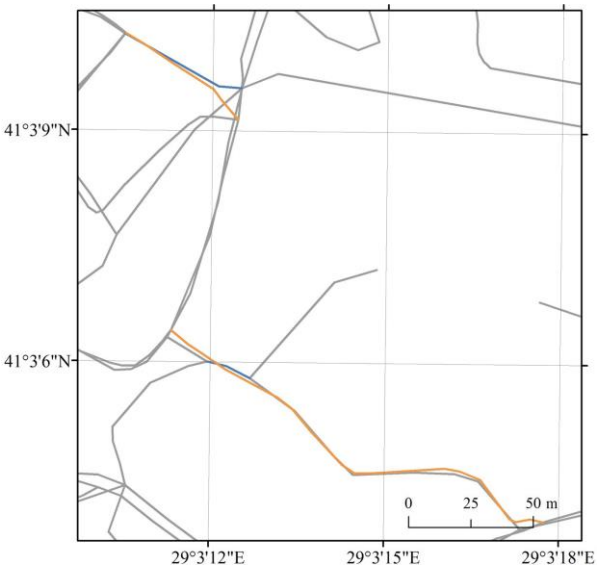

Figure 7. Correct (northwest) and missing (south) matches

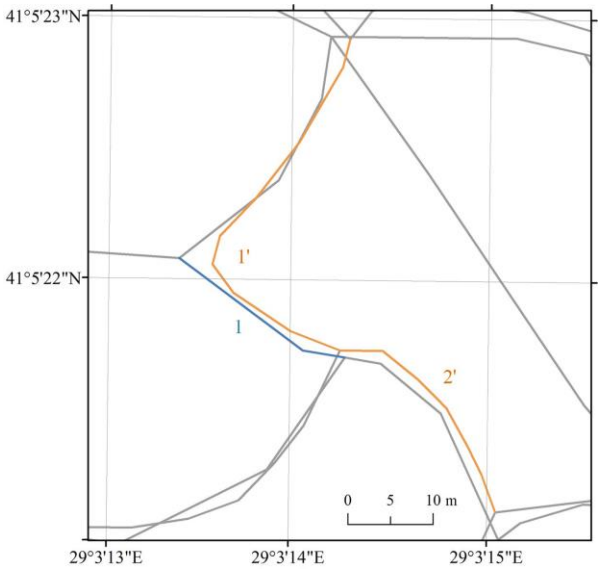

Figure 8. Incorrect matches in the hybrid pattern

Determining the accuracy of a matching study only by the correct matches is not sufficient. For example, in a study area, there are 100 manually detected possible matches and a selected automated method performed 10 matches only. If none of the 10 matches is incorrect, the method is considered to have worked with 100% correctness. However, according to manual matching, the method could not identify 90 matches. This shows that completeness should also be taken into account when making assessments of accuracy. Therefore, three of the frequently used measures of statistical analysis in data science; *precision* (Eq. 7), *recall* (Eq. 8) and *F-measure* (Eq. 9) were used to evaluate the proposed method (Samal et al., 2004; Song et al., 2011; Fan et al., 2016).

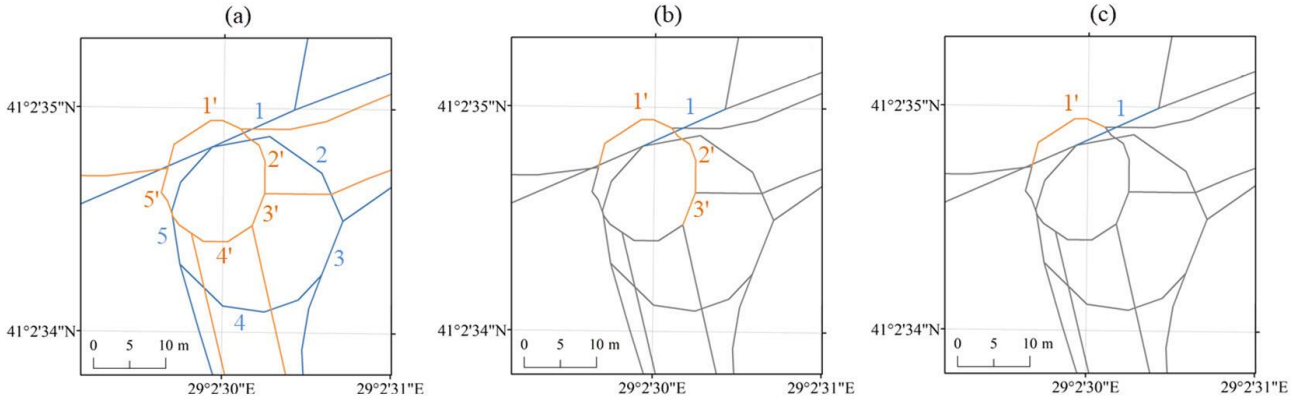

Figure 9. Manual (a), the first stage (b), and the second stage (c) matching

$$Precision = \frac{N_{Correct}}{N_{Correct} + N_{Incorrect}} \quad (7)$$

$$Recall = \frac{N_{Correct}}{N_{Correct} + N_{Mismatch}} \quad (8)$$

$$F - measure = \frac{2 \times Precision \times Recall}{Precision + Recall} \quad (9)$$

Three parameters have been used in the statistical measures: Number of correct matches (true positive), number of incorrect matches (false positive), and number of missing matches (false negative) ($N_{Mismatch}$). The number of missing matches was obtained by subtracting the total number of matches performed by the method (sum of true and false matches) from the number of manual matches.

The *precision* measure is a ratio of the number of correct matches to the total number of matches. Therefore, the *precision* was used as the accuracy indicator. *F-measure* is an evaluation measure in which the *precision* (accuracy) and *recall* (completeness) together affect in a balanced way. In the second stage of the method, the accuracy increased by 5.4%, 1.2%, 2.9%, and 4.4% in tree-, cellular-, and hybrid-patterned roads and Bosphorus sample, respectively (Table 7). It can be said that the results are satisfactory in terms of accuracy. *Recall* is a measure of how complete the methods are performed. For instance, when Table 6 is examined carefully, comparing with the manual matching result, the proposed approach performed two more matchings (over-matches) in the first stage and one missing in the second stage with tree-patterned roads. As seen in Table

7, the completeness is 100% in the first stage and 98.9% in the second stage. This means that over-matches do not affect the value of the *recall* measure. This also indicates that the *recall* value cannot be a standalone measure for the evaluation, but can be used to interpret the accuracy. From this point of view, recall value presented that the proposed approach ensured high completeness (almost fully complete). Therefore, the accuracy of the study is quite reliable. In hybrid-patterned roads, the recall value decreased in the second stage. This is because of that while the number of incorrect matches decreased, the number of missing matches increased. Also, F-measure increased by 3.1% and 0.7% in tree and cellular patterns. It has no change in hybrid pattern since (1) the number of correct matches had no change, and (2) decreasing number of incorrect matches was added to number of missing matches in both stages.

Table 7. The results of the evaluation measures

		Prec.[1] (%)	Rec.[2] (%)	F-m.[3] (%)
Tree	1.Stage	74.6	100	85.4
	2.Stage	80.0	98.9	88.5
Cellular	1.Stage	94.2	100	97.0
	2.Stage	95.4	100	97.7
Hybrid	1.Stage	81.9	86.4	84.1
	2.Stage	84.8	83.3	84.1
Bosphorus sample (Hybrid)	1.Stage	82.0	90.5	86.0
	2.Stage	86.4	85.7	86.0

[1]Precision; [2]recall; [3]f-measure

The number of correct matching of each measure is close to each other (Table 3). Therefore, the correct matching numbers have no specifics. This assessment supports the proposed efficiency formula in which the incorrect matches are used. Moreover, Hausdorff distance performed the number of correct matches at least 3.5 times greater than the number of incorrect matches (Table 3). Other measures performed many incorrect matches. Sinuosity and mean perpendicular distance performed the worst in cellular pattern since most of the corresponding road lines has low curvature. The results show that some of the similarity measures are more important than others for the pattern type on which they are used. For instance in our experiments, while Hausdorff distance was the best-matcher for all patterns, the mean length of the triangle edges was the worst-matcher for only hybrid pattern. This kind of changeable order between measures clearly supports the proposed approach that optimizes the similarity scores using the efficiency rates.

4. CONCLUSION

This paper proposes a semi-automated approach for road objects in line geometry. Besides, since it determined the efficiency rates for the tree-, cellular-, and hybrid-patterned road network datasets, the second stage of the proposed approach can be performed automatically with the road networks in a similar pattern. For a road network with a different pattern, the efficiency rates must be recalculated since the similarity measures have different correctness and incorrectness in terms of the pattern type (Table 3). In addition, efficiency rates can be calculated using small samples for datasets containing a large number of road objects, and then, applied to the source datasets. In this case, after the efficiency rates are determined semi-automatically by a manual matching operator using randomly selected samples, the actual large data is matched automatically using these efficiency rates. To prove the efficiency of the proposed approach, we conducted an additional matching process with OSM and TomTom road networks in Bosphorus, Istanbul. Since the Bosphorus networks were hybrid-patterned, the efficiency rates had no need to be computed again. This enables the matching process with the same patterned roads to start directly from the second stage.

Utilization of Maximum-Minimum normalization and the exponential function enabled the efficiency rates to be ranged between 1 and 2. Thus, even the mean perpendicular distance was used as the least significant measure in the similarity calculation.

The proposed approach does not use any semantic information to determine the similarity between objects. Instead, the similarities are calculated on the basis of scores based on geometric and topological measures. The optimization process updates the scores using the efficiency rates.

In this study, the scoring rules and the geometric and topological measures were taken from the study of Hacar and Gökgöz (2019b). However, the proposed approach can be used to adapt different kind of scoring rules using different geometric and topological measures that are specific to the characteristics of the source datasets.

The proposed approach has an *F-measure* over 86% in hybrid-patterned Bosphorus datasets. The results are satisfactory in terms of accuracy and completeness. The experimental testing also show that there is no need to conduct a second stage for the cellular-patterned road networks.

Computing the time of the matching process is a hard task since the process is conducted semi-automatically. The process time changes according to the experiences of the matching operator in the stage of manual results. This may occur the disadvantage that prevents planning the geo-process routines.

ACKNOWLEDMENT

The authors would like to thank IMM Directorate of Geographical Information Systems, The Traffic Stats Customer Service Team in TomTom, and Basarsoft Information Technologies Inc. for supplying road datasets and OpenStreetMap community for their contributions.

REFERENCES

Araújo T, Pires C, Mestre D, de Queiroz A, Santos V & da Nóbrega T (2019). A Parallel-based Map Matching Approach over Urban Place Records. Anais do XXXIV Simpósio Brasileiro de Banco de Dados, 121-132. Porto Alegre: SBC.

Başaraner M (2011). A zone-based iterative building displacement method through the collective use of Voronoi tessellation, spatial analysis and

multicriteria decision making. Boletim de Ciências Geodésicas, 17(2), 161-187.

Bilgi S, Gulnerman A G, Arslanoğlu B, Karaman H & Öztürk Ö (2019). Complexity measures of sports facilities allocation in urban area by metric entropy and public demand compatibility. International Journal of Engineering and Geosciences, 4(3), 141-148.

Chehreghan A & Ali Abbaspour R (2018). A geometric-based approach for road matching on multi-scale datasets using a genetic algorithm. Cartography and Geographic Information Science, 45(3), 255-269.

Cobb M A, Chung M J, Foley III H, Petry F E, Shaw K B & Miller H V (1998). A rule-based approach for the conflation of attributed vector data. GeoInformatica, 2(1), 7-35.

Fan H, Yang B, Zipf A & Rousell A (2016). A polygon-based approach for matching OpenStreetMap road networks with regional transit authority data. International Journal of Geographical Information Science, 30(4), 748-764.

Guo Q, Xu X, Wang Y & Liu J (2019). Combined Matching Approach of Road Networks under Different Scales Considering Constraints of Cartographic Generalization. IEEE Access, 8, 944-956.

Hacar M (2019). Yol Ağlarının Geometrik Entegrasyonu için Nesne Eşleme Yöntemlerinin Geliştirilmesi. PhD Thesis, Yildiz Technical University, Istanbul.

Hacar M (2020). A rule-based approach for generating urban footprint maps: from road network to urban footprint. International Journal of Engineering and Geosciences, 5(2), 100-108.

Hacar M & Gökgöz T (2019a). A conceptual model for geo-object matching. International Symposium on Applied Geoinformatics (ISAG-2019), 7-9 November 2019, Istanbul, Turkey, 97-102.

Hacar M & Gökgöz T (2019b). A New, Score-Based Multi-Stage Matching Approach for Road Network Conflation in Different Road Patterns. ISPRS International Journal of Geo-Information, 8(2), 81.

Kilic B & Gülgen F (2020). Accuracy and similarity aspects in online geocoding services: A comparative evaluation for Google and Bing maps. International Journal of Engineering and Geosciences, 5(2), 109-119.

Koukoletsos T, Haklay M & Ellul C (2012). Assessing data completeness of VGI through an automated matching procedure for linear data. Transactions in GIS, 16(4), 477-498.

Lei T & Lei Z (2019). Optimal spatial data matching for conflation: A network flow-based approach. Transactions in GIS, 23(5), 1152-1176.

Li L & Goodchild M F (2011). An optimisation model for linear feature matching in geographical data conflation. International Journal of Image and Data Fusion, 2(4), 309-328.

Lynch M & Saalfeld A (1985). Conflation: automated map compilation – a video game approach. Proceedings of Autocarto 7, 11–14 March 1985 Washington, DC, USA, 343-352.

Memduhoğlu A & Başaraner M (2018). Possible contributions of spatial semantic methods and technologies to multi-representation spatial database paradigm. International Journal of Engineering and Geosciences, 3(3), 108-118.

Mustière S & Devogele T (2008). Matching networks with different levels of detail. GeoInformatica, 12(4), 435-453.

Olteanu-Raimond A M, Mustiere S & Ruas A (2015). Knowledge formalization for vector data matching using belief theory. Journal of Spatial Information Science, 2015(10), 21-46.

Pourabdollah A, Morley J, Feldman S & Jackson M (2013). Towards an authoritative OpenStreetMap: conflating OSM and OS OpenData national maps' road network. ISPRS International Journal of Geo-Information, 2(3), 704-728.

Rosen B & Saalfeld A (1985). Match criteria for automatic alignment. Proceedings of 7th international symposium on computer-assisted cartography (Auto-Carto 7), 11–14 March 1985 Washington, USA, 1-20.

Ruiz J J, Ariza F J, Urena M A & Blázquez E B (2011). Digital map conflation: a review of the process and a proposal for classification. International Journal of Geographical Information Science, 25(9), 1439-1466.

Saalfeld A (1988). Conflation automated map compilation. International Journal of Geographical Information System, 2(3), 217-228.

Samal A, Seth S & Cueto 1 K (2004). A feature-based approach to conflation of geospatial sources. International Journal of Geographical Information Science, 18(5), 459-489.

Song W, Keller J M, Haithcoat T L & Davis C H (2011). Relaxation-based point feature matching for vector map conflation. Transactions in GIS, 15(1), 43-60.

Şen A (2013). The applicability of artificial intelligence methods for the selection/elimination process to the stream networks in cartographic generalization. Doctoral Thesis, Yildiz Technical University, Istanbul, Turkey.

Volz S (2006). An iterative approach for matching multiple representations of street data. Proceedings of the ISPRS Workshop on Multiple Representation and Interoperability of Spatial Data, Hannover, Almanya, 22–24 Feb 2006, 36(Part 2/W40), 101–110.

Xavier E, Ariza-López F J & Ureña-Cámara M A (2016). A survey of measures and methods for matching geospatial vector datasets. ACM Computing Surveys (CSUR), 49(2), 39.

Xiong D & Sperling J (2004). Semiautomated matching for network database integration. ISPRS journal of photogrammetry and remote sensing, 59(1-2), 35-46.

Yang B, Luan X & Zhang Y (2014). A pattern-based approach for matching nodes in heterogeneous urban road networks. Transactions in GIS, 18(5), 718-739.

Yuan S & Tao C (1999). Development of conflation components. Proceedings of geoinformatics, 99, 1-13.

International Journal of Engineering and Geosciences

https://dergipark.org.tr/en/pub/ijeg

e-ISSN 2548-0960

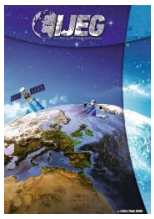

Investigation of Temporal Baseline Effect on DEMs Derived From COSMO Sky-Med Data

Ahmet Tarık Torun[*1], **Osman Orhan** [2]

[1]*Aksaray University, Faculty of Engineering, Geomatics Department, Aksaray, Turkey*
[2]*Mersin University, Institute of Science and Technology, Department of Remote Sensing and GIS, Mersin, Turkey*

Keywords
InSAR
DEM
Baseline
COSMO Sky-Med

ABSTRACT

Digital elevation models (DEM) are indispensable elements of sensitive earth science studies. It is important the production and usage of DEMs. The science of remote sensing offers scientists an important source of data on this subject. Radar data, which is an active remote sensing system, has an important capacity in this regard. DEM production using InSAR data has been widely used in the literature in the last decade. The temporal baseline parameter, which is an important factor in data generation from InSAR pairs, also affects the final products. In this study, it is aimed to examine the usability of these data by producing short (4days), medium (84 days) and long (440 days) baseline DEMs using InSAR pairs of COSMO Sky-Med satellite. At the same time, photogrammetric DEMs were produced with unmanned aerial vehicles (UAV) in selected pilot areas. The DEMs produced were evaluated in 4 land surface types, namely plain-bare, agricultural, urban and rugged area. In addition, by performing statistical analyzes such as RMSE, MAE, the accuracy of the produced DEMs compared to the DEMs produced with UAV was examined. The results showed that short and medium baseline data give more accurate results than long baseline InSAR pairs. Increasing the temporal baseline, increases the amount of error in the DEMs produced. Also, the effect of land surface types on the produced DEMs was revealed in the results of the study.

1. INTRODUCTION

The concept of the "Terrain Model" depicted as a numerical representation of the topographic surface, was first defined by Miller and Laflamme (1958). In the following years, several terms related to the representation of the topographic surface have been defined (Szypuła 2017). Among many terms, it is the digital elevation model (DEM) that is the most common and accepted in geomorphometric and GIS terminology. DEM is a shape that helps us to describe the earth mathematically, with a series of height measurements at regular/irregular intervals to best show the surface in 3D projection. In general, DEM is divided into two categories: a digital terrain model (DTM) that is free from trees, buildings and all kinds of objects, and a digital surface model (DSM) that reflects all man-made and natural objects (Martha et al. 2010).

DEMs are considered useful in many geospatial studies and applications, natural disasters (Hengl and Evans, 2009; Orhan et al. 2020a), archeology (Hageman et al. 2000), glacier and glacier analysis (Bishop et al. 2001), hydrology (Yang et al., 2015), plant cover research, urban studies, geomorphology and topography (Erasmi et al. 2014; Pope et al. 2007). Therefore, DEMs that provide information about the topography surface are essential for several different studies that are often of interest to geomorphologists as a starting point for further analysis (Güvenç, 2020). Several different techniques such as stereo satellite images, Interferometric SAR (InSAR), Global Navigation Satellite System (GNSS) measurements, topographic maps, contour lines, photogrammetry techniques, and laser scanning are used in the creation of the digital elevation model (Algancı et al. 2018; Peralvo and Maidment 2004).

* **Corresponding Author**

*(ahmettarik.torun@gmail.com) ORCID ID 0000-0002-7927-4703
(osmanorhan44@gmail.com) ORCID ID 0000-0002-1362-8206

Cite this article

Torun A T & Orhan O (2021). Investigation of Temporal Baseline Effect on DEMs Derived From COSMO Sky-Med Data. International Journal of Engineering and Geosciences, 6(3), 157-164

Research Article / DOI: 10.26833/ijeg.814319 **Received: 21/10/2020; Accepted: 13/11/2020**

Interferometric SAR (InSAR) has been developed as the most sufficient technologies to generate DEM with better resolution and high accuracy due to its all-weather, all-day characteristics, and the automatic high-efficiency processing methods (Zebker and Goldstein, 1986; Bamler and Hartl, 1998; Gao et al., 2017; Karabörk et al.2021). The InSAR technique is based on the principle of converting phase information obtained from a complex interferogram into elevation data. Both amplitude and phase information of microwave energy are measured in SAR systems. While the amplitude information depends on the electrical properties such as humidity, chemical substance content and geometric properties such as surface roughness, texture, the phase information depends on the distance between the satellite platform and the earth surface, like LiDAR and GNSS systems (Erten et al. 2018).

Space-based techniques such as InSAR are highly preferred in DEM production. Before 2007, only high-resolution stereo optical images were used in the production of high-resolution space-based DEMs (Sefercik et al. 2020). However, with the launched of high-resolution SAR satellites such as COSMO Sky-Med (COnstellation of small Satellites for Mediterranean basin Observation) after 2007, it has enabled the production of high-resolution DEMs under all weather conditions. The COSMO-SkyMed system, which is the unique constellation of four X-band radar satellites for Earth Observation, offers high-resolution SAR data (1m for Spotlight mode) for DEM generation. However, due to the re-pass monostatic imaging geometry, the performance of the generated DEMs was limited (Sefercik et al. 2020). The change in the earth's surface observed with the SAR images acquired at different dates causes a decrease in the coherent between the two SAR imaging systems. So, this situation prevents obtaining reliable phase data in the generation of elevation data. Therefore, the time difference between the SAR images is the main source of error in the produced DEM, and it has caused the production of DEM with low accuracy, especially in regions such as agricultural land where the temporal change is fast on the topography (Erten et al. 2018). In order to minimize limitations and increase the accuracy of acquired DEMs, COSMO Sky-med satellite works with the tandem-like interferometry system (within a 24-hour delay).

In the literature, there is a lack of information about the effect of different temporal baselines of SAR images on the DEMS derived from COSMO Sky-Med data. In this context, it is aimed to evaluate the accuracy of DEMs produced by using three COSMO Sky-med image pairs with different baselines (4-84-440 days) over the various types of surfaces such as plain-bare, rugged, agriculture and urban. UAV was used as base data in to assess the accuracy of DEM derived from COSMO Sky-Med data.

2. STUDY AREA AND MATERIALS

2.1. Study Area

Karapınar is a district located approximately 100 km east of Konya and is generally built on plains. Although traditional dry farming is practiced in the region, it has caused the emergence of karstic surface shapes due to irrigated agriculture and the geological structure of the region since the early 2000s (Orhan et al. 2020a). Sinkhole formations, which are caused by the misuse of groundwater in the region and continue to emerge day by day, threaten the people of the region (Orhan et al. 2020b). The main factor in choosing the study area is the coexistence of different land features in the region. Pilot areas with 4 different land surface types (plain-bare, agricultural, urban, rugged) determined in the study area were used in this study. Figure 1 provides the general boundaries of the study area and the selected pilot areas.

2.2. Materials

SAR images of the COSMO Sky-Med sensor were used in the study. COSMO Sky-Med, is a system that detects in X band and consists of 4 constellations, conceived by ASI (Agenzia Spaziale Italiana). The system is capable of observing in 3 imaging modes as spotlight, stripmap and scansar. The system can operate with single, double or full polarization. The revisit period of the system can be up to 1 day (Covello et al., 2010). In this study, 3 InSAR pairs, obtained with COSMO Sky-Med sensor, were used. InSAR pairs were created considering the temporal baselines. While selecting the InSAR pairs for DEM generation, care has been taken to ensure that other properties (polarization, orbital pass etc.) are the same, except for the baseline. Temporal baselines of selected InSAR pairs are 4 days, 84 days and 440 days, respectively. Technical information of the InSAR pairs used is presented in Table 1.

In addition to the InSAR data, photogrammetric flights were carried out using UAVS to control the produced DEMs on 15th of March 2016. In the study, photographs were taken using a DJI Phantom 4 model UAV at flight height of 100m, with overlap ratio of 80%. Ground control points have been established on the land surface to be used in evaluating the photographs. GCPs are designed in size that can be selected from photographs. In addition, red and white colors are used to distinguish it from photographs. The coordinates of GCPs were determined by precise GNSS measurements using with real time kinematic (RTK) method. The UAV and GCP used in the study are shown in Figure 2.

Table 1. COSMO Sky-med image specifications

	InSAR Pair 1	InSAR Pair 2	InSAR Pair 3
Acquisition Date	11.03.2016 15.03.2016	11.03.2016 03.06.2016	11.03.2016 25.05.2017
Orbit Pass Polarization		Descending VV	
Perp. Baseline (m)	466.04	52.43	41.49
Temp. Baseline (days)	4	84	440
Height of Ambiguity (m)	13.88	123.41	155.95
Doppler Difference (Hz)	485.49	337.58	37.85

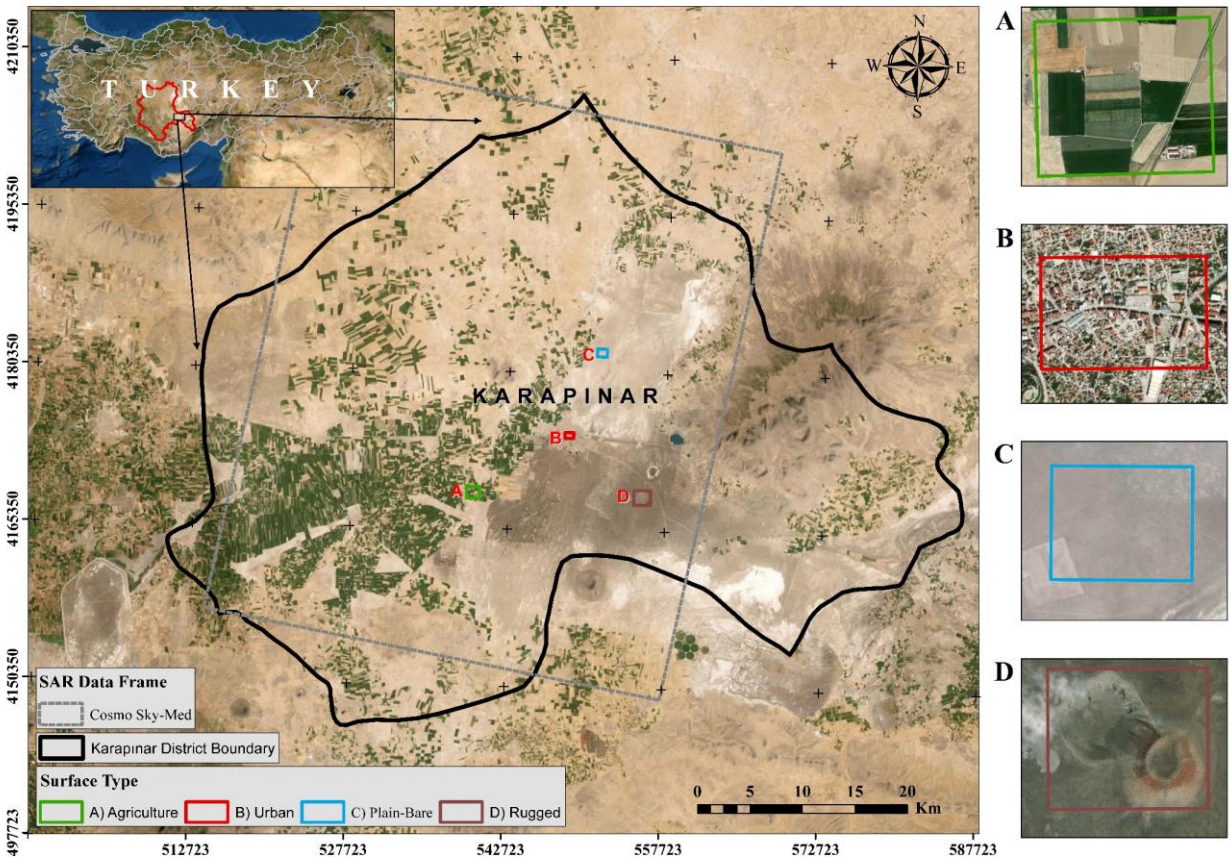

Figure 1. Study areas, A) Agriculture B) Urban C) Plain-Bare D)Rugged.

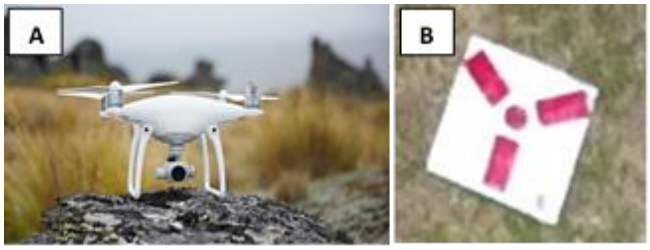

Figure 2. A) UAV b) GCP

3. METHODS

Digital Elevation Model (DEM) generation method with InSAR technique was used in the study. As known, InSAR is a radar imaging technique mostly used in remote sensing and geodetic studies (Abdikan, 2007). InSAR technique is based on combining images obtained with radar systems for studies such as DEM generation, deformation measurements and glacier studies (Hanssen, 2001). This technique involve information calculated by acquiring the phase difference of the appropriate image points in each of the two SAR images. The phase difference can be thought of as the value of the temporal difference, in terms of angle, between signals sent to the same location and having the same frequency (Yılmaztürk, 2015).

Digital Elevation Model (DEM) is defined as a data set that presents the elevation information and characteristics of the topography in 3 dimensions (Sefercik, 2007). DEMs can be used as a base for many analyzes that require elevation information in the field of earth sciences. DEMs, can be produced by techniques such as ground survey, aerial photogrammetry, remote sensing, laser scanning and InSAR (Amans et al. 2013; Algancı et al., 2018).

DEM generation with the InSAR technique is based on the process of superimposing, one of the two images of the same region taken at different times as the master image and the other as the slave image (Kyaruzi, 2005). DEM generation process from radar images consists of coregistration, inteferogram generation, phase filtering, phase unwrapping, conversion of phase information to height information and geometric correction stages, respectively (Crosetto ve Crippa, 2000). Figure 3 provides DEM generation stages with InSAR technique.

Coregistration is one of the main steps in interferometric image processing. For this process to occur, at least two SAR images must have similar acquisition geometries. The slave image must match the main image (Gens, 1998; Sefercik, 2010). In the image registration step, operations are carried out under three main headings as stack, cross- correlation and warp. The stack operator is the geographic resampling of two images (master and slave) that are generated by repeated scanning of the same region. Meanwhile, the values of the slave image are resampled according to the master image. The cross-correlation process step is the alignment of the same point on the earth that matches the master image. The warp operator that working with the cross-correlation, performs a mathematical calculation using GCPs automatically generated by the software for matching.

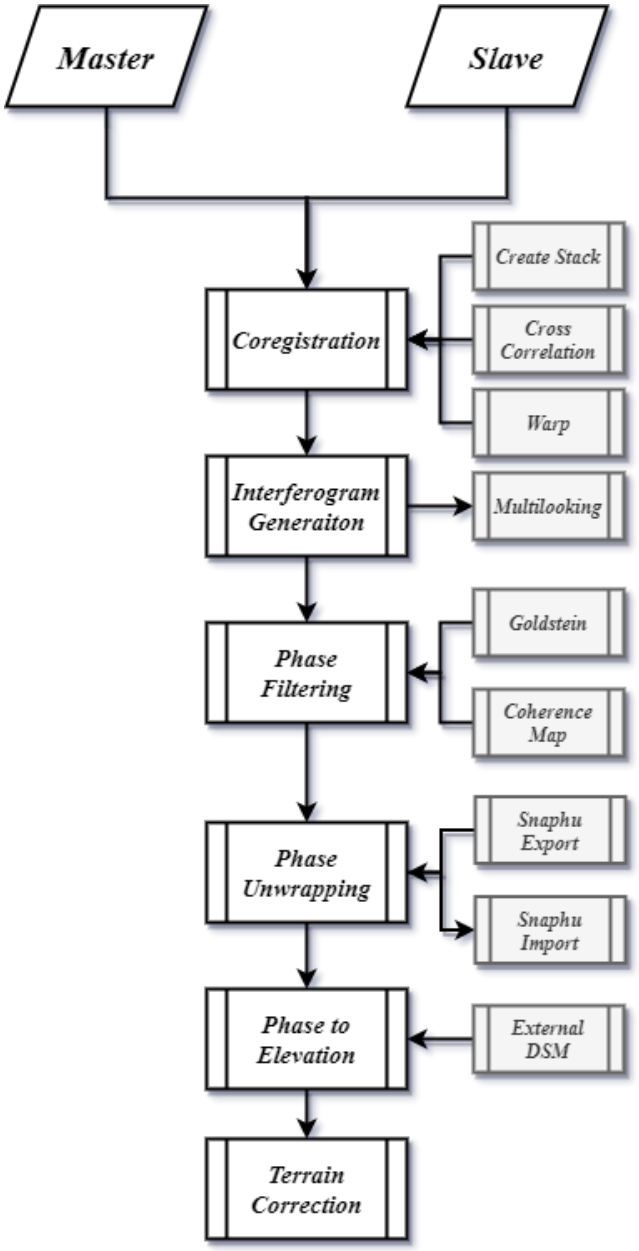

Figure 3. InSAR DEM generation flowchart

Interferograms are images obtained from two different SAR images of the same region and that contain the phase difference information between these two images (Richards, 2009). With the interferogram generation step, a more useful single image is generated by using the InSAR pair. The amplitudes of the corresponding pixels in both images are averaged and the difference of the phase values for each point in the image is calculated. The new image obtained after all these processes is called as interferogram.

Filtering is a process performed to increase the signal to noise ratio to increase the quality of the interferogram. The filter softens the spectrum of the interferogram into small pieces, using the amplitude values of the spectrum. In this process, the noise in the image is assumed to be lower than the other signals and suppressed and large amplitudes are enriched by assuming that the actual signal in the spectrum has a relatively large amplitude (Şengün, 2009). The most widely used filter in the literature is the adaptive phase filtering developed by Goldstein and Werner (Şengün, 2009; Song et al., 2014).

The interferogram showing the height differences of the topography is the module of 2π. The interferogram contains uncertainty in its content. To obtain height information at each point in the image, the correct integer number of phase cycles must be added to each measurement. The process of removing this uncertainty is called phase unwrapping.

Elevation information obtained from InSAR data is calculated with satellite orbit parameters and specific satellite geometry. Satellite orbit parameters are produced in The Earth Centered Earth Fixed (ECEF) coordinate system. This shows that a reference ellipsoid is needed for elevation calculations (Gens, 1998; Sefercik, 2010). For this reason, a reference DEM is used when performing the phase-elevation conversion. Shuttle Radar Topography Mission (SRTM) elevation models were used as the reference DEM for all images in this study.

The geometric correction of SAR images is different from optical images. Since SAR data have a side view geometry, a geometric distortion occurs on the data produced. Since SAR systems cause nonlinear compression, they cannot be corrected using polynomials. A geometric correction should be made by considering the sensor and processor characteristics (Sefercik, 2010). At this stage, the Range-Doppler terrain correction method is used for SAR images. This method assures the correction of geometric distortions caused by factors such as foreshortening and shadow, using a DEM to correct the position of each pixel.

To compare the DEMs produced with the InSAR technique, the reference DEM to be used in the analysis was produced by evaluating the determined areas with photogrammetric methods with an UAV. At this stage, unique flight plans were prepared for each region, with 100 m flight altitude and 80% longitudinal overlap (Figure 4). Also, 20 GCPs were used for each pilot area and 10 of them were reserved for testing the model produced.

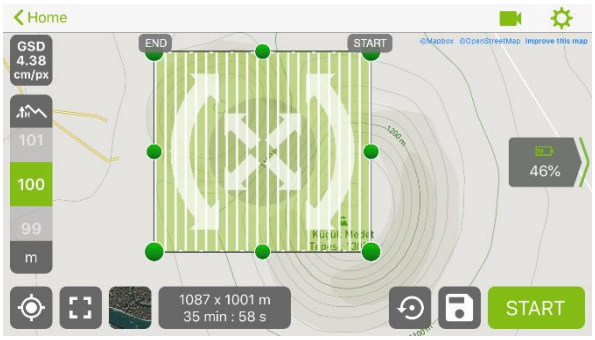

Figure 4. Flight plan sample

As a result of the photogrammetric evaluation of the photographs, 3D model of the land surface and orthomosaic image can be obtained. During these processes, all photographs are evaluated using the coordinates of the GCPs established on the land surface as a reference. The produced data and GCPs were analyzed via Pix4d software. At the end of the process DEMs produced which have ±10cm precision. DEM

obtained at this stage of the study was used as a reference for the evaluation of DEMs produced from InSAR data.

3.1 Statistical Analysis

Statistical analyzes were made to evaluate the DEMs obtained in the study. Root Mean Square Error (RMSE), Relative Root Mean Square Error (R-RMSE), Normalized Root Mean Square Error (N-RMSE) and Mean Absolute Error (MAE) analyzes were performed, respectively.

RMSE is the most suitable evaluation method for DEM data (Yang and Hodler, 2000). MAE calculates the mean errors independent of the directions of the variables. In order to obtain the total error, the differences of reference and observation data should be summed and divided by the number of observations (Güvenç, 2020).

RMSE, R-RMSE, N-RMSE and MAE calculated by following equations (Eq. 1-4) respectively.

$$RMSE = \sqrt{\sum_{i=1}^{n} \frac{(Z_r - Z_o)^2}{n}} \quad (1)$$

$$R-RMSE = \sqrt{\sum_{1}^{n} \frac{1}{n}\left(\frac{Z_r - Z_o}{Z_o}\right)^2} \quad (2)$$

$$N-RMSE = RMSE / Z_r \quad (3)$$

$$MAE = \frac{\sum_{1}^{n}(Z_r - Z_o)}{n} \quad (4)$$

where Z_r is the elevation values of reference DEM, Z_o is the elevation values of observed DEM and n is the number of observations.

3.2 DEM Evaluation

Several processes have been applied to compare the produced DEMs with the reference DEM. Due to the coordinate systems and datum effects of the produced DEMs, there may be problems of not fully overlapping with each other on the horizontal. In order to eliminate this issue DEMSHIFT module of BLUH software developed by Dr. Karsten Jacobsen, Institute of Photogrammetry and Geoinformation (IPI), University of Hannover, Germany was used. The module can eliminate the horizontal position errors of the produced DEMs according to the reference DEM depending on the slopes of the land. Figure 5 shows the effect of horizontal position error on vertical accuracies. The error of ΔD of the X point given in Figure 5 was detected and corrected in the X and Y directions, and the overlapping of the data was achieved. As a result of this process, the height error of ΔZ is eliminated.

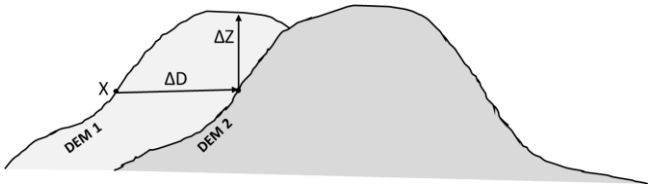

Figure 5. The effect of X-Y axis error on Z axis error (Adapted from Sefercik, 2018)

4. RESULTS and DISCUSSIONS

In the study, we compared short, medium and long-baseline data produced by interferometric methods and DEMs produced by UAVs and performed the statistical analysis. First of all, horizontal position errors of DEMs produced by interferometric methods were corrected by reference DEM by using the DEMSHIFT module (Jacobsen, 2005). Table 2 represents the applied corrections in X and Y directions according to the study areas. Figure 6 shows DEMs produced with InSAR data and UAV

Table 2. Horizontal shifting values of DEMs according to land surface types (LST)

Baseline / LST	Short		Medium		Long	
	X (m)	Y (m)	X (m)	Y (m)	X (m)	Y (m)
Plain-Bare	0.125	-2.852	0.149	-2.365	-0.834	2.279
Rugged	1.052	5.704	-1.097	-5.363	-1.535	-2.698
Urban	-0.294	2.689	-0.304	-2.700	-0.300	-2.691
Agriculture	1.373	4.829	1.383	-4.835	1.153	-4.867

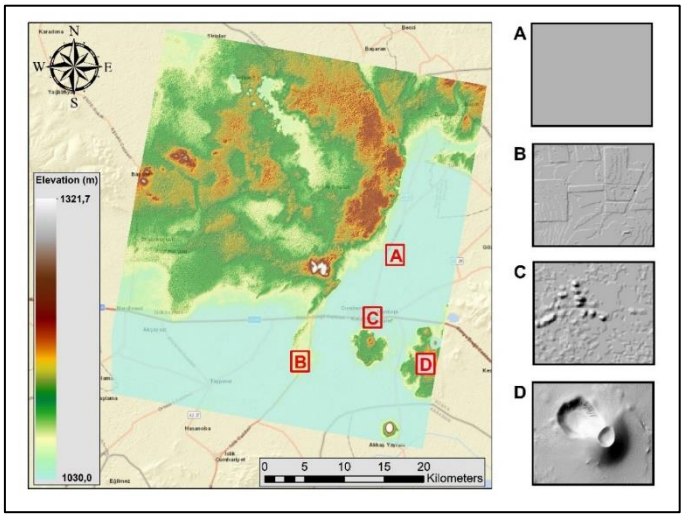

Figure 6. Produced DEMs with InSAR and UAV A) UAV Plain-Bare Area, B) UAV Agricultural Area, C) UAV Urban Area, D) UAV Rugged Area

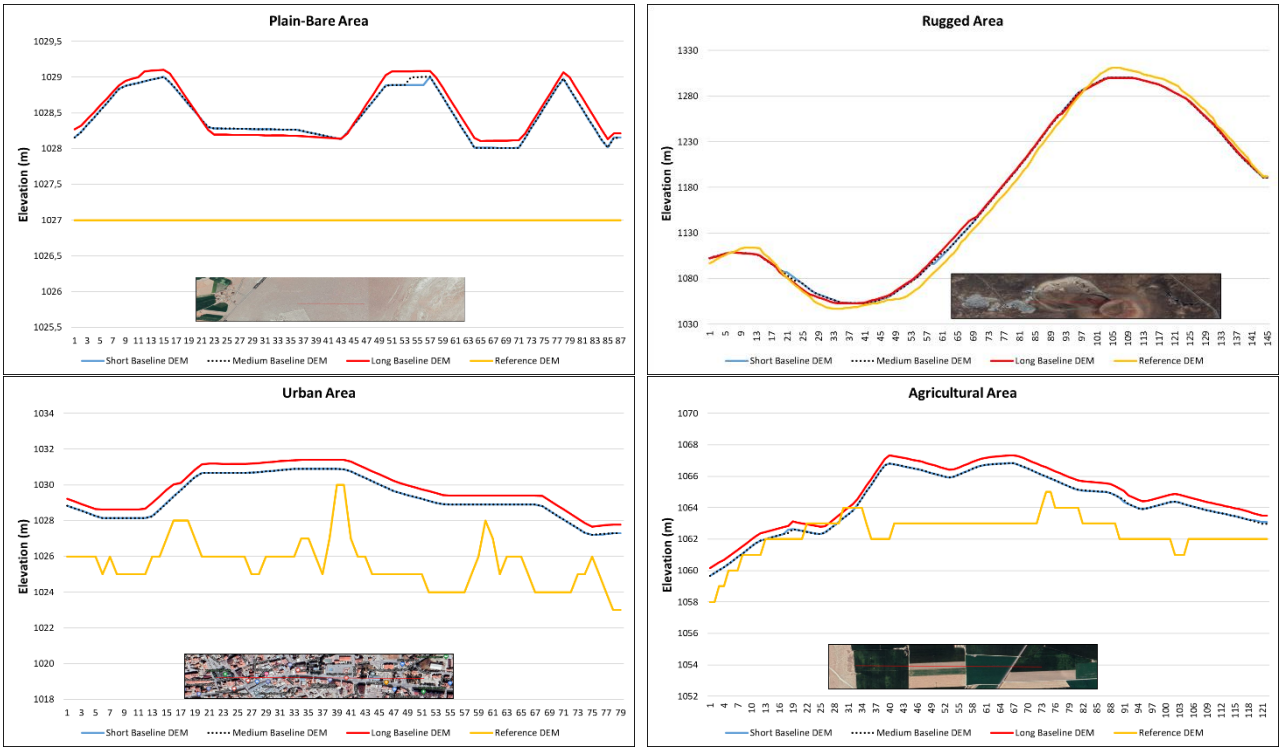

Figure 7. Profile plots according to land surface type

Profile graphics according to different land surface types are displayed in Figure 7. Profiles were extracted using the values taken from areas determined from different land surface types. When the profile charts are examined, it is clearly understood that InSAR data are affected by land surface types. On the other hand, generally, while short and medium baseline data indicate close values in all graphs, there are differences in data with long baseline. This situation is seen in the sections taken from the profile graphs.

Statistical analysis graphics applied to the data are shown in Figure 8.

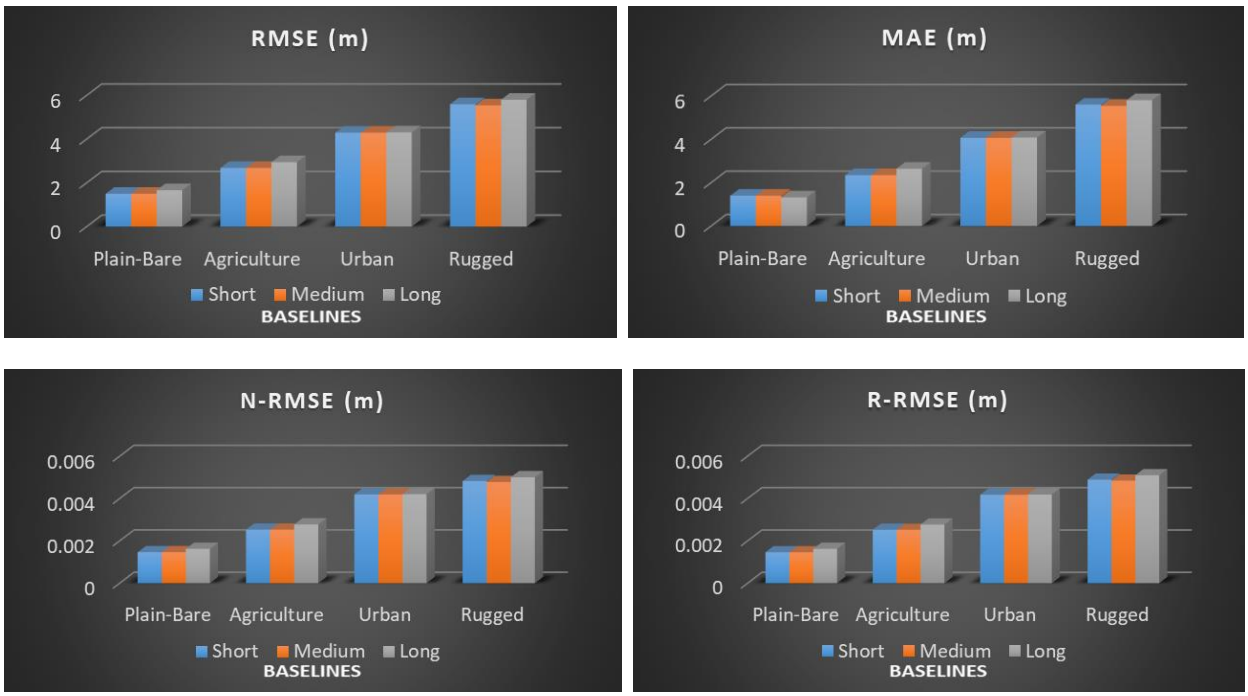

Figure 8. Statistical analysis results

The statistical analysis charts shown in Figure 8 were created using an average of 10000 control points for all areas. Statistical analyses have been calculated based on the reference DEM produced by UAV. In RMSE evaluations, it can be said that short baseline DEM (4days) generally has the smallest RMSE value compared to other DEMs. It has 1.5 m for the plain-bare area, 2.7 m for the agricultural area, 4.3 m for urban area and 5.6 m for the rugged area, RMSE value respectively. Also, it showed similar results in MAE values (1.4 m-2.3 m-4.1

m-5.6 m respectively). As well, R-RMSE and N-RMSE values gave similar results too. Considering the medium baseline DEM (84 days) data, it can be seen that there are no large deviations from the short baseline data. As shown in Figure 8, while better results are obtained for plain-bare areas in RMSE values, the error occurring in other areas increases. It is possible to observe these results in other statistical analyzes. Also, when the analysis results of long baseline DEM were examined, it was observed that there were apparent differences from other produced DEMs. RMSE values have reached 1.8 m for long baseline plain-bare area, 3 m for agricultural area, 4.3 m for urban area and 5.8 m for rugged area. In other analyzes, the differences of long baseline data appeared similarly.

The 1.5 m RMSE value obtained in the Plain-Bare area highlights an important point about the accuracy of the DEMs obtained. Also, when the produced DEMs are examined holistically, it is revealed that the average RMSE values are approximately 3.5 m. This shows that the absolute vertical error of the produced DEMs are better than the RMSE values of TSX-WorldDEM which is about 4 m (Airbus, 2018), SRTM DEM is 10 m (Farr et al., 2007), ALOS World3D DEM is about 5 m (Tadono et al., 2014) and ASTER GDEM V2 is about 9 m (Tachikawa et. al., 2011).

In this study, the effect of land surface types on accuracies was revealed more clearly because the baseline was not compared in a single land surface type. When the Figure 8 were examined, despite the elevation changes in plain-bare and agricultural land were not very different the RMSE values of the agricultural lands were higher than the plain areas. The noise effect of agricultural areas on InSAR data is reflected in the results in this way. At the same time, the buildings and urbanization factors that affect the DEM data caused deviations in the data of the urban areas. In addition, the rugged area data has the highest error value can be explained by the effects that occur during image acquisition (layover, shadow, foreshortening) in the radar data. Errors caused by the land surface during image acquisition also affect the result products produced with InSAR data.

5. CONCLUSION

In this study, DEMs produced from short, medium and long baseline data of COSMO Sky-Med satellite were compared with DEM produced by UAV. Profile graphics were drawn from the produced data and statistical analysis was performed on the data.

It is understood from all the analysis that long baseline data have larger deviations than short and medium baseline data. This is due to climate change, seasonal conditions and similar factors as well as errors that occur during the processing of InSAR pairs. It is obvious that not all land surface types will be the same. Therefore, the emergence of different results in different land surface types also creates a drawback in the use of long baseline data. The authors recommend that scientists avoid using long baseline data in DEM generation and deformation studies, where the results should be sensitive.

The fact that the comparisons made with the baseline of the COSMO Sky-Med satellite are limited in the literature makes this study unique. The results can be evaluated by diversifying the baselines and making different analyzes in future studies.

REFERENCES

Abdikan S (2007). SAR Görüntülerinden Üretilen İnterferometik Ve Stereo Sayısal Yükseklik Modellerinin Kalitesinin İncelenmesi. Master Thesis, Yıldız Technical University, Graduate School of Science and Engineering, Turkey.

Airbus (2018). WorldDEM™ Technical Product Specification, Airbus Defence and Space Intelligence.

Alganci U, Besol B & Sertel E (2018). Accuracy assessment of different digital surface models. ISPRS International Journal of Geo-Information, 7(3), 114.

Amans O C, Beiping W & Ziggah Y Y (2013). Assessing Vertical Accuracy of SRTM Ver. 4.1 and ASTER GDEM Ver. 2 using Differential GPS Measurements–case study in Ondo State, Nigeria. International Journal of Scientific and Engineering Research, 4(12), 523-531.

Bamler R & Hartl P (1998). Synthetic aperture radar interferometry. Inverse Probl, 14: R1–R54 .

Bishop M P, Bonk R, Kamp Jr U & Shroder Jr J F (2001). Terrain analysis and data modeling for alpine glacier mapping. Polar Geography, 25(3), 182-201.

Covello F, Battazza F, Coletta A, Lopinto E, Fiorentino C, Pietranera L, Valentini & Zoffoli S (2010). COSMO-SkyMed an existing opportunity for observing the Earth. Journal of Geodynamics, 49(3-4), 171-180.

Crosetto M & Crippa B (2000). Quality assessment of interferometric SAR DEMs. International Archives of Photogrammetry and Remote Sensing, 33(B1; PART 1), 46-53.

Erasmi S, Rosenbauer R, Buchbach R, Busche T & Rutishauser S (2014). Evaluating the quality and accuracy of TanDEM-X digital elevation models at archaeological sites in the Cilician Plain, Turkey. Remote sensing, 6(10), 9475-9493.

Erten E, Çelik M F & Şahin Z M (2018). TanDEM-X Digital Elevation Model Generation- TANDEM-X SayısalYükseklik Modelinin Oluşturulması. Harita Dergisi, 84(160), 47-54.

Farr T G, Rosen P A, Caro E, Crippen R, Duren R, Hensley S, Kobrick M, Paller M, Rodriguez E, Roth L, Seal D, Shaffer S, Shimada J, Umland J, Werner M, Oskin M, Burbank D & Alsdorf D (2007). The shuttle radar topography mission. Reviews of geophysics, 45(2).

Gao X, Liu Y, Li T & Wu D (2017). High Precision DEM Generation Algorithm Based on InSAR Multi-Look Iteration, Remote Sensing, 9, 741Tracking. Turkish Journal of Geosciences, 1(1), 1-7.

Gens R (1998). Quality Assessment of SAR Interferometric Data, Ph.D Thesis, Hannover, ISSN 0174 1454

Güvenç M (2020) Comparatıve evaluatıon of vertıcal accuracy of ground control poınts from ASTER-DEM SRTM-DEM wıth respect to ALOS-DEM. M.Sc. Thesıs. Hasan Kalyoncu Unıversıty Graduate School of Natural and Applıed Scıences.

Hageman J B, Bennett D A, Westcott K L & Brandon R J (2000). Construction of digital elevation models for archaeological applications. Practical Applications of GIS for Archaeologists: A Predictive Modelling Toolkit, 121-136.

Hanssen R F (2001). Radar interferometry: data interpretation and error analysis (Vol. 2). Springer Science & Business Media.

Hengl T & Evans I S (2009). Mathematical and digital models of the land surface. Developments in soil science, 33, 31-63.

Jacobsen K (2005). DEMs based on space images versus SRTM height models. In ASPRS annual convention Baltimore.

Karabörk H, Makineci H B, Orhan O & Karakus P (2021). Accuracy Assessment of DEMs Derived from Multiple SAR Data Using the InSAR Technique. Arabian Journal for Science and Engineering. https://doi.org/10.1007/s13369-020-05128-8

Kyaruzi J (2005). Quality Assessment of DEM from Radargrammetry Data. M.sc Thesis, International Institute for Geo-information Science and Earth Observation, Enschede, The Netherlandsz.

Martha T R, Kerle N, Jetten V, van Westen C J & Kumar K V (2010). Characterising spectral, spatial and morphometric properties of landslides for semi-automatic detection using object-oriented methods. Geomorphology, 116(1-2), 24-36.

Miller C L & Laflamme R A (1958). The Digital Terrain Model-: Theory & Application. MIT Photogrammetry Laboratory.

Orhan O, Kırtıloğlu O S & Yakar M (2020a). Konya Kapalı Havzası Obruk Envanter Bilgi Sisteminin Oluşturulması. Geomatik, 5(1), 92-104.

Orhan O, Yakar M & Ekercin S (2020b). An application on sinkhole susceptibility mapping by integrating remote sensing and geographic information systems. Arabian Journal of Geosciences, 13(17), 1-17.

Peralvo M & Maidment D (2004). Influence of DEM interpolation methods in drainage analysis. Gis Hydro, 4.

Pope A, Murray T & Luckman A (2007). DEM quality assessment for quantification of glacier surface change. Annals of Glaciology, 46, 189-194.

Richards J A (2009). Remote sensing with imaging radar (Vol. 1). Berlin: Springer.

Sefercik U (2018). Zamansal Baz Uzunluğunun İleri Nesil Yapay Açıklı Radar Uydu Verilerinin Konum Doğruluğu Üzerindeki Etki Analizi . Çukurova Üniversitesi Mühendislik-Mimarlık Fakültesi Dergisi , 33 (2) , 165-176 . DOI: 10.21605/cukurovaummfd.509184

Sefercik U G (2007). Comparison of DEM accuracies generated by various methods. In 2007 3rd International Conference on Recent Advances in Space Technologies (pp. 379-382). IEEE.

Sefercik U G (2010). Generation And Evaluation Of DEMs Derived By TERRASAR-X Insar Images. PhD diss., Zonguldak Karaelmas University, Graduate School of Science and Engineering, Turkey.

Sefercik U G, Buyuksalih G & Atalay C (2020). DSM generation with bistatic TanDEM-X InSAR pairs and quality validation in inclined topographies and various land cover classes. Arabian Journal of Geosciences, 13(13), 1-15.

Şengün Y S (2009). GPS ve Insar ölçülerini birlikte kullanarak İzmit depreminde oluşan deformasyonların belirlenmesi: Nokta seyrekleştirmede yeni bir algoritma. PhD Thesis, Istanbul Technical University, Graduate School of Science Engineering and Technology.

Song R, Guo H, Liu G, Perski Z, Yue H, Han C & Fan J (2014). Improved Goldstein SAR interferogram filter based on adaptive-neighborhood technique. IEEE Geoscience and Remote Sensing Letters, 12(1), 140-144. doi: 10.1109/LGRS.2014.2329498.

Szypuła B (2017). Digital elevation models in geomorphology. Hydro-Geomorphology-Models and Trends. InTechOpen, 2017b, 81-112.

Tachikawa T, Kaku M, Iwasaki A, Gesch D B, Oimoen M J, Zhang Z, Denielson J, Krieger T, Curtis B, Haase J, Abrams M, Crippen R & Carabajal C (2011). ASTER global digital elevation model version 2-summary of validation results. NASA.

Tadono T, Ishida H, Oda F, Naito S, Minakawa K & Iwamoto H (2014). Precise global DEM generation by ALOS PRISM. ISPRS Annals of the Photogrammetry, Remote Sensing and Spatial Information Sciences, 2(4), 71.

Yang X & Hodler T (2000). Visual and statistical comparisons of surface modeling techniques for point-based environmental data, Cartography and Geographic Information Science, 27(2):165–175.

Yang K, Smith L C, Chu V W, Gleason C J & Li M (2015). A caution on the use of surface digital elevation models to simulate supraglacial hydrology of the Greenland ice sheet. IEEE Journal of Selected Topics in Applied Earth Observations and Remote Sensing, 8(11), 5212-5224.

Yılmaztürk S (2015). Sbas-ınsar Yöntemiyle Düşey Yönlü Yüzey Deformasyonlarının Belirlenmesi: Bursa-orhaneli Linyit Madeni Örneği. Master Thesis, İstanbul Technical University, Instıtute of Science and Technology, Turkey.

Zebker H A, Goldstein R M (1986). Topographic mapping from interferometric SAR observations, J Geophys Res, 91:4493–4999.

International Journal of Engineering and Geosciences

https://dergipark.org.tr/en/pub/ijeg

e-ISSN 2548-0960

Relationship between land surface temperature and normalized difference water index on various land surfaces: A seasonal analysis

Subhanil Guha[*1] **Himanshu Govil**[1]

[1]*National Institute of Technology Raipur, Department of Applied Geology, Raipur, India*

Keywords
Landsat
Land surface
LST
NDWI
Raipur

ABSTRACT

The present study examines the seasonal relationship between land surface temperature (LST) and normalized difference water index (NDWI) on various land surfaces in Raipur City of India by using a series of Landsat images for four specific seasons since 1991-92. The LST is retrieved using the mono-window algorithm technique. The results show that the LST of the study area is noticeably affected by surface composition. The best correlation (correlation coefficient r = 0.42) between the LST and NDWI is achieved in the post-monsoon season, followed by the monsoon season (r = 0.33), pre-monsoon season (r = 0.25), and winter season (r = 0.04). There is a moderate negative correlation (r = -0.49, -0.33, -0.31, and -0.25 in the pre-monsoon, monsoon, post-monsoon, and winter season, respectively) generated between the LST and NDWI on water bodies. On green vegetation, this LST-NDWI correlation is moderate positive (r = 0.67, 0.43, 0.50, and 0.25 in the pre-monsoon, monsoon, post-monsoon, and winter season, respectively). On human settlement and barren land surface, the correlation is weak positive (r = 0.24, 0.21, 0.27, and 0.15 in the pre-monsoon, monsoon, post-monsoon, and winter season, respectively). The output of the research work can be used in the town planning section of any urban agglomeration.

1. INTRODUCTION

Land surface temperature (LST) is a significant factor for investigating the biogeochemical processes of the land surface (Tomlinson et al. 2011; Hao et al. 2016). A variation on LST is due to the variation in land surface configuration (Hou et al. 2010). Generally, green vegetation and water bodies present low LST, whereas built-up area, bare rock surface or dry soil reflects high LST (Guha et al. 2020a). Thus, LST related studies are very important in urban land use planning and development (Li et al. 2017). Urban heat island and urban hot spots are a very common term in an urban environment and are indicated by the zone of very high LST inside the urban bodies (Guha et al. 2017). Normalized difference water index (NDWI) is the most popular index for water surface extraction and it is invariably used in LULC and LST related studies (McFeeters 1996; Chen et al. 2006; Essa et al. 2012; Yuan et al. 2017; Guha et al. 2020b). Generally, the nature of LST-NDWI relationship in an urban area is insignificant which is controlled by several factors, such as humidity, vegetation, wetland, bare land, air pollution, rock surface, dry or wet soil, heterogeneous man-made materials, etc. (McFeeters 1996; Ghobadi et al. 2014; Guha et al. 2020c).

In many current research articles, the relationship between LST and NDWI was constructed using thermal infrared remote sensing. However, the seasonal analysis of the LST-NDWI relationship in tropical India is rare. The nature of LST and NDWI is changed due to the seasonal changes of evaporation, precipitation, moisture content, air temperature, etc. The LST-NDWI relationship was performed on Raipur City of Chhattisgarh State in Central India as it is not influenced by the humid maritime or dry extreme climatic condition. The study examines the nature and trend of the effect of LST on NDWI and the LST-NDWI relation on various land surfaces and their seasonal variation. The main focus of the study is to explore the long-term seasonal analysis of LST-NDWI correlation on various

*Corresponding Author

*(subhanilguha@gmail.com) ORCID ID 0000-0002-2967-7248
(himgeo@gmail.com) ORCID ID 0000-0002-3433-8355

Cite this article

Guha S & Govil H (2021). Relationship between land surface temperature and normalized difference water index on various land surfaces: A seasonal analysis. International Journal of Engineering and Geosciences, 6(3), 165-172

Research Article / DOI: 10.26833/ijeg.821730

Received: 05/11/2020; Accepted: 16/12/2020

land surfaces. The study will be effective for the future town and country planners for better environmental planning.

2. MATERIALS AND METHOD

2.1. Study area

The Raipur City of India was selected as the study area for the entire research work (Fig. 1). It is the capital and the largest city of Chhattisgarh State of India (URL-1). Raipur is one of the fastest-growing smart cities in India in terms of the urban area and urban population. Fig. 1(a) presents the outline map of India where Chhattisgarh State is located in the middle part (URL-2). Fig. 1(b) presents the outline map of Chhattisgarh State with districts (URL-2). Fig. 1(c) presents the false colour composite (FCC) image of Raipur City from recent Landsat 8 data (Date: 7 November 2018). Fig. 1(d) presents the digital elevation model (Date: 11 October 2011) of Raipur City (URL-3). The total study area extends between 21°11'22"N to 21°20'02"N and 81°32'20"E to 81°41'50"E with an average elevation of 219m to 322m (Fig. 1(d)). The Mahanadi River flows to the east of the city of Raipur, and the southern side has dense forests. The Maikal Hills rise on the northwest of Raipur; on the north, the land rises and merges with the Chota Nagpur Plateau, which extends northeast across Jharkhand state. On the south of Raipur lies the Deccan Plateau. The area is under a tropical wet and dry climate with four typical seasons (pre-monsoon, monsoon, post-monsoon, and winter). Hot and dry pre-monsoon season extends from March to May (Govil et al. 2019). June to September (rainy months) is significantly considered under the monsoon season. October and November months are often considered as the post-monsoon season, characterised by low pollution, moderate temperature, and moderate moisture content in plants and air, and a high percentage of green plants. December to February months (winter season) experience a cool and dry climate. The study area is also characterised by tropical mixed deciduous vegetation and mixed red soil (Govil et al. 2020). The total population of the city is over 1 million, and the sex ratio is 945 (URL-1). The city has an 86.90% total literacy rate (URL-1).

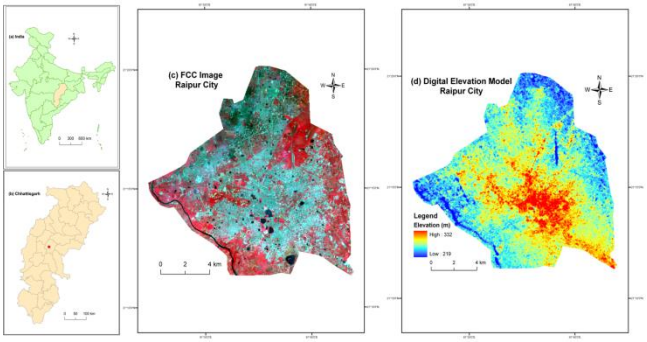

Figure 1. Location of the study area: (a) India (b) Chhattisgarh (c) FCC image of Raipur City (d) DEM of Raipur City

2.2. Data

Table 1. Specification of Landsat data sets

Date of acquisition	Time (UTC)	Cloud cover (%)	Resolution of TIR bands (m)
18-Mar-91	04:17:34	0	120
03-Apr-91	04:17:46	0	120
21-May-91	04:18:39	1	120
26-Sep-91	04:20:03	13	120
12-Oct-91	04:20:12	6	120
13-Nov-91	04:20:19	1	120
16-Jan-92	04:20:22	3	120
01-Feb-92	04:20:27	0	120
17-Feb-92	04:20:15	4	120
14-Apr-95	04:05:06	0	120
10-Dec-95	03:56:47	0	120
27-Jan-96	04:00:14	0	120
23-Sep-96	04:14:16	2	120
09-Oct-96	04:15:07	0	120
25-Oct-96	04:15:55	5	120
10-Nov-96	04:16:41	7	120
11-Nov-99	04:49:00	0	60
30-Jan-00	04:48:55	0	60
03-Apr-00	04:48:35	0	60
05-May-00	04:48:20	0	60
26-Sep-00	04:46:33	6	60
15-Dec-00	04:46:31	0	60
21-Mar-04	04:35:14	0	120
22-Apr-04	04:36:01	1	120
24-May-04	04:36:54	0	120
09-Jun-04	04:37:23	9	120
29-Sep-04	04:40:16	9	120
15-Oct-04	04:40:36	4	120
16-Nov-04	04:41:11	0	120
02-Dec-04	04:41:33	0	120
18-Dec-04	04:41:52	0	120
19-Jan-05	04:42:17	0	120
04-Feb-05	04:42:29	0	120
03-Mar-09	04:42:22	0	120
19-Mar-09	04:42:44	2	120
04-Apr-09	04:43:05	0	120
20-Apr-09	04:43:24	0	120
06-May-09	04:43:42	0	120
22-May-09	04:44:00	1	120
23-Jun-09	04:44:35	0	120
13-Oct-09	04:46:12	0	120
29-Oct-09	04:46:20	0	120
16-Dec-09	04:46:44	1	120
17-Jan-10	04:46:55	6	120
02-Feb-10	04:46:59	0	120
18-Feb-10	04:47:02	7	100
17-Mar-14	04:56:36	0	100
02-Apr-14	04:56:19	0	100
20-May-14	04:55:38	5	100
05-Jun-14	04:55:45	0	100
12-Nov-14	04:56:21	7	100
30-Dec-14	04:56:09	0	100
15-Jan-15	04:56:09	0	100
31-Jan-15	04:56:04	0	100
16-Feb-15	04:55:55	0	100
12-Mar-18	04:55:43	2	100
28-Mar-18	04:55:36	0	100
15-May-18	04:55:08	0	100
16-Jun-18	04:55:01	2	100
06-Oct-18	04:55:53	0	100
22-Oct-18	04:55:59	0	100
07-Nov-18	04:56:03	0	100
25-Dec-18	04:55:59	0	100
11-Feb-19	04:55:52	0	100
27-Feb-19	04:55:48	4	100

Table 1 shows the specification of Landsat data of different sensors. Landsat 8 thermal infrared sensors (TIRS) dataset has two TIR bands (bands 10 and 11) in which band 11 has a larger calibration uncertainty. Thus, only TIR band 10 data (100 m resolution) was

recommended for the present study (Barsi et al. 2014). Landsat 5 thematic mapper (TM) data has only one TIR band (band 6) of 120 m resolution. Landsat 7 enhanced thematic mapper plus (ETM+) data has a TIR band (band 6) of 60 m resolution. The TIR bands of all the Landsat sensors were resampled to 30 m pixel size by the data provider (URL-3) as the spatial resolution of visible to near-infrared (VNIR) and shortwave infrared (SWIR) bands of the three types of Landsat sensors is 30 m. All the raster calculations were processed in the environment of ArcGIS 9.3 and ERDAS IMAGINE 9.1 software.

2.3. Retrieving LST from Landsat Data

In this study, the mono-window algorithm was applied to retrieve LST from multi-temporal Landsat satellite sensors (Qin et al. 2001) where three necessary parameters are ground emissivity, atmospheric transmittance, and effective mean atmospheric temperature. At first, the original TIR bands (100 m resolution for Landsat 8 OLI/TIRS data, 120 m resolution for Landsat 5 TM data) were resampled into 30 m by USGS data centre for further application.

The TIR pixel values are firstly converted into radiance from digital number (DN) values (Markham & Barkar 1985). Radiance for TIR band of Landsat 5 TM data is obtained using Eq. (1) (URL-3):

$$L_\lambda = \left[\frac{L_{MAX\lambda} - L_{MIN\lambda}}{QCAL_{MAX} - QCAL_{MIN}}\right] * \left[Q_{CAL} - QCAL_{MIN}\right] + L_{MIN\lambda} \qquad (1)$$

where, L_λ is Top of Atmosphere (TOA) spectral radiance ($Wm^{-2}sr^{-1}mm^{-1}$), Q_{CAL} is the quantized calibrated pixel value in DN, $L_{MIN\lambda}$ ($Wm^{-2}sr^{-1}mm^{-1}$) is the spectral radiance scaled to $QCAL_{MIN}$, $L_{MAX\lambda}$ ($Wm^{-2}sr^{-1}mm^{-1}$) is the spectral radiance scaled to $QCAL_{MAX}$, $QCAL_{MIN}$ is the minimum quantized calibrated pixel value in DN and $QCAL_{MAX}$ is the maximum quantized calibrated pixel value in DN. $L_{MIN\lambda}$, $L_{MAX\lambda}$, $QCAL_{MIN}$, and $QCAL_{MAX}$ values are obtained from the metadata file of Landsat TM data. Radiance for Landsat 8 TIR band is obtained from Eq. (2) (Zanter 2019):

$$L_\lambda = M_L.Q_{CAL} + A_L \qquad (2)$$

where, L_λ is the TOA spectral radiance ($Wm^{-2}sr^{-1}mm^{-1}$), M_L is the band-specific multiplicative rescaling factor from the metadata, A_L is the band-specific additive rescaling factor from the metadata, Q_{CAL} is the quantized and calibrated standard product pixel values (DN). All of these variables can be retrieved from the metadata file of Landsat 8 data.

For Landsat 5 data, the reflectance value is obtained from radiances using Eq. (3) (URL-3):

$$\rho_\lambda = \frac{\pi.L_\lambda.d^2}{ESUN_\lambda.\cos\theta_s} \qquad (3)$$

where, ρ_λ is unitless planetary reflectance, L_λ is the TOA spectral radiance ($Wm^{-2}sr^{-1}\mu m^{-1}$), d is Earth-Sun distance in astronomical units, $ESUN_\lambda$ is the mean solar exo-atmospheric spectral irradiances ($Wm^{-2}\mu m^{-1}$) and θ_s is the solar zenith angle in degrees. $ESUN_\lambda$ values for each band of Landsat 5 can be obtained from the handbooks of the related mission. θ_s and d values can be attained from the metadata file (Coll et al. 2010).

For Landsat 8 data, reflectance conversion can be applied to DN values directly as in Eq. (4) (Zanter 2019):

$$\rho_\lambda = \frac{M_\rho.Q_{CAL} + A_\rho}{\sin\theta_{SE}} \qquad (4)$$

where, M_ρ is the band-specific multiplicative rescaling factor from the metadata, A_ρ is the band-specific additive rescaling factor from the metadata, Q_{CAL} is the quantized and calibrated standard product pixel values (DN) and θ_{SE} is the local sun elevation angle from metadata file.

Eq. (5) is used to convert the spectral radiance to at-sensor brightness temperature (Wukelic et al. 1989; Chen et al. 2006):

$$T_b = \frac{K_2}{\ln(\frac{K_1}{L_\lambda} + 1)} \qquad (5)$$

where, T_b is the brightness temperature in Kelvin (K), L_λ is the spectral radiance in $Wm^{-2}sr^{-1}mm^{-1}$; K_2 and K_1 are calibration constants. For Landsat 8 data, K_1 is 774.89, K_2 is 1321.08 ($Wm^{-2}sr^{-1}mm^{-1}$). For Landsat 5 data, K_1 is 607.76, K_2 is 1260.56 ($Wm^{-2}sr^{-1}mm^{-1}$).

The land surface emissivity ε, is estimated from Eq. (6) using the NDVI Thresholds Method (Sobrino et al. 2001, 2004; Vlassova et al. 2014).

$$\varepsilon = \varepsilon_v F_v + \varepsilon_s(1 - F_v) + d\varepsilon \qquad (6)$$

where, ε is land surface emissivity, ε_v is vegetation emissivity, ε_s is soil emissivity, F_v is fractional vegetation, $d\varepsilon$ is the effect of the geometrical distribution of the natural surfaces and internal reflections that can be expressed by Eq. (7):

$$d\varepsilon = (1 - \varepsilon_s)(1 - F_v)F\varepsilon_v \qquad (7)$$

where, ε_v is vegetation emissivity, ε_s is soil emissivity, F_v is fractional vegetation, F is a shape factor whose mean is 0.55, the value of $d\varepsilon$ may be 2% for mixed land surfaces Sobrino et al. 2004).

The fractional vegetation F_v, of each pixel, is determined from the NDVI using Eq. (8) (Carlson & Repley 1997):

$$F_v = \left(\frac{NDVI - NDVI_{min}}{NDVI_{max} - NDVI_{min}} \right)^2 \quad (8)$$

where, $(a) NDVI < 0.2$ for bare soil; $(b) NDVI > 0.5$ for vegetation; $(c) 0.2 <= NDVI <= 0.5$ for mixed land with bare soil and vegetation (Sobrino et al. 2001, 2004; Vlassova et al. 2014).

Finally, the land surface emissivity ε can be expressed by Eq. (9):

$$\varepsilon = 0.004 * F_v + 0.986 \quad (9)$$

where, ε is land surface emissivity, F_v is fractional vegetation.

Water vapour content is estimated by Eq. (10) (Yang & Qiu 1996; Li 2006):

$$w = 0.0981 * \left[10 * 0.6108 * \exp\left(\frac{17.27 * (T_0 - 273.15)}{237.3 + (T_0 - 273.15)} \right) * RH \right] + 0.1697 \quad (10)$$

where, w is the water vapour content (g/cm^2), T_0 is the near-surface air temperature in Kelvin (K), RH is the relative humidity (%). These parameters of atmospheric profile are the average values of 14 stations around Raipur which are obtained from the Meteorological Centre, Raipur (http://www.imdraipur.gov.in) and the Regional Meteorological Centre, Nagpur (http://www.imdnagpur.gov.in). Atmospheric transmittance is determined for Raipur City using Eq. (11) (Qin et al. 2001; Sun et al. 2010):

$$\tau = 1.031412 - 0.11536w \quad (11)$$

where, τ is the total atmospheric transmittance, w is the water vapour content (g/cm^2).

Raipur City is located in the tropical region. Thus, Eq. (12) is applied to compute the effective mean atmospheric transmittance of Raipur (Qin et al. 2001; Sun et al. 2010):

$$T_a = 17.9769 + 0.91715T_0 \quad (12)$$

LST is retrieved from Landsat 5 TM and Landsat 8 OLI/TIRS satellite data by using Eq. (13-15) (Qin et al. 2001):

$$T_s = \frac{\left[a(1 - C - D) + \left(b(1 - C - D) + C + D \right) T_b - DT_a \right]}{C} \quad (13)$$

$$C = \varepsilon\tau \quad (14)$$

$$D = (1 - \tau)\left[1 + (1 - \varepsilon)\tau \right] \quad (15)$$

where, ε is the land surface emissivity, τ is the total atmospheric transmittance, C and D are internal parameters based on atmospheric transmittance and land surface emissivity, T_b is the at-sensor brightness temperature, T_a is the mean atmospheric temperature, T_0 is the near-surface air temperature, T_s is the land surface temperature, $a = -67.355351$, $b = 0.458606$.

2.4. Extraction of Different Types of land surface by Using NDWI

Various land surface biophysical parameters were applied to specify different types of land surface features (Govil et al. 2019, 2020). In this study, special emphasis was given on NDWI (McFeeters 1996, 2013) for determining the relationship with LST. NDWI is determined by the green and NIR bands. For, Landsat 5 TM and Landsat 7 ETM+ data, band 2 is used as the green band and band 4 is used as the NIR band, respectively. For Landsat 8 operational land imager (OLI) and TIRS data, band 3 and band 5 are used as the green and NIR bands, respectively (Table 2). The value of NDWI is ranged between −1 and +1. Generally, the negative value of NDWI indicates the built-up area and bare land that have no water surfaces (Table 2). The dryness increases with the increase of the negativity of NDWI. NDWI value ranges between 0 to 0.3 shows the water bodies (McFeeters 2013), whereas NDWI > 0.3 shows the vegetation with water surfaces (McFeeters 1996, 2013; Chen et al. 2006; Guha et al. 2017). Generally, the post-monsoon images reduce the level of air pollution due to the presence of high moisture content in the air and these images also enhance the greenness of an area. Thus, the post-monsoon images are generally considered for the generation of land use/land cover (LULC) maps. LULC maps were generated using the aforesaid threshold limits of NDWI (McFeeters 1996, 2013; Chen et al. 2006: Guha et al. 2017) and the result was validated by the maximum likelihood classification. The average calculated values of the kappa coefficient and overall accuracy for all the images were 0.87 and 92.14%, respectively.

Table 2. Description of NDWI.

Acronym	Description	Formulation	References
NDBaI	Normalized difference bareness index	$\frac{Green - NIR}{Green + NIR}$	McFeeters 1996

3. RESULTS AND DISCUSSION

3.1. Extraction of LULC Types Using NDWI

The total area under different LULC categories was shown in Table 3. Water bodies were the most stable LULC type in the study area. Green vegetation was decreased in a very significant amount (76.80 km^2) from 1991-92 to 2018-19. On the other hand, the built-up

area and bare land were increased at a very high rate (78.37 km^2 in 27 years) due to rapid land conversion. In 1991-92, the built-up area and bare land were mainly found in the central part of the Raipur City. The northwest portion of the city was urbanised rapidly from 1991-92 to 2004-05 as the percentage of urban vegetation was declined due to the conversion into built-up areas. After 2004-05, the green areas were reduced at an alarming rate as most of the parts of the city were converted into bare land and built-up area. Only the eastern and the south-western parts were covered by urban vegetation.

Table 3. Total area (km^2) under different types of LULC.

Year	Green vegetation	Built-up area and bare land	Water bodies
1991-92	140.38	21.16	2.69
1995-96	130.23	31.72	2.29
1999-00	117.74	44.59	1.89
2004-05	112.41	49.68	2.14
2009-10	90.69	71.59	1.95
2014-15	81.63	81.28	1.32
2018-19	63.58	99.53	1.12

3.2. Characteristics of the Spatial Distribution of LST and NDWI

There is a prominent seasonal variation of different periods that occurred in mean and standard deviation (STD) values of LST (Table 4). The winter season indicates the lowest mean LST values for all the years, whereas the highest mean LST values were found in the pre-monsoon seasons during the entire time. From 1991-92 to 2018-19, the mean LST increased in every season. The post-monsoon season has the mean LST value nearer to the winter season, while monsoon season has a slightly high value of mean LST than the post-monsoon season. The average values of LST and the correlation coefficient of LST and NDWI from 1991-92 to 2018-19 were shown in grey shades inside the Table 4.

Fig. 2 shows the seasonal contrast in the distribution of LST from 1991-92 to 2018-19. The pre-monsoon season has the maximum values of mean LST followed by monsoon, post-monsoon, and winter season. The north-west and south-east parts of the study area exhibit high LST. These parts also have a low percentage of urban vegetation and a high percentage of built-up area and bare land. It shows that the proportion of vegetation has been reduced and the built-up area was increased significantly with time. The correlation coefficient values of Pearson's linear correlation between the LST and NDWI for the entire period were moderate positive to weak negative. The post-monsoon season has the best mean correlation coefficient value (0.42), followed by the monsoon (0.34), pre-monsoon (0.25), and winter (0.04) season.

It is seen from Fig. 2 that in 2018-19, more than 90% of the area in the pre-monsoon season was above 38^{o}C LST. The result is different in the winter season, where no area of the city was above 38^{o}C LST. In 1991-92, almost 90% of the area was below 24^{o}C LST in the winter season. Monsoon and post-monsoon seasons indicate a moderate range of LST. The mean LST of the study area was gradually increased between 1991-92 and 2018-19. The conversion of other lands into the built-up area and bare land influences a lot on the mean LST of the city. Both the changed and unchanged built-up area and bare land suffer from the increasing trend of LST. These results significantly present the influence of climate shift in Raipur City.

Table 4. Temporal and seasonal variation of LST values and Pearson's correlation coefficient values of LST-NDWI relationship (significant al 0.05 level).

Season	Year of acquisition	LST (^{o}C) Min.	Max.	Mean	Std.	Correlation coefficients for LST-NDWI relationship
Pre-monsoon	1991-92	23.81	36.27	31.54	1.52	0.13
	1995-96	24.54	41.07	34.64	1.89	0.12
	1999-00	26.36	42.23	36.38	1.93	0.33
	2004-05	26.95	44.07	38.01	2.19	0.29
	2009-10	28.81	46.48	39.60	2.54	0.26
	2014-15	31.93	48.22	41.28	1.75	0.29
	2018-19	33.46	51.11	43.74	1.75	0.35
	Average	27.98	44.21	37.88	1.94	0.25
Monsoon	1991-92	19.87	30.83	25.74	1.41	0.26
	1995-96	21.21	33.01	26.50	1.33	0.36
	1999-00	22.76	35.91	27.81	1.34	0.48
	2004-05	24.17	36.20	31.32	1.33	0.38
	2009-10	25.94	38.38	33.06	2.40	0.31
	2014-15	27.74	40.15	34.87	1.68	0.33
	2018-19	30.59	41.98	37.30	1.13	0.36
	Average	24.61	36.64	30.94	1.52	0.34
Post-monsoon	1991-92	19.72	29.56	24.32	1.72	0.35
	1995-96	20.42	30.33	25.12	1.34	0.45
	1999-00	22.41	33.47	26.84	1.91	0.26
	2004-05	23.03	35.25	28.01	1.71	0.34
	2009-10	24.62	37.91	30.26	1.60	0.47
	2014-15	26.24	38.22	31.68	1.12	0.49
	2018-19	28.92	41.28	33.70	1.34	0.55
	Average	23.62	35.15	28.56	1.53	0.42
Winter	1991-92	18.22	28.33	23.29	1.22	0.05
	1995-96	20.08	28.68	24.40	1.04	-0.03
	1999-00	20.44	32.80	25.21	1.81	-0.08
	2004-05	21.08	33.21	26.47	1.25	-0.03
	2009-10	22.06	34.36	27.98	1.23	0.11
	2014-15	22.80	36.21	28.90	1.39	0.03
	2018-19	24.31	38.36	30.46	1.37	0.21
	Average	21.28	33.14	26.67	1.33	0.57

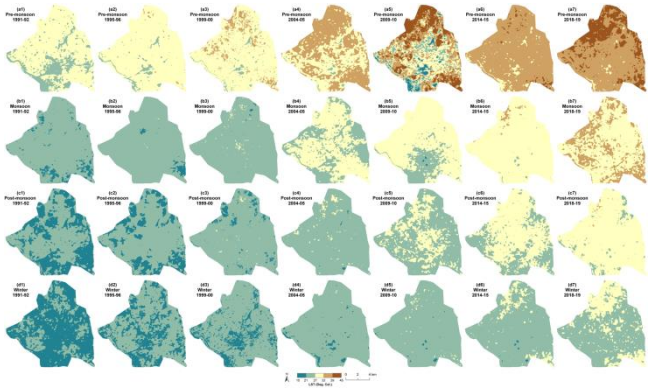

Fig. 2. Spatial distribution of LST for the following years: (a1-a4) 1991-92 (b1-b4) 1995-96 (c1-c4) 1999-00 (d1-d4) 2004-05 (e1-e4) 2009-10 (f1-f4) 2014-15 (g1-g4) 2018-19.

Fig. 3 shows the seasonal variation in the spatial distribution of NDWI from 1991-92 to 2018-19. The high and low NDWI regions were seasonally stable since the 1991-92 sessions. Only the values of NDWI were changed, whereas the overall distributional pattern of NDWI remains almost unchanged. The central part of

the city always presents a higher NDWI value. A lower NDWI value is seen throughout the periphery of the city.

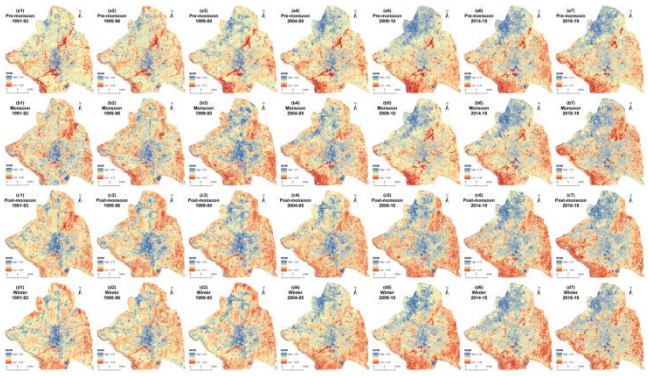

Fig. 3. Spatial distribution of NDBaI for the following years: (a1-a4) 1991-92 (b1-b4) 1995-96 (c1-c4) 1999-00 (d1-d4) 2004-05 (e1-e4) 2009-10 (f1-f4) 2014-15 (g1-g4) 2018-19.

3.3. Relationship between LST and various types of LULC

The LST of the study area significantly depends upon the LULC types. Generally, the area with green vegetation has low LST value; the built-up areas and bare lands have moderate to high LST value, and the water bodies are characterised by a low to moderate range of LST. In the pre-monsoon season, the built-up area and bare land have comparatively high LST than the other LULC types. But in the winter season, these areas have comparatively low to moderate LST due to low emissivity. Green areas and water areas are characterised by a relatively stable range of low LST values.

Fig. 4 presents the temporal changes of LST on various categories of LULC. Vegetation and water surface increases the LST, while bare land/built-up surface decreases LST. Most of the converted lands are built-up or bare land. Consequently, the built-up/bare land surfaces increase, while vegetation and water surface decrease in a significant amount. Land conversion is the main responsible factor for the seasonal change of mean LST. As a result, the mean LST significantly increased (1.60^{o}C in pre-monsoon, 5.34^{o}C in monsoon, 4.76^{o}C in post-monsoon, and 1.08^{o}C in winter season) from 1991-92 to 2018-19.

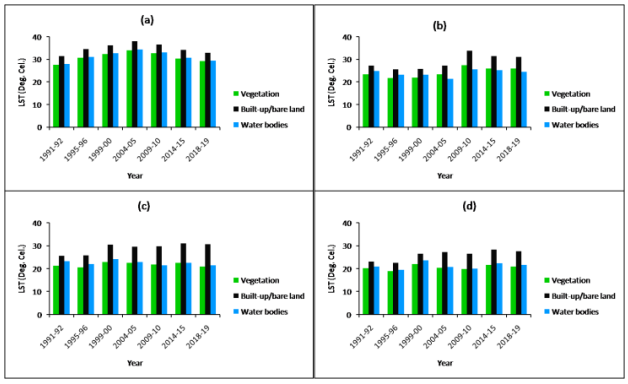

Figure 4. Seasonal variability of mean LST on various categories of LULC: (a) pre-monsoon (b) monsoon (c) post-monsoon (d) winter.

3.4. Seasonal contrast on LST-NDWI relationship

Table 5 shows the seasonal contrast of LST-NDWI relationships on different LULC types in winter, pre-monsoon, monsoon, and post-monsoon season, respectively. Here, only three types of LULC were considered, i.e., (1) vegetation, (2) water bodies, and (3) built-up area and bare land. On water bodies, the LST-NDWI relationship is moderate negative for any season. NDWI is a water index that is frequently used in water body extraction. On the bare land and built-up area of the study area, the correlation is a weak positive for all four seasons. On green vegetation, the relationship is strong (pre-monsoon) to moderate (monsoon, post-monsoon, and winter (weak moderate)) positive. The pre-monsoon season has a strong positive LST-NDWI correlation on the green vegetation (0.67), a weak positive correlation on the bare land and built-up area (0.24), and a moderate negative correlation on green vegetation (-0.49). In the monsoon season, the correlation is moderate positive on green vegetation (0.43), weak positive (0.21) on bare land and built-up area, whereas the correlation is moderate negative (-0.43) on water bodies. The post-monsoon season has a moderate to strong positive correlation (0.50) on green vegetation, a weak positive correlation (0.27) on the bare land and built-up area, and has a moderate negative correlation (-0.31) on water bodies. In winter season, the LST-NDWI correlation is weak positive (0.25) on green vegetation, weak positive (0.15) on built-up area and bare lands. Water bodies have a moderate negative (-0.45) correlation in the winter season.

Table 5. Seasonal contrast in the LST-NDWI relationship on different types of LULC (significant at 0.05 level).

	Pre-monsoon			Monsoon		
Year	Vegetation	Built-up/bare land	Water bodies	Vegetation	Built-up/bare land	Water bodies
1991-92	0.57	0.08	-0.55	0.23	0.11	-0.41
1995-96	0.60	0.14	-0.49	0.25	0.10	-0.31
1999-00	0.76	0.31	-0.51	0.37	0.29	-0.28
2004-05	0.70	0.14	-0.40	0.33	0.07	-0.35
2009-10	0.73	0.35	-0.46	0.59	0.30	-0.31
2014-15	0.61	0.33	-0.46	0.56	0.34	-0.28
2018-19	0.70	0.35	-0.59	0.65	0.27	-0.42
	0.67	0.24	-0.49	0.43	0.21	-0.33
	Post-monsoon			Winter		
Year	Vegetation	Built-up/bare land	Water bodies	Vegetation	Built-up/bare land	Water bodies
1991-92	0.55	0.19	-0.26	0.39	0.16	-0.49
1995-96	0.57	0.23	-0.22	0.23	0.14	-0.46
1999-00	0.51	0.34	-0.27	0.23	0.10	-0.43
2004-05	0.48	0.28	-0.38	0.19	0.14	-0.55
2009-10	0.49	0.27	-0.45	0.25	0.21	-0.47
2014-15	0.46	0.26	-0.32	0.22	0.11	-0.39
2018-19	0.44	0.32	-0.28	0.26	0.18	-0.34
	0.50	0.27	-0.31	0.25	0.15	-0.45

Fig. 5 represents a generalised view of the overall seasonal variation of LST-NDWI relationships for the whole of the study area. The relationship was positive in the three seasons except for the winter, where it was mostly negative along with some positive values. It can be concluded from Fig. 5 that the post-monsoon season reveals the best correlation, followed by the monsoon and pre-monsoon seasons. There was practically no such relationship found in the winter season. It was mainly due to the high intensity of moisture content in the air. Dry seasons (winter and pre-monsoon) reduce

the strength of the correlation, while the wet seasons (post-monsoon and monsoon) enhance the strength of the LST-NDWI correlation.

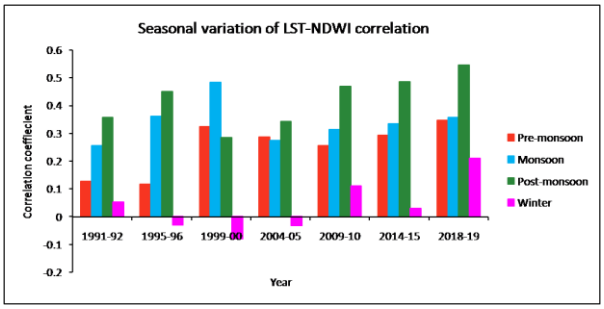

Figure 5. Seasonal contrast on the LST-NDWI relationship for the whole of the study area (significant at 0.05 level).

The present study indicates that LST builds an insignificant and non-linear correlation with NDWI in Raipur City, India from 1991-92 to 2018-19 in four different seasons (pre-monsoon, monsoon, post-monsoon, and winter). The result is reliable and significant compared to the other similar studies using Landsat data conducted on the cities from different parts of the world in recent years. NDWI and LST built a non-linear correlation when considering the whole urban area in Wuhan City of China (Wu et al. 2019). Choudhury et al. (2019) showed a negative correlation of the LST-NDWI relationship on the water bodies in the Asansol-Durgapur Development Region, India. LST and NDWI produced a negative correlation on the water bodies of Nanchang City, China (Zhang et al. 2017). A significant negative relationship was found between LST and NDWI on the water bodies in Shenzhen City, China (Chen et al. 2006). The present result shows a significant and stable negative correlation (-0.49, -0.34, -0.31, and -0.45 in pre-monsoon, monsoon, post-monsoon, and winter seasons, respectively) between LST and NDWI on the water bodies throughout the period.

4. CONCLUSION

The present study investigates the temporal and seasonal relationship of LST and NDWI in Raipur City, India using sixty-four Landsat datasets of four different seasons (pre-monsoon, monsoon, post-monsoon, and winter) for 1991-92, 1995-96, 1999-00, 2004-05, 2009-10, 2014-15, and 2018-19. In general, the results show that the relationship between LST and NDWI is non-linear. The correlation is moderate positive in the post-monsoon (0.42) and monsoon (0.34) seasons, whereas it is found weak positive in pre-monsoon (0.25) and winter (0.03). The presence of high moisture content in the air and plants is the main responsible factor for high positivity. The LST-NDWI relationship varies for specific LULC types. The water bodies reflect a moderate negative correlation of LST-NDWI in all the four seasons (-0.49 in pre-monsoon, -0.34 in monsoon, -0.31 in post-monsoon, and -0.45 in winter). On green vegetation, this LST-NDWI correlation is also strong positive in pre-monsoon (0.67), moderate positive in monsoon (0.43) and post-monsoon (0.50), weak positive in winter (0.25). The built-up area and bare land build a weak positive correlation of LST-NDWI in all the four seasons (0.24 in pre-monsoon, 0.21 in monsoon, 0.27 in post-monsoon, and 0.15 in winter). All the four seasons have an insignificant and non-linear correlation for all LULC types (0.14 in pre-monsoon, 0.10 in monsoon, 0.15 in post-monsoon, and -0.02 in winter). The high percentage of urban vegetation and urban water bodies can promote the ecological health of a rapidly growing city like Raipur. Thus, this research work can be an effective one for the future town and country planners.

ACKNOWLEDGEMENT

The authors are indebted to the United States Geological Survey (USGS).

REFERENCES

Barsi J, Schott J, Hook S, Raqueno N, Markham B & Radocinski R (2014). Landsat-8 thermal infrared sensor (TIRS) vicarious radiometric calibration. Remote Sensing, 6(11), 11607-11626.

Carlson T N & Ripley D A (1997). On the Relation between NDVI, Fractional Vegetation Cover, and Leaf Area Index. Remote Sensing of Environment, 62, 241-252. https://doi.org/10.1016/S0034-4257(97)00104-1

Chen X L, Zhao H M, Li P X & Yi Z Y (2006). Remote sensing image-based analysis of the relationship between urban heat island and land use/cover changes. Remote Sensing of Environment, 104(2), 133–146. https://doi.org/10.1016/j.rse.2005.11.016

Choudhury D, Das K, & Das A (2019). Assessment of land use land cover changes and its impact on variations of land surface temperature in Asansol-Durgapur Development Region. Egyptian Journal of Remote Sensing and Space Sciences, 22(2), 203-218. https://doi.org/10.1016/j.ejrs.2018.05.004

Coll C, Galve J M, Sanchez J M & Caselles V. 2010. Validation of Landsat-7/ETM+ thermal-band calibration and atmospheric correction with ground-based measurements. IEEE Transactions on Geoscience and Remote Sensing, 48(1), 547–555. https://doi.org/10.1109/TGRS.2009.2024934

Essa W, Verbeiren B, Van der Kwast J, Van de Voorde T & Batelaan O (2012). Evaluation of the DisTrad thermal sharpening methodology for urban areas. International Journal of Applied Earth Observation and Geoinformation, 19, 163-172. https://doi.org/10.1016/j.jag.2012.05.010

Ghobadi Y., Pradhan B., Shafri H.Z.M. & Kabiri K. 2014. Assessment of spatial relationship between land surface temperature and land use/cover retrieval from multi-temporal remote sensing data in South Karkheh Sub-basin, Iran. Arabian Journal of Geosciences, 8(1), 525–537. https://doi: 10.1007/s12517-013-1244-3.

Govil H, Guha S, Dey A & Gill N (2019). Seasonal evaluation of downscaled land surface temperature: A case study in a humid tropical city. Heliyon, 5(6), e01923. https://doi.org/ 10.1016/j.heliyon.2019.e01923

Govil H, Guha S, Diwan P, Gill N & Dey A (2020). Analyzing Linear Relationships of LST with NDVI and

MNDISI Using Various Resolution Levels of Landsat 8 OLI and TIRS Data. Data Management, Analytics and Innovation. Advances in Intelligent Systems and Computing, 1042. Springer, Singapore, 171-184. https://doi.org/10.1007/978-981-32-9949-8_13

Guha S, Govil H & Besoya M (2020c). An investigation on seasonal variability between LST and NDWI in an urban environment using Landsat satellite data. Geomatics, Natural Hazards and Risk, 11(1), 1319-1345. https://doi.org/10.1080/19475705.2020.1789762

Guha S, Govil H & Mukherjee S (2017). Dynamic analysis and ecological evaluation of urban heat islands in Raipur city, India. Journal of Applied Remote Sensing, 11(3), 036020. https://doi:10.1117/1.JRS.11.036020

Guha S, Govil H, Dey A & Gill N (2020a). A case study on the relationship between land surface temperature and land surface indices in Raipur City, India. Geografisk Tidsskrift-Danish Journal of Geography, 120(1), 35-50. https://doi.org/10.1080/00167223.2020.1752272

Guha S, Govil H, Gill N & Dey A (2020b). Analytical study on the relationship between land surface temperature and land use/land cover indices. Annals of GIS, 26(2), 201-216. https://doi.org/10.1080/19475683.2020.1754291

Hao X, Li W & Deng H (2016). The oasis effect and summer temperature rise in arid regions-case study in Tarim Basin. Scientific Reports, 6, 35418. https://doi.org/10.1038/srep35418

Hou G L, Zhang H Y, Wang Y Q, Qiao Z H & Zhang Z X (2010). Retrieval and Spatial Distribution of Land Surface Temperature in the Middle Part of Jilin Province Based on MODIS Data. Scientia Geographica sinica, 30, 421-427.

Li J (2006). Estimating land surface temperature from Landsat-5 TM. Remote Sensing Technology and Application, 21, 322-326.

Li W F, Cao Q W, Kun L, & Wu J S (2017). Linking potential heat source and sink to urban heat island: Heterogene-ous effects of landscape pattern on land surface temperature. Science of the Total Environment, 586, 457–465. https://doi.org/10.1016/j.scitotenv.2017.01.191

Markham B L & Barker J K (1985). Spectral characteristics of the LANDSAT thematic mapper sensors. International Journal of Remote Sensing, 6(5), 697–716. https://doi.org/10.1080/01431168508948492

McFeeters S K (1996). The use of the Normalized Difference Water Index (NDWI) in the delineation of open water features. International Journal of Remote Sensing, 17(7), 1425-1432. https://doi.org/10.1080/01431169608948714

McFeeters S K (2013). Using the Normalized Difference Water Index (NDWI) within a Geographic Information System to Detect Swimming Pools for Mosquito Abatement: A Practical Approach. Remote Sensing, 5(7), 3544-3561. https://doi.org/10.3390/rs5073544

Qin Z, Karnieli A & Barliner P (2001). A Mono-Window Algorithm for Retrieving Land Surface Temperature from Landsat TM Data and Its Application to the Israel-Egypt Border Region. International Journal of Remote Sensing, 22(18), 3719-3746. https://doi:10.1080/01431160010006971

Sobrino J A, Jimenez-Munoz J C & Paolini L (2004). Land surface temperature retrieval from Landsat TM5. Remote Sensing of Environment, 9, 434–440. https://doi:10.1016/j.rse.2004.02.003

Sobrino J A, Raissouni N & Li Z (2001). A comparative study of land surface emissivity retrieval from NOAA data. Remote Sensing of Environment, 75(2), 256–266. https://doi.org/10.1016/S0034-4257(00)00171-1

Sun Q, Tan J & Xu Y (2010). An ERDAS image processing method for retrieving LST and describing urban heat evolution: A case study in the Pearl River Delta Region in South China. Environmental Earth Science, 59, 1047-1055.

Tomlinson C J, Chapman L, Trones J E & Baker C (2011). Remote sensing land surface temperature for meteorology and climatology: a review. Meteorological Application, 118, 296–306. https://doi.org/10.1002/met.287

URL-1: https://censusindia.gov.in/2011

URL-2: http://www.surveyofindia.gov.in

URL-3: https://www.earthexplorer.usgs.gov

Vlassova L, Perez-Cabello F, Nieto H, Martín P, Riaño D, & De La Riva J (2014). Assessment of methods for land surface temperature retrieval from Landsat-5 TM images applicable to multiscale tree-grass ecosystem modeling. Remote Sensing, 6(5), 4345-4368.

Wu C, Li J, Wang C, Song C, Chen Y, Finka M & Rosa D L (2019). Understanding the relationship between urban blue infrastructure and land surface temperature. Science of the Total Environment, 694, 133742. https://doi.org/10.1016/j.scitotenv.2019.133742

Wukelic G E, Gibbons D E, Martucci L M & Foote H P (1989). Radiometric calibration of Landsat Thematic Mapper thermal band. Remote Sensing of Environment, 28, 339–347. https://doi.org/10.1016/0034-4257(89)90125-9

Yang J & Qiu J (1996). The empirical expressions of the relation between precipitable water and ground water vapor pressure for some areas in China. Scientia Atmospherica Sinica, 20, 620-626.

Yuan X, Wang W, Cui J, Meng F, Kurban A & De Maeyer P (2017). Vegetation changes and land surface feedbacks drive shifts in local temperatures over Central Asia. Scientific Reports, 7(1), 3287. https://doi.org/10.1038/s41598-017-03432-2

Zanter K (2019). Landsat 8 (L8) Data Users Handbook; EROS: Sioux Falls, SD, USA.

Zhang X, Estoque R C & Murayama Y (2017). An urban heat island study in Nanchang City, China based on land surface temperature and social-ecological variables. Sustainable Cities and Society, 32, 557-568. https://doi.org/10.1016/j.scs.2017.05.005